MORPHOLOGICAL EFFECTS ON SPIN-DEPENDENT ELECTRONIC

PROCESSES IN POLY[9,9-DIOCTYLFLUORENYL-2,7-DIYL]

THIN FILM ORGANIC LIGHT EMITTING DIODES

by

Richards G. Miller III

A dissertation submitted to the faculty of
The University of Utah
in partial fulfillment of the requirements of the degree of

Doctor of Philosophy

in

Physics

Department of Physics and Astronomy

The University of Utah

May 2017

The University of Utah Graduate School

STATEMENT OF DISSERTATION APPROVAL

The following faculty members served as the supervisory committee chair and members for the dissertation of _____ Richards G. Miller III _____ . Dates at right indicate the members' approval of the dissertation.

| ___ Christoph Boehme ___ , Chair | ___ 10/7/16 ___ |
| | Date Approved |

| ___ John M. Lupton ___ , Member | ___ 10/7/16 ___ |
| | Date Approved |

| ___ Eugene Mishchenko ___ , Member | ___ 10/7/16 ___ |
| | Date Approved |

| ___ Benjamin C. Bromley ___ , Member | ___ 10/7/16 ___ |
| | Date Approved |

| ___ Michael H. Bartl ___ , Member | _____ |
| | Date Approved |

The dissertation has also been approved by ___ Benjamin C. Bromley ___

Chair of the Department of ___ Physics and Astronomy ___

and by David B. Kieda, Dean of The Graduate School.

ABSTRACT

The goal of the work presented in this dissertation was to find out how physical ordering of organic semiconductors affects spin-dependent electronic charge carrier transitions. Organic light emitting diodes in distinct morphological phases were created out of thin films of the π-conjugated polymer poly[9,9-dioctylfluorenyl-2,7-diyl] (polyfluorene), allowing diodes to be studied with the sole difference being the degree of polymeric order in the active layer of the device. The polyfluorene morphologies studied ranged from an amorphous (glassy) phase through mixed phases, to a highly ordered (beta) phase. The phase control was achieved through a dipping procedure where a glassy polyfluorene layer is immersed in a solvent mixture that structures the side chains of a monomer unit into an alternating planar ladder structure.

Continuous-wave (cw) and pulsed (p) electrically detected magnetic resonance (EDMR) spectroscopies were used to probe charge carrier spin states within the polyfluorene layers. For cw EDMR, microwave frequencies between ~1 and 20 GHz were used, while all pEDMR measurements were conducted at X-band (~9.6 GHz). The experiments allowed for a comparison of how polymer morphology affects spin-dependent charge carrier transitions, coherent spin motion, spin relaxation times, the local nuclear (hyperfine) magnetic fields and spin-orbit effects.

In addition to film morphology, temperature and device-bias dependencies of the

spin-dependent charge carrier transitions were studied experimentally and a set of global

fit and bootstrap error analysis techniques were adapted for EDMR spectroscopy.

To my family:

Parental units 1 & 2 and Tanya baby

CONTENTS

ACKNOWLEDGMENTS

I first decided on physics as an interest to pursue as a graduating high school senior. Green energy had always seemed the ultimate goal as a kid and I still believe it to be one of the most fundamental problems facing humanity to this day. While the work in this dissertation is not going to solve any energy crises, it certainly has ties to those same questions I had back then.

Rome was not built in a day and I definitely did not make it here without the help of so many people. Of course I definitely would not be here without the love and support from my family. Without them there for me to reach out to and ground me I would have floated off a long time ago. I could never correctly express how much they have done for me.

Then there are those intellectual giants I had the privilege of calling friends and mentors:

Will Baker: The man who got me started in this lab so long ago. Seems like we met skiing and, while I complained about not knowing what I wanted to work on while we rode chairlifts, you slowly got me hooked on your own work. You are the first person to get me into a lab at Utah and also the first person to assure me I did not break the machine half an hour after you left me there.

Kipp J. van Schooten: I would not be here without you. Your work ethic in the lab is contagious, I would have given up on this project many times over if you were not there to suggest I try it a few more times. The thing I will never take for granted is you answering

all of my stupid questions, cheers.

Alexander Thiessen: The perfect friend in physics. You were always around to talk science when I was stuck on a subject and to escape when the weekend came around.

Hans Malissa: There is no question my work has been made better by you. All of your ideas and suggestions have led this body of work to encompass so much more than it would have had you not been there to tell me to go learn new things and never be satisfied with what I have as it is.

John Lupton: You rightfully challenged me on all my results. Without that, this body of work would have been a shadow of what it is today. You always pushed me to reexamine things that allowed me to catch subtle nuances that would have been overlooked otherwise.

Christoph Boehme: You gave me the chance I needed and then several others. Thanks for getting me started and continuously reinvigorated on this project so many times. Your enthusiasm and knowledge in this field knows no bounds. It is impossible not to see the beauty of what we do here when you are there to shine light on all our work.

Thanks to all of you

CHAPTER 1

INTRODUCTION

Organic semiconductors were originally derived from dyes which led to π-conjugated polymers and other molecular electronic materials that we have today [1]. They are cheap and easy to process, with the added bonus of being chemically flexible, allowing for numerous device applications akin to many of those known for silicon [2–6]. Organic semiconductors typically interact with light in the visible spectrum at room temperature and they have therefore revolutionized lighting and display applications, with organic light emitting diode (OLED) displays being used in tens of millions of modern smart phones. While these benefits of polymers would seemingly also bring them to the forefront in the photovoltaic technologies, there are still significant problems to solve which have so far led to mostly unsuccessful commercialization attempts [7,8]. In the following chapters, organic semiconductors are discussed in the context of none of these technologies, but rather, they are discussed in the context of spintronics, the utilization of the spin-degree of freedom of charge carriers for technological application which, for inorganic electronic materials, has led to dramatic technological innovations such as giant magnetoresistance devices, discovered in 1988 that revolutionized hard-disc technology [9].

1.1 What Is Organic Spintronics?

Organic spintronics is still a hypothetical technology that aims to utilize electron states in organic semiconductors for a new kind of electronics that takes advantage of not only the charge that electrons carry but also the spin degree of freedom. Since spin-orbit coupling (SOC) in condensed matter scales with Z^4 (Z being the atomic order number), carbon based materials tend to exhibit very low SOC, even though this property cannot be generalized since SOC is determined also by other influences such as the molecular curvature. Frequently though, due to low SOC, carbon-based materials like organic semiconductors exhibit paramagnetic states with long spin relaxation times [10,11]. Utilizing electron spins as an information carrier therefore seems to be even more attractive in organic semiconductors compared to inorganic semiconductors.

Examples for existing organic spintronic devices include spin-valves [5], magnetic field sensors [3], and spin-OLEDs [12]. While the idea to apply existing spintronics concepts for quantum computing has also been gaining footholds in the scientific community [13–16], there has not been much progress within the organic spintronics research domain. This may possibly be due to the unclear nature of spin-transport and spin-dependent recombination processes in organic semiconductors. Also, while single electron spin detection has been achieved more than a decade ago [17,18], it has not been demonstrated for an electron spin in an organic semiconductor material. Thus, while quantum computing is highly unlikely to develop from organic spintronics, there are numerous other currently pursued organic spintronics concepts which have a much greater likelihood to be implemented [6].

Among the still unresolved questions associated with organic spintronics is the

question of molecular structure: how does the qualitative and quantitative behavior of spin-dependent processes change between ordered and amorphous materials? This study aims to shed a light on this question by examining a polymer that can be in either an ordered, near-crystalline phase, or in a disordered, amorphous phase.

For nonspintronics related applications, organic materials have increasingly become an alternative to silicon [19] since the turn of the century with display or lighting applications entering the market since then. In contrast, organic spintronics has only been suggested since 2004 and even though numerous studies on spin-dependent processes and spin transport in organic semiconductor materials have taken place since then, any technological applications based on organic spintronics do not exist commercially yet [5,6,20–23]. The lack of technological progress of organic spintronics is mostly due to a persistent lack of progress on the fundamental understanding of electronic processes in these materials and this problem is predominantly due to the circumstance that many experimental techniques that have been established as standard spintronics characterization techniques (i.e., the Magneto-Optical-Kerr-Effect Spectroscopy or Hanle precession experiments) are not applicable to organic semiconductor materials [12]. Among the most widely applied experimental techniques to organic spintronics studies are electron paramagnetic resonance (EPR) based spectroscopies. In particular the continuous wave (cw) and pulsed electrically detected magnetic resonance (pEDMR).

1.2 Π-conjugated Polymers and Charge Transport

In contrast to most crystalline inorganic semiconductor materials, polymers have mobile charge carriers that are localized in molecular orbitals. These molecular orbits are

discrete energy levels that are distributed about an average energy level. While inorganic materials have continuous distributions of energy levels outside the bandgap, organic materials have a dense region of energy levels. Instead of a valance band edge, polymers have a "highest occupied molecular orbit" (HOMO) energy below which electrons occupy the eigenstate continuum; the "lowest unoccupied molecular orbit" (LUMO) level is akin to the conduction band edge in inorganic semiconductors. As illustrated in Fig. 1.1, the Fermi energy of an organic semiconductor generally lies between the HOMO and LUMO levels for most organic semiconductors indicating that these materials are actually predominantly insulators which only become conductive when charge carriers are injected either electrically, optically or via doping. In inorganic semiconductors charges transport takes places freely through the conduction band. In contrast, in organic materials, charges are only delocalized about the length of unbroken molecular conjugation (black lines in Fig. 1.1 d)) and their propagation through the materials takes place by means of spontaneous electronic transitions like hopping or tunneling.

The molecular orbitals of charge carriers in π-conjugated polymers arise out of a delocalization of electrons within a monomer along the backbone of a polymer. This delocalization occurs in π-conjugated polymers due to a bond hybridization. π-conjugated polymers, which include polyfluorene (PFO), are made up of alternating single and double bonds, the prototypical example being Benzene where sp^2 hybridization occurs. This hybridization makes it so that these bonds lie directly in the plane of a ring, the benzene ring with all bonds being equivalent in energy and more robust than normal atomic orbitals. Carbon atoms have 6 electrons and in the ground state, the $1s^2 2s^2 2p_x^1 2p_y^1 2p_z^0$ orbitals are occupied. When we define the z-axis as the axis perpendicular to the plane of the ring, then

each carbon atom in a benzene ring promotes one of its electrons from the 2s state to the p_z orbital whereupon it becomes a sp^2 orbital along with the $2p_x$ & $2p_y$ orbitals. While these bonds are used to hold the molecule together, the $2p_z$ orbital remains uninvolved.

As illustrated in Fig. 1.2, the π-orbitals parallel to the z axis of each carbon atom overlap laterally with their neighbors. This allows the electrons in each p_z orbital to occupy any one of the 6 p_z orbitals, thus one of the three molecular orbits that the overlapping π bonds create (as only 2 electrons can be in each orbit). Only one of the three molecular orbits is shown in Fig. 1.2 to avoid the overcrowding of the cartoon. This delocalization of charge carriers leads to conjugation [24].

Every polymer is made up of several monomer units that are bound to a like monomer on one end to create a dimer, three monomers create a trimer and so on. Each PFO polymer is made up of chromophores, segments of uninterrupted π-conjugation, which are separated by a defect along the polymer chain that breaks up the delocalized molecular orbits along the entire chain length. Each chromophore has discrete energy levels which help make up the HOMO and LUMO bands.

PFO has a backbone of two adjoining benzene rings, each polymer has charge delocalization for an extended length and thus forms modified molecular orbits. Vacant LUMO states which are filled with charges that are injected into a polymer are often of polaronic character. Therefore the charges are typically referred to as electron polarons. Similarly, when charge is removed from a HOMO state, a hole polaron is created. Electron and hole polarons are charge carriers of organic semiconductors and they can experience extended delocalization along a chromophore (orange shaded region in Fig. 1.2) in which charge transport is possible. Typically, large kinks and chain defects in the highly

disordered solids that polymers oftentimes form are the two main ways in which the long spatial delocalization of chromophores can be broken up into relatively short sections of a long polymer chain and thus cease charge delocalized transport. Charges can move past these localized domains via inter- or intrachain transfer [25] due to tunneling and hopping, a propagation that is starkly different from most inorganic semiconductors, possibly with the exception of low-temperature charge propagation in disordered amorphous semiconductors like hydrogenated amorphous silicon [26].

Charge transport in π-conjugated polymers relies on spontaneous transitions of charges between localized states implying much smaller mobilities of charge carriers and thus, conductivities in polymers, as in most organic semiconductor materials, are typically much lower than in inorganic semiconductors like Si and GaAs. The interchain transfer of charges can take place either to another segment of the same polymer if it is folded back on itself or to an adjacent polymer chain. Intrachain motion implies that the free charge continues along the same polymer. Intrachain mobilities of charge carriers in π-conjugated polymers are generally much higher compared to interchain mobilities. Free charges moving through polymers are subject to many local perturbations arising from the distribution of hyperfine fields (magnetic fields produced by local nuclei). When opposite charges become close enough to one another they can form a Coulombically bound pair system called the polaron pair. Polaron pairs are usually thought of as a hole and electron in an intermediate state between free charges and excitons. The charges are typically on different polymer chains localized at distances on the order of ~2-8 nm [27,28]. If either the hole or the electron within the polaron pair transfers to the other chromophore, the pair will undergo a transition into an exciton. Excitons have much stronger binding energies

due to the strong wave-function overlap of the two particles. Excitons are short lived; they can recombine to the ground state on a ps-scale at the longest. In contrast to excitons, polaron pairs can also dissociate into free charge carriers.

Both excitons as well as polaron pairs can exist as geminate pairs and as nongeminate pairs, where geminate pairs constitute electron-hole states with a correlated spin-state, i.e., the singlet state. Geminate pairs are created from optical charge carrier injection and they remain geminate until a pair dissociation takes place. Charge carriers in geminate pairs do not contribute to photoconductivity as long as they remain geminate [29].

Exciton states are categorized in three different classes: Frenkel, Wannier-Mott, and charge transfer (CT) excitons. The main difference between these types is their size. The Frenkel excitons are smaller than the molecular spacing, where both hole and electron are found on the same molecule. Wannier-Mott excitons can be spaced over an order of magnitude more than the molecular spacing [30]. They can be distinguished from polaron pairs by a larger exchange interaction. However, due to the strong localization of polaron states, Wannier-Mott excitons are rarely seen in organic semiconductors. The size and exchange energies of CT excitons are found somewhere between Frenkel and Wannier-Mott excitons, usually the electron and hole occupy adjacent molecules. Typical for bulk organic materials are Frenkel excitons while CT excitons can be found at materials interfaces, i.e., within organic blend materials [31].

1.3 Electronic Transitions and Spin-Selection Rules

Hopping and tunneling transport are widely occurring mechanisms in organic semiconductors. For both to be likely within a bulk material, a charge carrier must have

wavefunction overlap (exchange) from an initial energy eigenstate to an adjacent energy eigenstate. As long as charge carrier states are singly occupied, electrons and holes are paramagnetic with spin s=½ [32] and for transitions between electronic states, spin selection rules can be important. A spin-selection rule is the dependency of an electronic system's the transitions probability (i.e., of a polaron pair state) on the spin-manifold of the system before the transition occurs. In organic semiconductors, spin-orbit coupling is very weak. Because of this, the orbital angular momentum l and the spin s of a polaron pair have to be conserved independently in order to conserve the total angular momentum. As an example, when a polaron pair recombines via a singlet exciton, it forms a singlet ground state under release of energy. Due to the weak SOC induced spin conservation, this implies that for the transition to be possible, the spin pair has to have singlet content before the transition, i.e., it must not be orthogonal to the singlet state within the spin pair Hilbert Space. This example for a spin-selection rule is called Pauli blockade because it blocks electronic transitions due to the Pauli exclusion principle.

Spin selection rules can govern electronic transitions of charges in weak SOC materials in various ways and they exist for many types of energy transitions [36].

Spin selection rules also govern the way exciton excitations decay to a singlet ground state. For instance, when SOC is weak, excited singlet states can decay radiatively (this is called fluorescence) while the decay into a triplet is unlikely (yet still with finite probability as SOC is never entirely vanishing) and when it occurs, the radiative decay of triplet excitons into the singlet ground state is very slow (this is called phosphorescence) due to the same reasons. For optical excitation, the same spin-selection rules apply since the spin of a photon is readily absorbed into the angular momentum of an excitation. Thus, in an

optically excited molecule, the vast majority of polaron pairs are in the singlet state as they are predominantly generated from geminate pairst. The Jablonski diagram shown in Fig. 1.3 demonstrates the possibilities for excited charge decay. Breaking of selection rules via the intersystem crossing is possible only due to spin-orbit coupling of the electron spin and the orbital angular momentum. Internal conversion is a nonradiative process allowing charges in singlet states to jump to another singlet energy level with a roughly equivalent vibrational energy level [33,34]. The charge wave functions can overlap with the nuclei and thus have the probability to couple to nuclear spin energy transitions. It is this that drives charges to eventually change their energy state over larger energy ranges. Generally speaking, a charge that sits in an excited vibrational state will quickly relax (dashed lines in Fig 1.3) to the lowest vibrational state of a given energy band on tens of fs time scales ($\sim 10^{-14}$ s) [33].

During EPR measurements charges are driven between states with $\Delta m_s = \pm 1$, where m_s is the magnetic spin quantum number. When EPR drives transitions in weakly spin-spin coupled pairs of electron spin with $s = 1/2$, transitions between singlet and triplet manifolds [35] are possible as the driving microwave field induces a perturbation Hamiltonian H' that is not an eigenvector of the product states $|\uparrow\uparrow\rangle$, $|\uparrow\downarrow\rangle$, $|\downarrow\uparrow\rangle$, $|\downarrow\downarrow\rangle$, of a weakly spin-coupled polaron pair. The transition probabilities R will then be determined by Fermi's golden rule

$$R = \frac{2\pi}{\hbar} |\langle f|H'|i\rangle|^2 \rho. \tag{1.1}$$

Note that in presence of strong spin-spin interaction like exchange interaction, J, or dipolar interaction, D, pairs of $s = 1/2$ assume the singlet triplet basis $|T_+\rangle = |\uparrow\uparrow\rangle$, $|T_0\rangle = \{|\uparrow\downarrow\rangle + |\downarrow\uparrow\rangle\}/\sqrt{2}$, $|S_0\rangle = \{|\uparrow\downarrow\rangle - |\downarrow\uparrow\rangle\}/\sqrt{2}$, $|T_-\rangle = |\downarrow\downarrow\rangle$, and for those eigenstates, singlet-to-

triplet transition probabilities are vanishing, while pure triplet-to-triplet transition probabilities are even higher to the uncoupled case.

1.4 Dissertation Overview

In the following chapters, experiments are presented in which PFO thin films with various morphological order states are subjected to charge carrier injection and then investigated with regard to the nature of spin-dependent electronic processes which affect the magneto-optoelectronic properties of these materials. The idea behind these experiments is to resonantly manipulate, magnetically, the spin eigenstates of polaron pairs that exist under nonequilibrium conditions so that spin-dependent electronic transitions of charge carriers are changed and the changes of these rates are then detected via current measurements. Once such electrical detection of magnetic resonance (EDMR) is seen, the current in a polymer device becomes an observable of coherent and incoherent spin motion and the electronic and spin-transitions times, spin-interactions, strengths as well as the associated overall physics of observed spin-dependent transitions becomes apparent and can then be investigated with regard to its dependence on materials and device conditions under which they occur. These experiments ultimately reveal the qualitative types of spin-dependent transitions processes in PFO, spin-spin and spin-lattice relaxation times, g-factor values and distributions, hyperfine field strengths and distributions, spin-orbit, dipolar, as well as exchange couplings.

Compared to previous studies of other π-conjugated polymers focusing the same spin-related observables [20,27,36–40], the study presented here explores the particular influence of materials disorder. In summary, **Chapter 2** covers qualitative models for spin-

dependent processes relevant for this study and the associated spin-Hamiltonians that form the theoretical basis for the experiments discussed and it also explains the continuous (cw) and pulsed (p) EDMR experiments that are carried out in order to detected those mechanisms and how lineshape interpretations of EDMR signals are interpreted appropriately. **Chapter 3** will address the materials and device preparation techniques and procedures for this study. C**hapter 4** focuses on the technological details of the presented experiments. Experimental parameter, equipment, and procedure details including signal analysis and magnetic resonance pulse sequences are outlined and details of the sample preparation are explained. **Chapter 5** discusses the characterization of polyfluorene pahses. **Chapter 6** discusses the specific spin-dependent processes that are hypothesized for polyfluorene. In **Chapter 7**, cw EDMR data are presented that were collected at multiple frequencies using coplanar waveguides for the determination of hyperfine strengths and spin-orbit coupling strengths. **Chapter 8** discusses coherent spin manipulation effects and their implications for the measurement of transverse and longitudinal spin-relaxation times T_1 and T_2. **Chapter 9** discusses electron spin echo envelope modulation experiments that were conducted on polyfluorene using EDMR in order to probe how the nuclear environment affecting charge carriers differs between phase morphologies of polyfluorene.
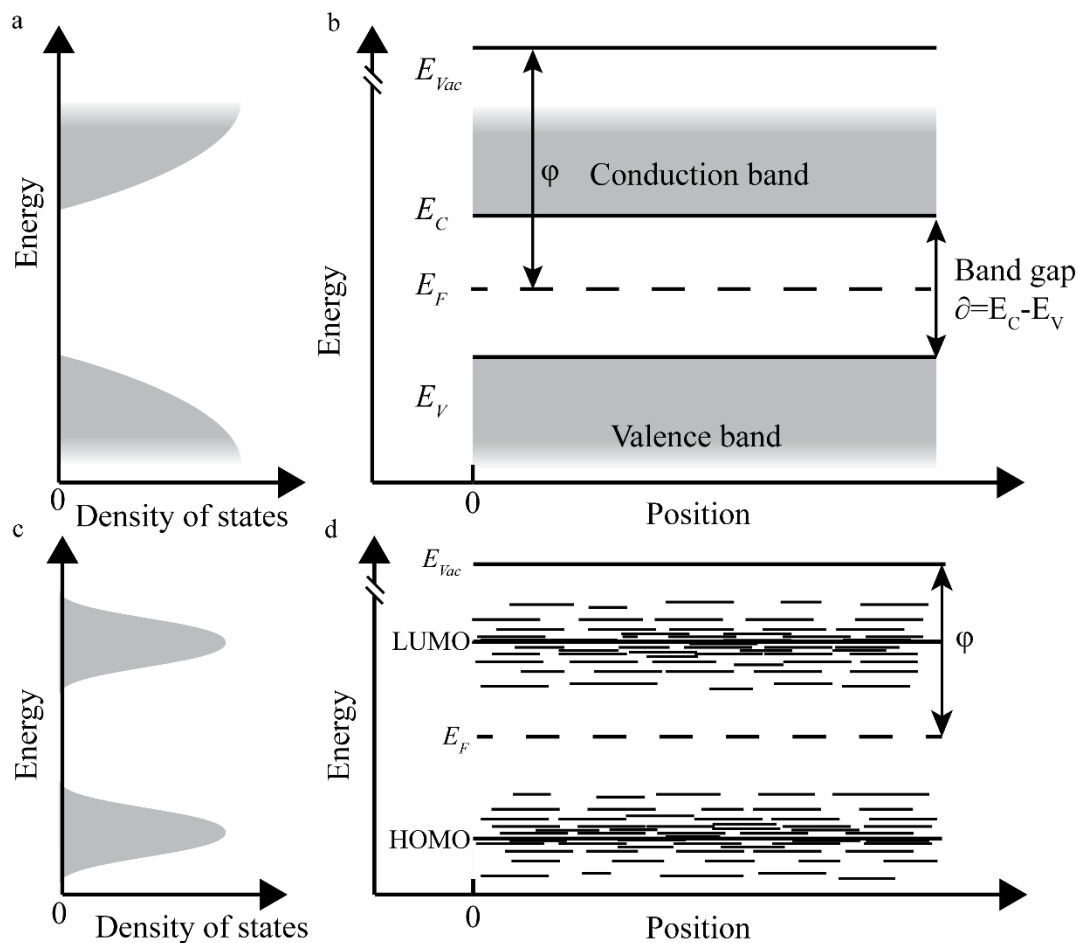
Figure 1.1: Illustrations of the differences between a plot of the density of states (a) and the band diagram (b) of an inorganic semiconductor with a prototypical organic semiconducting material [(c) and (d), respectively]. The density of energy states distributions in organic semiconductors defines the LUMO and HOMO levels (c and d). This figure is adapted from D. Waters [36].
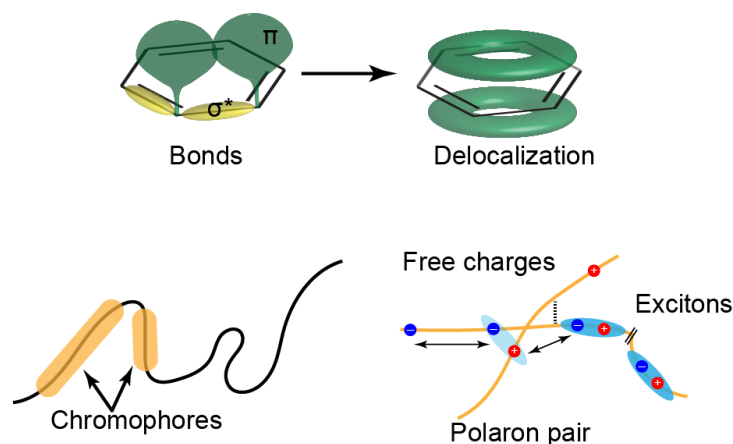
Figure 1.2: Sketches illustrating the how sp^2 hybridization (top left) leads to orbital overlaps (top right) and how it turns into the delocalization over a monomer unit (bottom left). The monomer delocalization leads to delocalization of charge over unbroken chain segments called chromophores. The panel on the bottom right depicts free charges along a polymer chain and how they become weakly coupled (light blue halo) polaron pairs when they get close enough to one another on adjoining chains. Excitons are also shown in darker blue halos to depict their strong coupling.
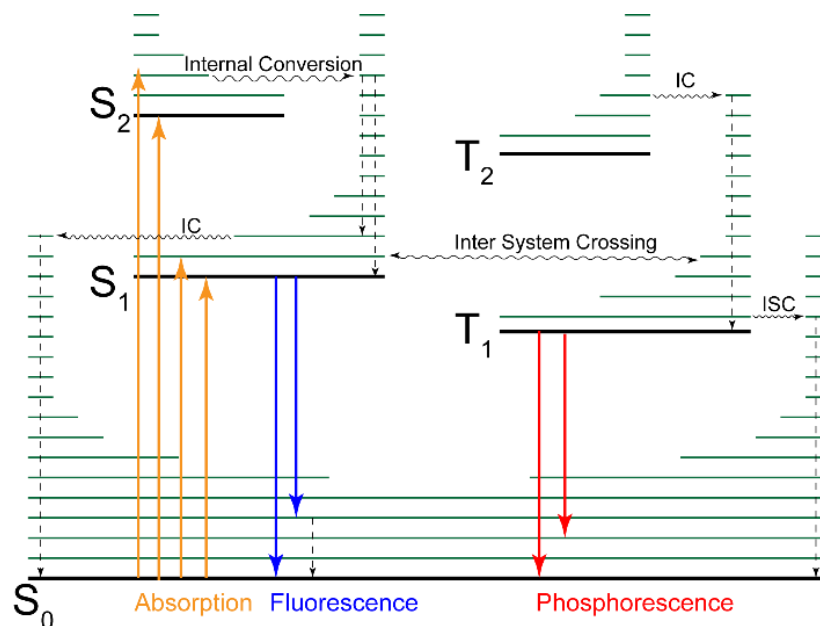
Figure 1.3: A Jablonski diagram showing the energy levels (black) that charges can occupy and transition arrows for certain absorption and emission processes. The dashed arrows represent vibrational energy (green lines) losses that do not produce photons. The wavy lines are labeled either internal conversion (IC) or intersystem crossing (ISC). Absorption (yellow) of a photon requires the charge to be excited from the singlet ground state into an excited singlet state due to spin selection rules, and the fluorescence (blue) can decay from the lowest vibrational energy of an excited state as the vibrational energy losses are on a faster time scale than emission (10^{-12} to 10^{-9} s) [1]. Decay from the excited triplet state to the ground state is allowed only when spin obit is present to allow ISC. This figure is adopted from reference [33].

CHAPTER 2

STUDYING SPIN-DEPENDENT ELECTRONIC PROCESSES

IN POLYMER THIN-FILMS

This chapter focuses on the techniques used in this study to determine said spin properties, how they work and what they tell us. The theoretical foundations of the studied systems will be discussed and the qualitative nature of the spin-processes that were relevant for this study are explained.

2.1 Fundamental Principles of Magnetic Resonance Spectroscopy

Historically, the rapid and revolutionary development of magnetic resonance spectroscopy began when nuclear magnetic resonance (NMR) was first demonstrated in 1945 by Bloch and Purcell [41,42], based on the seminal work by Rabi in 1936 [43,44], while a Russian doctoral student, Zavoisky, had detected a first electron paramagnetic resonance (EPR) signal a year prior [45]. Electron spin resonance (ESR) is synonymously used for EPR. During these early years of magnetic resonance spectroscopy, both NMR and EPR measurements were conducted solely as continuous wave (cw) adiabatic field sweep experiments.

Cw spectroscopy helped to gain significant insight into the microscopic nature of

paramagnetic systems, for both nuclear and electron spins. The idea behind a cw magnetic resonance experiment is to drive spins between two energy levels that are Zeeman split using a polarizing magnetic field that creates multiple energy levels dependent on the spin of a charge. Lock-in detection in combination with the radiation field- amplitude, phase, or magnetic field modulation can be used to improve signal to noise ratios. Standard cw magnetic resonance spectroscopy is used predominantly to measure resonance line centers and resonance line shapes, which depend on hyperfine field- and spin-orbit, dipolar, and exchange interactions, Landé g-factors, (a unitless constant relating the spin of a particle to its magnetic moment) and distributions of all these parameters. For lock-in detected cw magnetic resonance spectroscopy, it is important to note that, due to the inherent differential nature of lock-in detection, amplitude and magnetic field modulation experiments lead to absorption and absorption derive spectra, respectively.

Traditional EPR is measured using inductive detection, i.e., by measuring the amount of reflected microwave radiation on bulk samples which means the material that contains the paramagnetic centers on which the experiment is conducted. These often include systems suspended in a solution, or in a condensed matter matrix. For a magnetic resonance experiment, a sample is placed in the center of an electromagnetic resonator into which a polarizing field is coupled via wave guides or electromagnetic transmission lines. Resonators (usually near-field cavities) are then critically coupled to radiation sources with the samples inserted and this critical coupling is then diminished and no or less radiation is reflected from the cavity when a sample is brought into magnetic resonance, i.e., when the splitting of the paramagnetic states matches the photon energy of the radiation.

B_0 modulation cw EPR is where a steady excitation field is applied to a sample while

the polarizing magnetic field is swept through the resonance condition adiabatically (as for most cw magnetic resonance spectroscopy techniques) with an oscillating modulation field (B_m) that is applied parallel to the adiabatically swept steady state field. When magnetic resonance conditions are established, the modulation of B_0 leads to a modulation of the reflection signal at the modulation frequency and when the dynamics of the reflection signal is then filtered off, all harmonic contributions except a narrow range around the modulation component, a strongly noise reduced signal can be measured. Lock-in detected magnetic resonance signals increase linearly with the modulation amplitude as long as they are not over-modulated. Over-modulation of the modulation field, i.e., the use of a modulation amplitude that exceeds the line width of a magnetic resonance results in broadening artifacts (i.e., a measured magnetic resonance line is broader than without over modulation). In order to avoid over modulation, B_m should be kept at less than a third of the overall linewidth [46]. In essence, B_m should always be as large as possible to observe an optimal signal-to-noise ratio, yet as small as necessary at the same time in order to avoid over modulation.

Fig 2.1 illustrates both the principle of magnetic resonance spectroscopy based on radiation absorption measurements of Zeeman split spin states for two different g-factors (red and blue lines) as well as a cw magnetic resonance spectrum that would be measured when two inhomogeneously broadened resonances were obtained via magnetic field modulated lock-in detection. Inductively detected magnetic resonance spectroscopy must be conducted at magnetic fields high enough to produce sufficient thermal spin polarization such that a radiation field can couple to a studied spin ensemble. Thus, executing magnetic resonance spectroscopy at higher frequencies and higher magnetic fields is typically

preferable and the field and frequency ranges chosen for most magnetic resonance spectrometers are solely limited by cost considerations. As the nuclear magneton is more than three orders of magnitude smaller compared to the Bohr magneton, NMR conducted on nuclei is typically limited by the cost of magnetic field generation while EPR spectrometers are limited by strong enough radiation source in the microwave to THz domain. Thus NMR is typically conducted at radio frequency (RF) bands between 100MHz and 1GHz at magnetic fields ranging from 2T to 20T, while EPR is predominantly conducted in the microwave range between 3GHz and 600GHz at magnetic fields between 100mT and 20T [45].

For the magnetic resonance spectroscopy of charge carriers in organic semiconductors using EPR, there are several crucial challenges. First, organic semiconductors exist predominantly only as thin films and since the sensitivity of inductively detected magnetic resonance spectroscopy depends on the fill factor of a sample, i.e., its volume, low sensitivity is given. Secondly, due to the weak SOC in these materials, the magnetic resonances (g-factors) of most, even qualitatively different electron spin states occur at the same spectral position and therefore, they are not spectroscopically distinguishable. In particular, electron spins influencing the optoelectronic and magneto-optoelectronic properties of the studied materials cannot be distinguished from those which do not play a role, including paramagnetic defects which are not even within the studied materials, such as defects in the glass substrate. Finally, EPR does not allow a means to observe how a paramagnetic center is involved and how it influences spin-dependent electronic transitions [39,45,47].

2.2 Theoretical Foundations of Magnetic Resonance Spectroscopy

In the previous sections, the discussion of magnetic resonance spectroscopy was highly nonquantitative. Therefore, in the following, a detailed quantitative discussion of magnetic resonance spectroscopy, covering the theoretical foundations of this technique, will take place which will establish the connections between spin-phenomena that are detectable with magnetic resonance spectroscopy and the physical nature of the studied paramagnetic systems.

2.2.1 The Rotating Frame Description of Magnetic Resonance

The magnetic moment of an electron exposed to a magnetic field with strength B_0 will precess about the direction of this field with a Larmor frequency $\omega_0 = -\gamma\, B_0$, with γ being the gyromagnetic ratio that is defined as $\gamma = 2\pi\mu_B g_i/h$, with g being the g-factor and μ_B the Bohr magneton. The vacuum value for the electron's gyromagnetic ratio is $\gamma_e =$ 28.034952GHz/T.

Manipulating the orientation of a spin means changing the angle between the precessing spin and the applied magnetic field. This can be achieved by magnetic resonance, i.e., by application of a magnetic field B_1 that rotates at the Larmor frequency within the geometric plane that is perpendicular to the direction of B_0 [48,49]. As the rotating frequencies for B_1 have to be well in the GHz range for electron spins, microwave radiation can be used to achieve such conditions. The reasons why the orientation of B_1 must be perpendicular to B_0 can be understood by viewing the problem from a reference frame which rotates at the same frequency as the rotating magnetic field B_1. When this rotating frame rotates at the same frequency as the spin orientation, the spin orientation is

fixed within the rotating frame, so it does not precess anymore. This however implies that there is no constant magnetic field B_0 that would drive a precession [50] and thus, the description of the electron spin motion is reduced to a simple constant magnetic field B_1 which now causes the spin to precess away from the axis parallel to the B_0-field direction [49].

Fig. 2.2 a) is an illustration of an electron spin that precesses in presence of a constant magnetic field B_0 that is aligned to a z axis, and an oscillating magnetic field B_1 that is perpendicular to B_0, in the laboratory frame K. The electron spin precesses about the z-axis with a Larmor frequency ω_0 in the xy plane. Fig. 2.2 b) depicts the same situation from the rotating frame, K', with the oscillating magnetic field being at rest so that the magnetic field B_1 is seen to be constant to the spin, **S**. In the rotating frame, the spin will experience a torque that causes precesses about the stationary field B_1.

2.2.2 The Quantum Mechanical Description of Magnetic Resonance

The main purpose of any spectroscopy technique is to gain insights into the nature of the physical system that is subjected to this method. As interactions with the systems are carried out over a spectrum of oscillation frequencies, the "resonances" are revealed, which means the eigenenergies of the system and thus, the eigenvalues of the Hamiltonian associated with the system. As the physical nature of a given object determines it Hamiltonian, knowing the Hamiltonian or parts thereof allows for insights into the physical nature of an unknown object [51]. If this fundamental principle of spectroscopy techniques is now applied to magnetic resonance spectroscopy, it becomes clear that an in-depth discussion of the Hamiltonia of interaction spin systems is crucial for the understanding of

experiments results.

For the weakly SOC systems on which this study is focused, only the spin Hamiltonian is relevant while the electronic Hamiltonian is only marginally important for description of magnetic resonance phenomena. In general, this spin Hamiltonian

$$\widehat{H}'(t) = \widehat{H}'_0 + \widehat{H}'_1(t) \tag{2.1}$$

consists of two main contributions, time-dependent component $H_1(t)$ that is due to the excitation radiation, and the time-independent component

$$\widehat{H}'_0 = \widehat{H}_Z + \widehat{H}_{HF} + \widehat{H}_J + \widehat{H}_D \tag{2.2}$$

that contains the entire complexity of the investigated spin system and its interactions with its microscopic environment, including, Zeeman and SOC which both are expressed by $\widehat{H}_Z$, spin-dipolar $\widehat{H}_D$, spin-exchange $\widehat{H}_J$, as well as nuclear-spin (so called hyperfine $\widehat{H}_{HF}$) interactions.

The energy scales of the Zeeman interaction depends on the magnetic field and ranges typically $\sim 10^{10}$ Hz or 0.0004 eV. Typical values of the other contributions for the polaron systems studied here follow in order of strength: hyperfine interactions ($\sim 10^7$ Hz), spin-orbit ($\widehat{H}_{SOC}$) coupling ($\sim 10^6$ Hz) that is part of the Zeeman term, dipolar ($\sim 10^5$ Hz), and exchange ($\leq 10^5$ Hz) for interactions at x-band frequencies [50]. In the following, these contributions are discussed on an analytic level.

2.2.3 Zeeman and Spin-Orbit Interaction

The Zeeman interaction in the presence of an external magnetic field has been discussed above and it is illustrated by Fig. 2.1 as being proportional to the externally applied magnetic field B_0 following the Zeeman Hamiltonian

$$\hat{H}_Z = \mu_B g \hat{\boldsymbol{S}} \cdot \boldsymbol{B_0}. \tag{2.3}$$

In the presence of several paramagnetic centers, i.e., when pairs of charge carriers in an organic semiconductor form, the different Zeeman contributions can just be added to

$$\hat{H}_Z = \sum_{i=a,b} \mu_B g_i \hat{\boldsymbol{S}}_i \cdot \boldsymbol{B_0}. \tag{2.4}$$

with g_i being the Landé-factor of spin $\hat{\boldsymbol{S}}_i$, μ_B the Bohr magneton, and $\boldsymbol{B_0}$ the external magnetic field vector. The Zeeman interaction was first studied in 1896 by Pieter Zeeman, when he discovered a splitting of an atomic emission line that scaled linearly with applied magnetic field strength [52].

In uncoupled paramagnetic systems, magnetic resonance can be established simply by resonance between the Zeeman levels and an applied electromagnetic radiation whose frequency f_{mw} must be equal to the change in energy between states such that.

$$\Delta \hat{H}_Z = \Delta m_s g \mu_B B_0 = h f_{mw}. \tag{2.5}$$

Due to weak SOC, the g-values in organic materials generally differ from the free electron value of $g_e = 2.00231930436182\ldots$ [35] by less than $\mathit{\Delta}g = 0.01$ [50]. Most effective g-factors in organic semiconductors are actually highly anisotropic and thus, they require to be expressed by g-tensors [30] which can be obtained by second order perturbation theory that takes into account the spin orbit interaction, $\hat{H}_{SOC}$. A symmetric (3 by 3) tensor [50] is given by

$$\boldsymbol{g} = g_e \boldsymbol{I} + 2\lambda \boldsymbol{\Lambda} \tag{2.6}$$

with

$$\Lambda_{ij} = \sum_{n \neq 0} \frac{\langle \psi_0 | L_i | \psi_n \rangle \langle \psi_n | L_j | \psi_0 \rangle}{E_0 - E_n} \tag{2.7}$$

where $\boldsymbol{I}$ is the identity matrix, and λ is the spin-orbit coupling constant that relates $\boldsymbol{S}$ to $\boldsymbol{L}$. $\mathit{\Lambda}$ is the symmetric tensor that is defined by Eq. 2.7 through the wave functions of an

electron for different states, E_n is the energy level for the nth excited state. The off diagonal elements of the tensor are rather small in light organic compounds (Λ scales proportionally to Z^4). The spin-orbit coupling manifestation is relatively weak at frequencies for X-band and lower as the observable differences to g_e scale with frequency [3]. Since the magnitude of the Zeeman interaction scales with magnetic field but the hyperfine fields (see next section) do not, conducting magnetic resonance spectroscopy of the same spin resonances at various magnetic fields and frequencies is the most reliable way to distinguish SOC contributions from hyperfine field contributions to spin resonance line width [3,53]. For the magnetic resonance spectra discussed in this study, completely isotropic (not directionally dependent) g-values were assumed such that the g-tensor can be approximated by the average of the main axis elements

$$g_{iso} = \frac{1}{3}(g_{xx} + g_{yy} + g_{zz}).$$ (2.8)

The correctness of this assumption can be verified by inspection of the resonance line symmetry, even in the absence of crystalline order and an angular distribution of the molecular orientation. If the observed paramagnetic systems are anisotropic, the magnetic resonance lines associated with an ensemble of these species will be highly asymmetric, representing the superposition of a so-called powder-distribution [35].

2.2.4 Electron-Spin Hyperfine Interaction

Hyperfine interaction is the interaction of nuclear magnetic moments with the magnetic moments of electron spins. Since hyperfine interaction involves only nuclei with nonvanishing spin, hyperfine fields in organic molecules are very strong due to the all abundant hydrogen and highly distributed due to structural disorder. This typically results

in an unresolved Gaussian line broadening of spin EPR lines. In general, hyperfine contributions have two components

$$\widehat{H}_{HF} = H_{FC} + H_{DD} \tag{2.9}$$

in an interaction Hamiltonian due to the interaction between an electron spin $\widehat{\boldsymbol{S}}$ and a nuclear spin $\boldsymbol{I}$ consists of an isotropic Fermi contact interaction and an electron-nuclear dipole-dipole element, the so-called anisotropic hyperfine interaction which both can be combined into one expression

$$\widehat{H}_{HF} = \widehat{\boldsymbol{S}}\boldsymbol{A}\boldsymbol{I}. \tag{2.10}$$

The Fermi contact interaction can be written as

$$H_{FC} = a\widehat{\boldsymbol{S}} \cdot \boldsymbol{I} \tag{2.11}$$

in which the coupling constant

$$a = \frac{4\pi\mu_0}{3h} g_e \mu_B g_n \mu_n |\rho_s(0)|^2 \tag{2.12}$$

is governed by the particular geometrical nature of the electron wavefunction overlap with the nucleus that. $\rho_s(0)$ is the electron spin density at the nucleus. The reference frame of Eq. 2.10 is assumed to be located at the origin. The mathematical description of the Fermi contact interaction is analogous to the spin-exchange interaction term of isotropic Heisenberg exchange, the fundamental origin of which is solely due to electrostatic interaction [54].

The anisotropic dipole-dipole coupling between an electron and a nucleus must be expressed as a tensor product

$$H_{DD} = \widehat{\boldsymbol{S}}\boldsymbol{T}\boldsymbol{I} \tag{2.13}$$

with

$$T_{ij} = \frac{\mu_0}{2h} g_e \mu_B g_n \mu_n \left\langle M_0 \left| \frac{3r_i r_j - \delta_{ij} r^2}{r^5} \right| M_0 \right\rangle. \tag{2.14}$$

where M_0 is the molecular orbit about the nucleus to which the spin is dipole-dipole coupled [20]. When the anisotropy of **g** is small, the dipole-dipole tensor can be approximated by a diagonal tensor. Hyperfine interactions in organic semiconductor lead to random, inhomogeneous broadening of the intrinsic, Lorentzian resonance line shapes throughout ensembles of paramagnetic center, resulting in macroscopically detected Gaussian line shapes. For the magnetic resonance of charge carriers in organic semiconductors (for both, electrons and holes) hyperfine broadened Gaussian curves are typical. Different charge carrier types will have different resonance line width, as the associated different types of electron wavefunctions will interact differently with the proton ensembles that surround them.

2.2.5 Electron Spin-Spin Interactions

Adjacent electron spins can interaction via magnetic dipolar interactions and as exchange interaction. Akin to the electron-nuclear dipolar interaction discussed above, electron-electron dipolar interaction is highly anisotropic and the interaction Hamiltonian has a similar form as Eq. 2.13 with a dipolar interaction tensor, **D**. In contrast, spin exchange interaction is similar to the Fermi contact interaction and thus, isotropic with an exchange constant J [35]. The dipolar interaction between two electrons in the high-field limit can be approximated by:

$$\widehat{H}_D = \boldsymbol{D}(3S_a^z S_b^z - \widehat{\boldsymbol{S}}_a \widehat{\boldsymbol{S}}_b) \tag{2.15}$$

with

$$D_{ij} = \frac{\mu_B{}^2 \mu_0}{2h} g_a g_b \langle \frac{3r_i r_j - \delta_{ij} r^2}{r^5} \rangle. \tag{2.16}$$

Thus, dipolar interaction is inversely proportional to r^3. The dipolar tensor **D** can also

be "parameterized" [55] in terms of:

$$D = \frac{3}{2}D_{zz}, E = \frac{1}{2}(D_{xx} - D_{yy}) \tag{2.17}$$

$$\mathbf{D} = \begin{pmatrix} \frac{1}{3}D - E & 0 & 0 \\ 0 & \frac{1}{3}D + E & 0 \\ 0 & 0 & -\frac{2}{3}D \end{pmatrix}. \tag{2.18}$$

When the value of D can be determined spectroscopically, it can be used to find the distances between interacting spin species as D_{zz} is proportional to the inverse of the cube distance between charges. D and E are dubbed the zero-field splitting parameters which govern the energy eigenstates of a pair of dipolar interacting electrons in absence of an external magnetic field that adds a Zeeman term to the interaction Hamiltonian. Fig. 2.3 illustrates this situation by plotting the eigenenergies of the dipolar coupled spin pair as a function of the applied magnetic field B_0.

The plot shows the influence of the zero field splitting parameters on the eigenstates at low magnetic fields when the strength D determines the separation from the center of the spin pair states with spin 1 (triplet) to the singlet with spin 0. The separation of the two triplet spin 1 states is twice that of the E, the rhombicity value calculated from the dipolar tensor [35]. It also shows how an excitation pulse of a certain strength can drive between two different spin states at different polarizing magnetic field strengths. D and E can be attained experimentally by modeling the half field signal, i.e., the $\Delta m = 2$ transition [21], which allows for the determination of the dipolar coupling of the Hamiltonian [55] using the expression

$$\hat{H}_D = D\left|\hat{\mathbf{S}}_z^2 - \frac{1}{3}S(S + 1)\right| + E(\hat{\mathbf{S}}_x^2 - \hat{\mathbf{S}}_y^2) \tag{2.19}$$

The final contribution to the Hamiltonian due to spin-spin interaction is the exchange

interaction. The exchange Hamiltonian takes into account the wave function overlap of two charge carriers in close proximity to one another. In polymers, the wave function of a charge carrier can spread over several monomer units as long as there is no break in the conjugation backbone [56]. Typically the isotropic Heisenberg exchange is given by

$$\widehat{H}_J = J\widehat{S}_a \cdot \widehat{S}_b \tag{2.20}$$

In which J is the exchange integral that takes into account the spatial component of the electron spin's wave functions. Similar as for spin-dipolar interaction, spin-exchange governs the spin-eigenstates of an interacting pair of spins in the low-field regime where Zeeman energies are smaller than the exchange interaction. In this case, J represents half of the energy difference between singlet and triplet spin state. Exchange interaction is very strong in excitonic states where the interacting spins have significant wave function overlap. In polymers, triplet excitons have typically lower eigenenergies as they are not as tightly bound as the singlet excitons, which have antisymmetric wave function [50].

Exchange interaction, like dipolar interaction, is strongly dependent on the distance between the two charge carriers. However, in contrast to dipolar interaction, the magnitude of the exchange integral, rather than the distance of the center of masses of the two electron wavefunctions, determines the magnitude of the interaction and furthermore, exchange interaction J typically follows an exponential distance dependence $J = J_0 e^{-\beta r}$ rather than the r^{-3} dependence mentioned above for dipolar interaction. Simulations for exchange integrals of charge carriers in π-conjugated polymers done by Sperlich [35] show that the exchange strength is dominant compared to other interaction types for distances $r < 2$nm (exciton range) while dipolar strengths are stronger for distances above that threshold (polaron pair range). Exchange strength becomes less than the strength of the magnetic

field of Earth at 2 nm separation; the dipolar strength falls below that threshold at nearly 4 nm [35].

2.2.6 The Time-Dependent Excitation Hamiltonian

The time dependent component of the Hamiltonian is essentially an additional Zeeman interaction term for the oscillating magnetic excitation field which is controlled during a magnetic resonance experiment. In the rotating frame, even this term can be transformed into a time independent Hamiltonian

$$\hat{H}_1 = \mu_B g \hat{\boldsymbol{S}} \cdot \boldsymbol{B_1} \tag{2.21}$$

as long as the magnitude B_0 of the Zeeman Hamiltonian is adjusted or erased according to the reference frame transformation. Under these conditions, Eq. 2.21 can be treated as a static magnetic field in the same way as the Zeeman term. $\boldsymbol{B_1}$ is perpendicular to $\boldsymbol{B_0}$ and oscillates at the Larmor frequency generated by $\boldsymbol{B_0}$ when the $\boldsymbol{B_1}$ frequency is on resonance.

2.3 EDMR for the Spectroscopy of Polymer Thin Film Materials

EDMR is a magnetic resonance spectroscopy technique that is based on the observation of electric currents in condensed matter systems which are controlled by magnetic resonantly manipulated spin-dependent transition rates [39,57–59]. Compared to inductively detected magnetic resonance spectroscopy, EDMR is highly sensitive as it has been demonstrated to be sensitive to individual electrons [17,60,61] and nuclear spin states [62], many orders of magnitude higher than EPR and NMR which typically needs at least 10^9 and 10^{15}, respectively, to allow for the detection of spin induced signals [63]. Thus, EDMR allows for the use of thin film devices much like those used in modern

photovoltaic and display application. EDMR also allows for the observance of spin states under device operation conditions and it can also be used at room temperature and very low magnetic field when virtually no thermal equilibrium spin polarization exists. The signal of many known EDMR detected states is not dependent on spin polarization but spin selection rules such as spin-permutation (singlet vs. triplet character) as it is the case for the Pauli Exclusion Principle. Furthermore, while EDMR is very sensitive to paramagnetic states which influence a materials conductivity, it is mostly insensitive to paramagnetic states which do not affect a materials charge transport. This selectivity makes EDMR fundamentally well suited for the exploration of spin-selection rules.

EDMR spectroscopy is typically detected by monitoring changes to steady state DC currents. If spin-dependent charge carrier transitions are present in a material, then detectable current changes will occur when a magnetic resonant change of spin states is induced. EDMR has been used to investigate spin-dependent charge carrier transitions in semiconductor materials for more than half a century [38,57,58,64–70] and many qualitatively different mechanisms responsible for the observed EDMR signals have been reported. Those mechanisms that are relevant for this study will be discussed later in this chapter.

2.4 Pulsed Electrically Detected Magnetic Resonance

A short time after the discovery of NMR, first pulsed magnetic resonance experiments were conducted by Erwin Hahn [71] in the form of nuclear spin echoes. Pulsed magnetic resonance experiments are inherently nonadiabatic, where powerful excitation fields are very shortly applied to an investigated system while B_0 is held constant. Pulsed excitation

brings the probes' spins to nonenergy eigenstates which will propagate according to Schroedinger's equation after the excitation until the quantum coherence decays spontaneously in the course of a spin-relaxation event. The coherent propagation of a polarized spin ensemble can be detected transiently after the pulsed excitation and this allowed for coherent spin motion effects to be observed. Since coherent spin motion is deterministically governed by spin-Hamiltonian of a paramagnetic system and the spin-Hamiltonian is characteristic for the qualitative and quantitative nature of the observed system, pulsed magnetic resonance offers much more experimental access to the studied spin systems. Furthermore, since the observed coherent spin motion-effects decay as the spin ensemble loses its coherence, pulsed spin resonance techniques allow for the straight-forward measurement of relaxation times [50].

While the development of pulsed NMR followed the development of cw NMR within less than five years and pulsed EPR had followed cw EPR by the early 1970s, the development of pulsed EDMR lagged cw EDMR spectroscopy by nearly four decades. Cw EDMR techniques have been used since the mid-1960s [64], yet the first electrical detection of coherent spin motion with pEDMR did not take place until the early 2000s [72]. One of the various reasons for this delay was the inability to conduct pEDMR like pEPR experiments namely by coherent spin motion through real-time transient observation of electric currents. As spin-selection rules are most pronounced in materials with small mobilities, it was the dielectric relaxation times that prevented such experiments.

Eventually, pEDMR experiments were demonstrated using a pump and probe scheme [47], for which changes of a DC current are monitored due to magnetic resonant

excitation of paramagnetic center which influences spin-dependent transitions. For these experiments pEPR excitation consisting of one or more pulses is used to change a spin ensemble of charge carriers into a coherent noneigenstate. Then, on a time scale long enough to not be filtered by dielectric relaxation, current changes are probed between the moment they appear after the pulse and the time when the current returns to its steady state. The integration of these current change transients produces a value for the charge that was electrically transmitted through an EDMR sample. This represents a projection of the coherent spin states onto an operator that is defined by the nature of the spin-dependent process that controls the material's conductivity [37,47,73]. Coherent spin-motion can be observed following this scheme, for instance, when this pulse and probe scheme is repeated with consecutively longer excitation pulses. In this case, the charge measurement that is always a projection of the coherent spin state at the end of the excitation, will reflect the propagation of the spin system as a function of time during the pulsed spin excitation.

As an example, when a Pauli-blockade is the spin-selection rule that controls a measured spin-dependent charge carrier recombination current, then a spin-permutation symmetry operator $|S\rangle\langle S|$ projects a charge carrier spin state onto the transmitted charge. For a pEDMR experiment using such a spin-dependent current, charges are electrically injected into the device and the spin-pairs are formed, with ½ likelihood that the pure triplet states $|\uparrow\uparrow\rangle = |T+\rangle$ and $|\downarrow\downarrow\rangle = |T-\rangle$ are formed and an equal probability that the other two eigenstates $|\uparrow\downarrow\rangle$ and $|\downarrow\uparrow\rangle$, with mixed singlet and triplet symmetry, are generated [33,37]. Rate equations outlined in the supplementary information of Ref. [74] show that in the steady state, the pure triplet states are pumped to very high densities as the mixed states have much shorter lifetimes caused by the spin-dependent transition matrix elements.

A pulsed microwave excitation of either one of the pair partners will now change the density pure triplet states into state with mixed symmetry while in absence of mixed symmetry states, no triplet states are generated. Thus, the densities of mixed states and pure triplet states will change by Δn and $-\Delta n$, respectively. The transient of the conductivity change from the steady state after the magnetic resonant excitation will therefore follow a biexponential form

$$\Delta\sigma = 2\mu e\tau\Delta n(-d_{pp_s}e^{-(k_s+d_{pp_s})t} + d_{pp_t}e^{-(k_t+d_{pp_t})t}) \tag{2.22}$$

in which σ is the device conductivity, μ is the average free carrier mobility, e is the charge of a free carrier, τ is the free carrier lifetime $k_s + d_{pp_s}$ and $k_t + d_{pp_t}$ are the exciton formation and dissociation rates for singlets and triplets, respectively [74]. This expression was derived from a set of ordinary differential equations that were obtained by simplification of a stochastic Liouville equation [47,73]

$$\partial_t\hat{\rho} = \frac{2\pi i}{h}\left[\hat{\rho}, \hat{H}\right]^- + S[\hat{\rho}] + R\{\hat{\rho} - \hat{\rho}_0\} \tag{2.23}$$

in which $\hat{\rho}$ is the density operator, $\hat{H}$ is the spin-pair's spin-Hamiltonian described earlier in this chapter, S is the stochastic operator which represents the external changes of the ensemble, and R is the spin relaxation term. This equation is detailed in Ref. [47]. For a general review of the theoretical foundations of pEDMR more than a decade after its invention, a large number of studies can be found [47,63].

2.5 Spin-Dependent Electronic Processes in Organic Semiconductor Materials

In the following sections the specific mechanisms that cause magnetic resonance induced changes of spin-dependent electronic transition rates and thus, EDMR signals are

discussed, followed by a discussion of the specific electronic systems in organic semiconductors which allow for such mechanism.

2.5.1 Spin-dependent Electronic Mechanisms That Allow for EDMR Signals

After the first EDMR experiments had been conducted around 1966 by Honig [64], it was Lepine in 1972 who recognized that spin-selection rules of nonequilibrium systems which can be the origin for EDMR signals when he studied magnetic resonantly changed recombination currents at silicon interfaces [75]. Lepine's description of spin-dependent pair recombination assumes that between ensembles of electrons and holes, spin-dependent recombination can occur at any given time between any electron and any hole. The consequence of this situation is that due to thermal polarization that is lifted under magnetic resonance, a change of the recombination current occurs, whose magnitude (the EDMR signal) is quadratically dependent on the thermal spin polarization, i.e., the ratio between the magnetic field B_0 and the temperature [47]. While Lepine's predictions for the temperature- and magnetic field-dependencies of EDMR signals worked for some of the observed EDMR signals, it quickly became apparent that it did not work for most EDMR signals as it failed to account for orders of magnitudes stronger signals which showed to be nearly independent on temperature and applied magnetic field. Other models were quickly proposed to explain the magnitude of the signal [76] yet it soon became apparent that polarization, while possibly affecting conductivity, was not the main source of the observed signal; this led to other explanations using exchange coupled centers in intermediate states and spin-dependent recombination and trapping [47].

2.5.1.1 Spin-dependent Pair Transitions with Intermediate Pairs

The most significant breakthrough for the understanding of the physics of EDMR eventually came from Kaplan, Solomon and Mott (KSM) in 1978 [77]. They introduced the idea of intermediate pairs of electrons and holes that were weakly spin-dipolar and exchange-coupled and whose constituents had to either recombine or dissociate first before they could form other pairs. The KSM model could explain the large signal as well as the temperature and magnetic field dependence. The originally published semiclassical concept paper by KSM self-admittedly failed to take into account several subtle details of the physics of intermediate pairs such as a finite triplet recombination due to finite SOC or the spin-spin coupling and hyperfine coupling influences that could account for an increased accuracy of their model, but the fundamental step for a widely applicable understanding of EDMR signals had been made.

2.5.1.2 Refinements of the KSM Model

After the advent of the KSM model, several derived descriptions for spin-dependent transitions in specific materials systems were developed, most notably the concept for polaron pair (PP) recombination in organic semiconductors that was developed in 1992 by Frankevich et al. [78] which proposed that a hole and electron can form a long-lived KSM pair consisting of Coulombically bound electrons and holes. Others [47] adopted this model under consideration of finite triplet recombination probabilities, spin-spin interactions, and interaction with the local environment. These extensions allowed for more detailed descriptions of the intermediate-spin pair's Hamiltonian which were needed for accurate predictions of cw- and pEDMR experiments.

2.5.2 <u>Spin-Selection Rule Mechanisms in Organic Semiconductors</u>

In spite of existing theoretical descriptions for EDMR spectroscopy, most of which are based on the Pauli-blockade that was treated by KSM, there is a significantly broader range of other spin-selection rules and spin-induced conductivity effects that are not associated with the KSM mechanism. Some of these processes are similar to KSM in that they are based on intermediate pair formation, yet with different spin manifolds as pair partners. Other processes that affect the electric current are entirely unrelated to spin-selection rules. In the following, some of these mechanisms are discussed qualitatively.

2.5.2.1 Single Spin ½ Model

Arguably the simplest model for a spin-dependent process is the single spin ½ transition between paramagnetic states. Hopping transitions between localized charge carrier states can occur when these states are spatially and energetically close enough such that thermal energy can provide their difference as illustrated in Fig. 2.4. When the energy splitting δ_1, δ_2 of the spin states within the two states is different (i.e., due to local spin-orbit or hyperfine field fluctuations), the four transition matrix elements from either spin state of the original to either spin state of the final state are mutually different and thus, the transition is a spin-dependent process. Both δ_1 and δ_2 are much smaller than the thermal energy and their difference, which determines the magnitude of an EDMR signal due to this process, is even orders of magnitude smaller and this is why this process is usually negligible in organic semiconductors. It is more significant in materials with larger SOC. If this process was dominant for the experiments presented in the following chapters, EDMR signals would be highly temperature dependent as would organic

magnetoresistance (OMAR), both of which are not seen to be true [21,36]. Likewise, certain coherent spin-motion effects such as spin-beat oscillation that is observed in electrically detected Rabi-nutation experiments, discussed in section 4.6.2.2 would not be detectable either.

2.5.2.2 The Bipolaron Mechanism

The spin-dependent bipolaron charge transport process is a Pauli blockade controlled intermediate pair process where adjacent, localized pairs of polarons with identical charges (electrons or holes) undergo transitions into doubly occupied charge carrier states, so called polarons. The bipolaron process is closely related to the polaron pair model in that both are KSM processes and both involve localized polaron states. The difference between the two processes is that bipolaron states form from unipolar pairs of charge carriers while polaron pairs are inherently bipolar. The bipolaron model was introduced to give an analytical model for OMAR [23,79] and pEDMR [22]. Due to the similarity of the bipolaron pair process and the polaron pair process with regard to their spin physics, the two mechanisms should show the same coherent spin nutation signatures. This is the reason the existence of the bipolaron pair process has been strongly debated [12] as experimentally it is nearly entirely indistinguishable from the polaron pair process which has experimentally been well corroborated and established as a spin-dependent recombination process [21].

Fig. 2.5 shows a cartoon of the bipolaron process. The charges (electrons) depicted with blue arrows to designate their spin orientation move through the material until they encounter a trapped polaron (a charge with an associated self-induced polarized phonon field) in a localized state, shown with an orange halo. If the two charges are in a singlet

configuration they can couple and form a singlet bipolaron which can then decay to the ground state. The charges are unable to form in a triplet configuration due to Pauli exclusion, and hence no triplet bipolarons are formed.

2.5.2.3 Trion Recombination

The trion model was first proposed in 1958 by Lampert [80] and has since been observed in a variety of materials such as GaAs quantum wells and carbon nanotubes [81,82]. Trions can be considered as charged excitons that contain an extra electron that is strongly coupled to both exciton constituents to form a spin 3/2 particle (see illustration in Fig. 2.6). The trion eventually decays through an Auger-type recombination process where the exciton falls into the ground state (a singlet state) while the remaining polaron absorbs the trion energy and becomes a free charge carrier.

In organic semiconductors, a trion can form from an exciton on a chromophore that also hosts a polaron close enough to develop a wavefunction overlap. To date there has been no spectroscopic evidence of a strongly exchange coupled spin-3/2 system in organic materials. Such evidence could be obtained for instance by spin-Rabi nutation experiments revealing a a $\sqrt{3}\gamma B_1$ nutation component which is absent in all empirical data [21].

2.5.2.4 The Triplet-exciton Polaron Process Model

Related to the trion process is the triplet-exciton polaron (TEP) process, which like the trion process involves transitions of systems with s = 3/2 but only two of the three spin s = 1/2 constituents are strongly exchange coupled (forming an exciton), while the third spin is only weakly coupled to the exciton. Also, unlike the trion process, the TEP has

actually been confirmed experimentally in a variety of organic semiconductor materials. Fig. 2.7 displays an illustration of the TEP process; a polaron is weakly spin coupled to a triplet exciton [83] which results in the triplet returning to the singlet ground state and the polaron returning to the free charge carrier continuum with the excess energy released in the triplet decay. The exciton is strongly coupled on the same chromophore as it is the case for the trion, but the polaron itself is weakly coupled from an adjacent chromophore. As singlet excitons decay much faster than the triplet excitons they do not significantly couple magnetically to free polarons, in contrast to the triplet excitons. While microwave excitation can change the triplet-singlet content, there is likely no intersystem crossing as the energy between singlet and triplet excitons is large (~0.3 eV) [36].

Magnetic resonance, in particular EDMR signals, corresponding to $g = 4$ (the half field signal with $\Delta m \pm 2$) are indications of the TEP process, as only the triplet exciton with spin $s = 1$ and strong dipolar interaction can account for the $\Delta m = \pm 2$ excitation [21]. Furthermore, a full field signal due to the TEP process should reveal a Rabi nutation signal of the free polaron (spin ½) as there will be a $\Delta m = \pm 1$ transition but no coupled adjacent pair partner. As discussed in the following chapters, indications of the TEP process are seen in both studied phases of PFO.

2.5.2.5 Triplet-triplet Annihilation

Under materials conditions with high triplet exciton densities [84], it is possible for two triplet excitons to form weakly coupled pairs similar to polaron pair or the bipolaron pair mechanism [70]. Through spin conservation, this coupled system can decay into an a singlet ground state and a singlet polaron pair [21] and change the polaron pair

population, the polaron pair dissociation rate, and hence the sample conductivity. This process is depicted qualitatively in the sketch of Fig. 2.8. To probe for the triplet-triplet annihilation process, electrically detected magnetic resonantly induced Rabi-nutations are an unambiguous proof. If the triplets are weakly coupled, a single nutation frequency $\sqrt{2}\gamma B_1$ is expected and possibly a beat oscillation at twice this frequency. If the triplets are strongly bound, a spin 2 species is present and that will display a Rabi nutation frequency at both $\sqrt{2}\gamma B_1$ and $\sqrt{6}\gamma B_1$ [21,36]. None of these signals are observed in either PFO phase.

2.5.2.6 Polaron Pair Recombination

Fig. 2.9 shows a qualitative illustration of the electronic and spin states involved in the polaron pair process with an energy axis that is not to scale. Uncorrelated, nongeminate charge carriers (from electrical injection) can form Coulombically bound localized states of weakly spin-spin coupled polaron pairs. PPs can either thermally dissociate back into free charge carriers or undergo transitions into strongly coupled excitons with singlet or triplet spin-manifolds. As excitons are energetically much lower than the charge carrier states, they can only annihilate through recombination by either emitting fluorescence (singlets) or phosphorescence (triplets), or, in the case of triplet excitons whose lifetimes are long enough, they can recombine through several nonradiative processes, including processes discussed above such as the triplet-triplet process, trion formation, and the triplet-exciton polaron process. Singlet excitons can also decay via intersystem crossing and subsequently produce phosphorescence by recombination into the ground state, potentially resulting in a delayed emission [36].

While the binding energies of excitons are in the hundreds of meV to low eV range,

PPs have much weaker binding energies, in the μeV to lower meV range. Excitons are so strongly bound that magnetic resonant spin-manipulation of individual electrons within these states is not possible. Instead magnetic resonance is only possible with entangled electron pairs when they are in triplet states. EDMR therefore does not produce a detectable signal for excitons that do not interact with other charge carriers.

Due to PP dissociation and recombination, PP densities can influence charge carrier (meaning uncoupled polaron) densities and thus, they can influence a material's conductivity [63], (see Eq. 2.22). Thus, manipulating PP with magnetic resonance will result in an EDMR signal.

The PP process is unambiguously identifyable by pEDMR through electrically detected Rabi spin nutations, experiments that simultaneously reveal two harmonic components with frequencies γB_1 and $2\gamma B_1$ due to the nutation of charge carriers with s = 1/2 as well as their beat oscillation. The magnetic resonance signal of the PP should consist of two Gaussian peaks with equal area resulting from the superposition of many individual Lorentzian distributions with much smaller widths whose centers are slightly shifted due to local magnetic field fluctuations caused the randomly distributed hyperfine fields (inhomogeneous broadening).

2.6 EDMR Detected Magnetic Resonance Lineshapes of Charge Carriers in Polymers

Magnetic resonance lineshapes are determined by homogeneous and inhomogeneous broadening but also by the influences of anisotropies which cause asymmetric line shapes. Homogenous line broadening is caused by a finite coherence time as well as other spin-relaxation processes of paramagnetic centers that are resonantly driven in magnetic

resonance and it results in a Lorentzian line broadening whose width depends on spin-spin relaxation times as long as no power broadening occurs [35,47,50,55]. Inhomogeneous broadening occurs due to random distributions of homogenous resonances which results in Gaussian distributions of the individual Lorentzian lines. The resulting lineshape can be described by a convolution of Gaussian distributed Lorentzian lines, a so called Voigtian function. However, in large spin ensembles, including polaron states of conducting polymers, inhomogeneous broadening is much broader than homogeneous broadening of the individual ensemble constituents due to the random hyperfine fields produced by the all abundant protons. Thus, the Vogtian lineshape essentially reduces to its most dominant contribution and becomes a Gaussian function [55].

Additional influences for magnetic resonance lineshapes include inhomogeneous broadening due to a random distribution of g-factors caused by SOC fluctuations in a given material, power broadening caused by large amplitudes of the magnetic resonant driving field, as well as motional narrowing, caused by the geometric motion of a paramagnetic center in randomly distributed local fields.

2.6.1 Motional Narrowing

Motional narrowing is a highly counterintuitive phenomenon that occurs when paramagnetic systems under magnetic resonance move fast across a condensed matter system with randomly distributed local magnetic field. At random but slow propagation, the paramagnetic systems experience at different sites different local magnetic fields. Therefore, they acquire separate phase changes at each site which leads to a broadening of the observed lineshape. However, if the spins move fast enough such that they do not have

time to pick up significant phase differences at each local site [85], the spins will essentially experience one, very homogeneous net-magnetic field representing the average of all local fields which results in an increased T_2 time and a resonance line narrowing.

2.6.2 Power Broadening

Any magnetic resonance line shape can be artificially broadened and converted into a Lorentzian line by using a sufficiently large (larger than all other intrinsic line widths contributions) amplitude B_1 of the resonant driving field [47]. This effect is called power broadening. The easiest way to explain the power broadening effect is by using Bloch spheres defined in section 2.2.1. If a paramagnetic system is off magnetic resonance then B_0 is not fully cancelled in the rotating frame which results in an off axis $B_{net} = \Delta B_0 + B_1$, see Fig. 2.2, and the magnetic moment will precess around B_{net} and thus, due to the misaligned spin-precession, a spin-resonance signal (detected inductively, electrically, or optically) will be weaker. If B_1 is large compared to ΔB_0, then the plane of precession is essentially the same as if ΔB_0 was zero. The further off resonance the magnetic field is the larger B_0 is in the rotating frame, and there is no way that the spin can change its orientation unless B_1 is so large that again the B_{eff} is nearly 90° to the z-axis. Thus, with sufficiently high power of the driving field, magnetic resonance can be established at any off-resonance magnetic field B_0.

The magnetic resonance lineshape in the power broadening domain is Lorentzian and the width of the resonance $2B_1$. Thus, the more intense the excitation field, the wider the resonance.
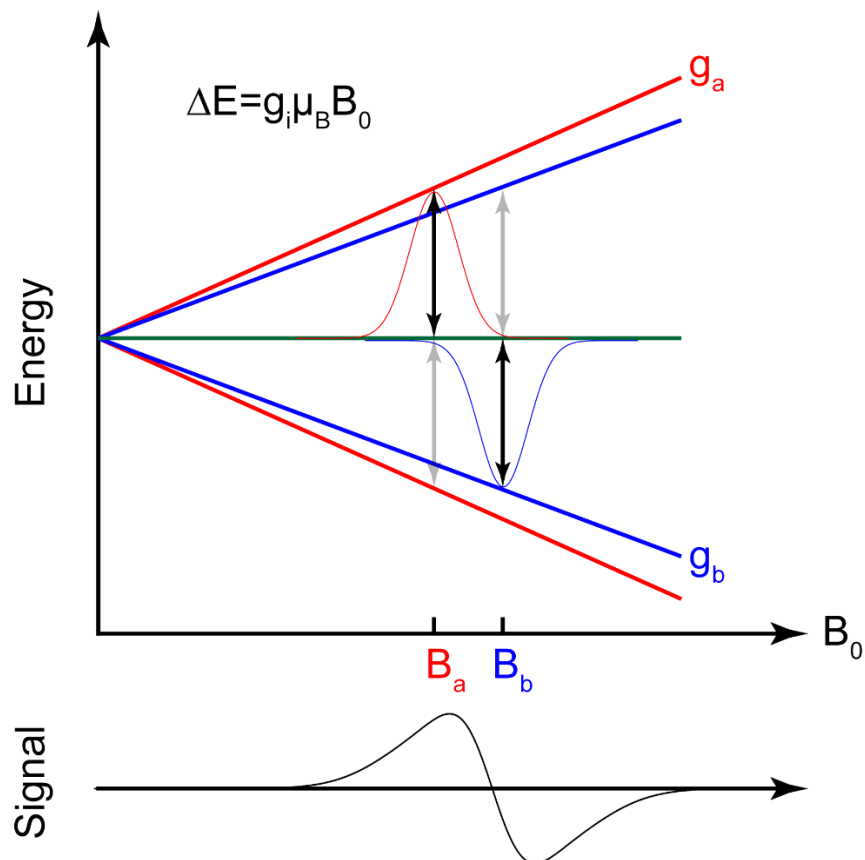
Figure 2.1: Plots of the Zeeman splitting of two paramagnetic centers with Landé g-factors g_a and g_b as functions of an applied magnetic field B_0. The energy levels of the spin up and down states are both directly proportional to the g-factors, yet with opposite signs. The energy splitting is therefore also proportional, as it is to the Bohr magneton. The $\Delta m_s = \pm 1$ transitions are shown for both spins. Two of the four absorption curves are also plotted, with centers at the maximum absorption fields (double headed arrows). The signal expected from a cw EPR measurement is cartooned below for a system with two charge carriers with different g-factors.
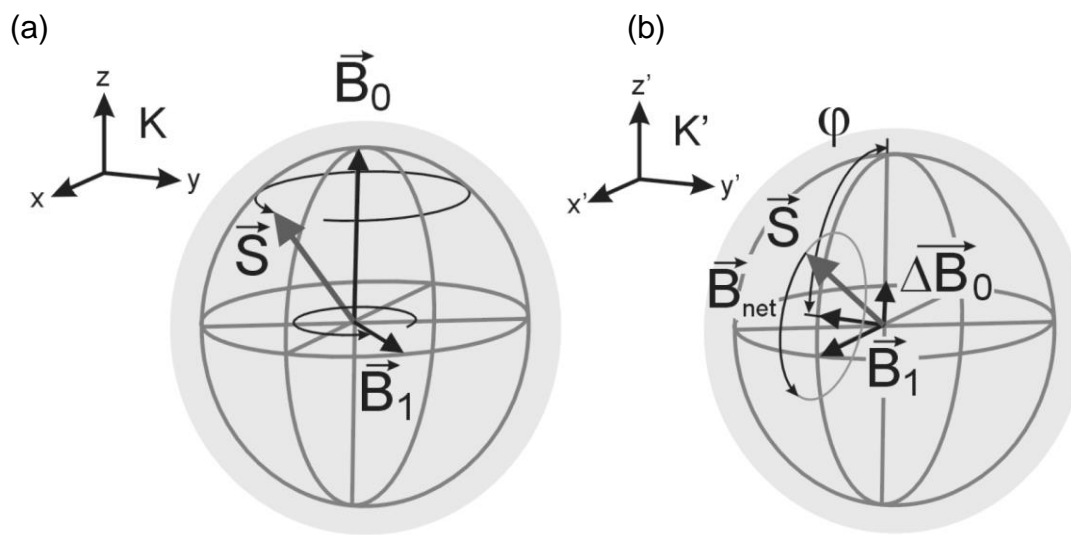
Figure 2.2: Illustration of spin motion in presence of a magnetic field B_0 and a perpendicular, rotating magnetic field component B_1 under near magnetic resonance conditions in the laboratory frame K (a) as well as the rotating frame K' (b). In the rotating frame, the static magnetic field B_0 is almost entirely "transformed away"; it is reduced to a residual small value ΔB_0. The oscillating magnetic field B_1 becomes a static magnetic field that dominates the net magnetic field B_{net} around which the spin propagates. (Adapted from reference [86]).
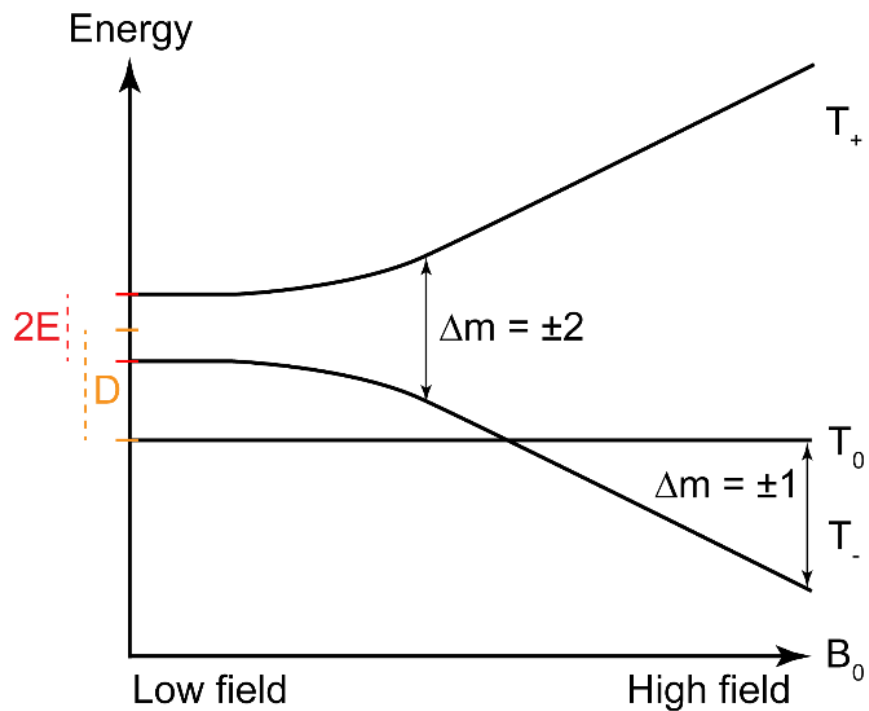
Figure 2.3: Plot of the eigenenergies of two spin-dipolar coupled electron spins as a function of the applied external magnetic field. The splitting at low fields is a result of the lifted degeneracy from the dipolar coupling within the sample. The zero field splitting parameters D and E are absolute values. Both the half field ($\Delta m = \pm 2$) as well as the full field resonance conditions ($\Delta m = \pm 1$) are shown.

Single spin-1/2
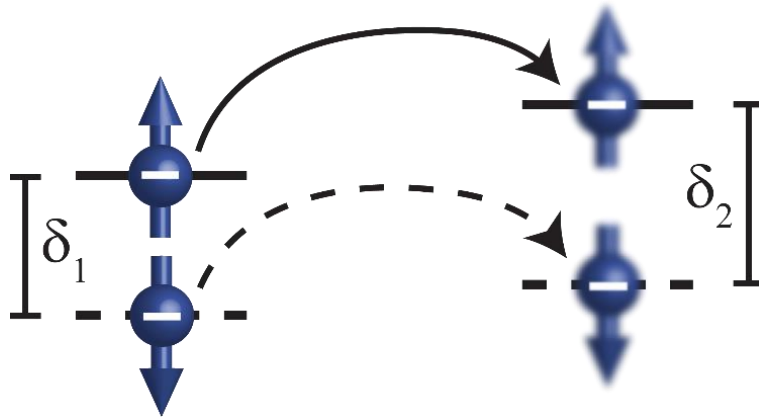
Figure 2.4: Illustration of the spin dependent single spin-½ process. The blue spheres are representative of electrons and the arrows of the spins of the charge carrier. The energy differences between an initial and final state are shown. Adapted from reference [36].
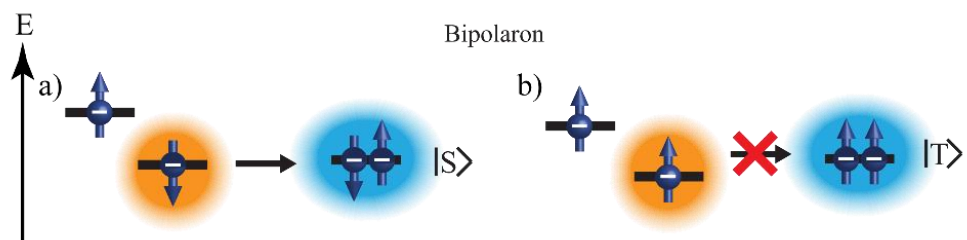
Figure 2.5: Qualitative Illustration of the spin-dependent bipolaron pair process: a) two adjacent charge carriers (no halo and orange halo) can combine to form a strongly exchange coupled singlet state, the bipolaron state which constitutes a charge transport event (blue halo). The probability of this charge transport to occur depends on the spin pair state of the two charge carriers before the transitions: (a) A Pair state with singlet is much more likely to form a bipolaron than (b) a pair in an initial triplet spin configurations. Adapted from reference [36].
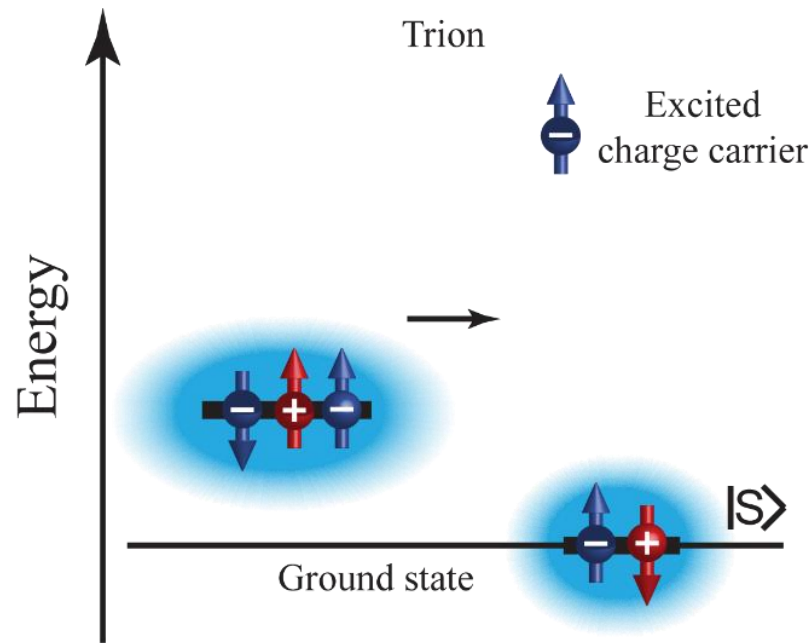
Figure 2.6: Illustration of the trion recombination process. A trion is a triplet exciton, made of electron and hole (red charge), strongly coupled (blue halo) to a polaron. The trion can recombine into a singlet ground state under generation of a free charge carrier of higher energy. Adapted from reference [36].
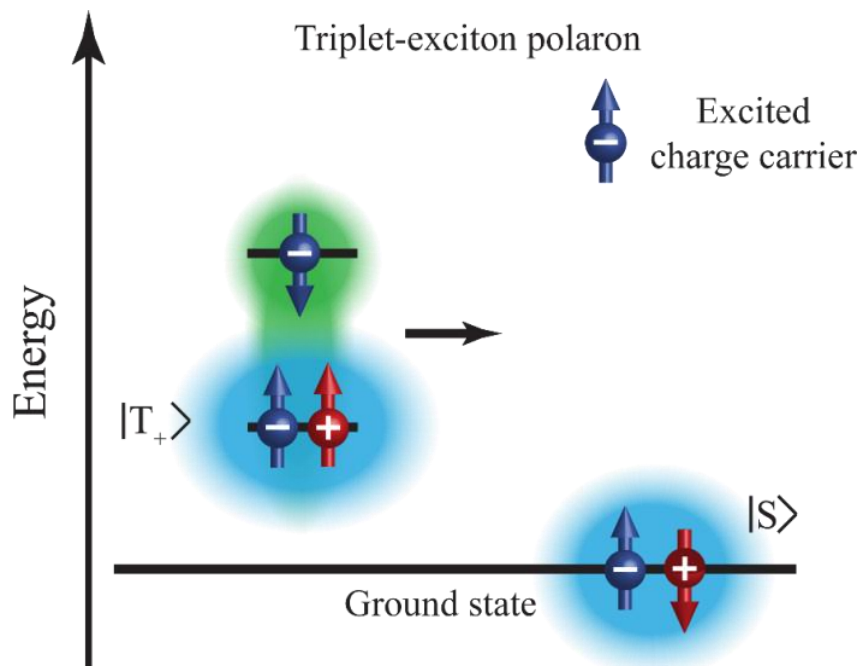
Figure 2.7 Illustration of the triplet-exciton polaron (TEP) recombination process as adapted from reference [36]. Similar to the trion recombination process, three charge carriers are involved, two with identical charge and one with opposite charge. The difference is one of the charge carriers is weakly coupled to the other two charge carrier which have mutually opposite charge and are strongly spin exchange coupled. They form a triplet exciton. The weakly interacting polaron assists in the recombination of the exciton into a singlet ground state by accepting the exciton energy and enabling spin conservation.
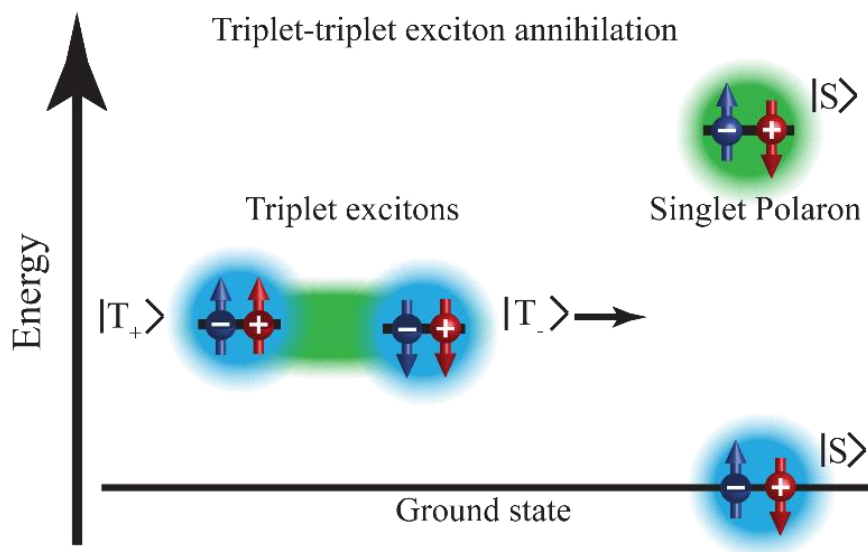
Figure 2.8: Qualitative sketch of the triplet-triplet annihilation process. Two weakly coupled triplets can dissociate into a singlet ground state and a weakly coupled singlet polaron pair. Adapted from reference [36].
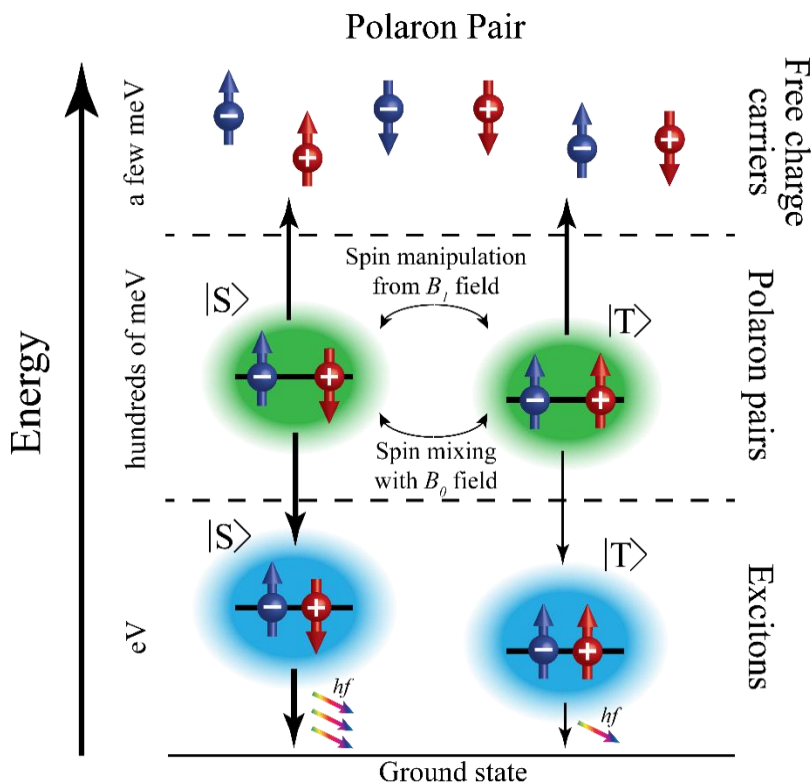
Figure 2.9 A cartoon of the polaron pair recombination process. Free charges are injected into the material at high energies and can weakly couple (green halo) to form polaron pairs in either singlet or triple configurations. The population of singlet and triplet PPs can be manipulated using a spin mixing field (B_1). The polaron pairs, with a marginal binding energy on the order of 100 meVs, can from strongly coupled (blue halos, ~1eV) excitons or dissociate back to the free charge carriers. The singlet excitons can fluoresce whereas the triplet excitons can only phosphoresce. Adapted from reference [36].

CHAPTER 3

OLEDS MADE WITH POLYFLUORENE ACTIVE LAYERS

In this chapter the polymer poly[9,9-dioctylfluorenyl-2,7-diyl] (Polyfluorene, PFO), and the concept behind OLED devices are introduced. PFO can be deposited in various different phases (i.e., morphologies) and this subsequently alters several properties of devices made of these different materials. Some of the figures or parts of the figures in this chapter haven been taken from the manuscript: *Morphology effects on spin-dependent transport and recombination in polyfuorene thin films*, which has been submitted for publication to *Phys. Rev. B* and this manuscript is coauthored by K. J. van Schooten, S. Jamali, G. Joshi, H. Malissa, J. M. Lupton, and C. Boehme.

3.1 Organic Light Emitting Diodes

Like entirely undoped semiconductor materials, most polymer materials are completely nonconducting and, therefore, they are actually insulators in their equilibrium state. Conductivity typically arises when charge carriers are injected into the material, either optically, when optical excitations dissociate into nongeminate electron-hole pairs, or electrically through appropriate injection contacts. For the study of spin-dependent recombination, the application of electron and hole injection was needed, as spin-

dependent processes in organic semiconductors are known to include spin-dependent recombination mechanisms. Thus, device structures as illustrated in Fig. 3.1 were fabricated consisting of a vertical layer stack where the studied materials were sandwiched between electron and a hole injection layers. Such asymmetric bipolar injection devices essentially constitute diodes and since at least some of recombination current in polymers layers is always radiative (namely recombination through singlet excitons as discussed above), these devices are organic light emitting diodes, referred to as OLEDs in the following. OLEDs are devices that produce light when a bias across the electrodes excites a charge from the highest molecular orbit (HOMO) level to the lowest unoccupied molecular orbit (LUMO) in the active organic layer.

The PFO-based OLED devices used in this study were fabricated in identical manners, except for changing the phase of the active PFO layer and, in a few cases, the size of the active area. An image of a processed PFO OLED device is shown in Fig 3.1 b). For these vertical stack OLEDs, all 6 layers of the device are placed atop one another and the current flows in a vertical direction.

In the device stack used in this study (shown in Fig 3.1 a)), a transparent front contact made out of indium tin oxide (ITO) layer defines the active device area. Then, a hole injection layer made out of the polymer mixture poly(3,4-ethylenedioxythiophene) polystyrene sulfonate (PEDOT:PSS) is located underneath the active polymer layer PFO, followed by a calcium (Ca) layer that is used as electron injector and an aluminum (Al) layer that covers the back of the device and operates as cathode. The photograph in Fig 3.1 b) shows the bottom of the substrate of a PFO OLED device under operation (when a forward bias is applied) which gives a front view of the device through the transparent

substrate. A small blue point (200µm) is visible due to the fluorescence emission, caused by the recombining charge carriers.

According to semiconductor device theory, p-n junctions form when a material with electrostatically positive holes as majority charge carrier (p-type material) and a material with negative electrons (n-type material) are placed next to each other. Typically, such systems are prepared by material doping which produces the different majority carrier polarization due to the different establishment of Fermi energies. At the interface, this Fermi energy difference causes local compensation and a space charge build up, a so-called depletion zone in which the device is nonconducting. Depending on the direction of an externally applied device bias, the thickness of this depletion layer can become larger or smaller and in the latter case, it will eventually disappear. It is this effect which impedes current in diodes in one bias direction while it allows current in the opposite bias direction [24]. In many commercially produced diodes, the p and n type materials are made out of the same material (they are co-deposited in the same deposition process) with changing doping profile. These devices have so-called homo-junctions. In contrast, OLEDs have different materials in adjoining layers which form p-n junctions: they form so-called heterojunctions.

Because of the numerous differences between OLEDs and most diodes based on band-semiconductors such as Si and GaAs, the structure of band diagrams and conduction mechanisms differ significantly between these two device groups. OLEDs are asymmetric devices that are made of several different materials each with different work functions that contribute to the overall device current. This, along with significantly different mobilities for electrons and holes even within the same material, results in IV curve for OLEDs which

are asymmetrical like for all other diodes yet still very different qualitatively and quantitatively. Injection conductors such as polymers do not naturally have a buildup of charges but can accommodate the charges given electrical injection into the appropriate energy levels [36]. The band structure of a PFO OLED is shown in Fig. 3.2 [6] and it illustrates how different energetic percolation pathways can occur within a variety of different bias regimes.

3.2 The Chemical Structure of Polyfluorene

Polyfluorene is an polymer made up of several monomers which have a backbone of two benzene rings and two side chains made up of 8 carbon and 17 hydrogen atoms each. There are no fluorine atoms present in PFO, in contrast to what the name of this molecule suggests. Instead, the name comes from the fact that it fluoresces. As explained in Chapter 1, the Benzene rings are made with sp^2 hybridization bonds that allows for the p_z orbitals to overlap horizontally along the backbone and allow charge transport through these molecular orbitals as long as they are continuous. If there is a discontinuity in this so-called π-conjugation, a charge must undergo a hopping transition before it can continue through the device on a new chromophore. Chromophores are sections of the polymer chain that maintain the sp^2 hybridization along the whole length of the chromophore. Their boundaries are defined by defects such as kinks in the chain that result in a gap between the otherwise overlapping p_z orbitals.

PFO differs from other OLED materials in such a way that its monomer unit, shown in Fig. 3.3 a), can be placed in a number of different configurations. PFO is a well-studied organic semiconductor [87–98], yet none of these studies have looked at spin transport

properties or spin-selection rules of the material and their dependence on the phase in which the polymer may occur. This study focuses on two of the phases that will be described in the next section.

3.3 The Influence of Order on Polyfluorene Characteristics

When PFO is processed from solution into a solid state, it is possible to influence the orientation of the molecular PFO structure in a variety of ways. The two most common orientations are the so-called glassy phase (note that this is different from the α-phase [99]), which is a purely disorganized state, comparable to the only known morphology state of many other polymers, i.e., poly[2-methoxy-5-(20-ethyl-hexyloxy)-1,4-phenylene vinylene] (MEH-PPV) [39], Super yellow-PPV [40], tris-(8-hydroxy quinolone) Al (Alq3) [67], and others. The β-phase of PFO occurs when the orientation of the polymer chains becomes an ordered structure. Due to the structural disorder in glassy phase PFO compared to β-phase PFO, the average chromophore is shorter in glassy-phase PFO compared to the β-phase PFO, while in the latter, the polymer chains are straighter and ordered in the sense that all the side chains of a chromophore are in the same plane on alternating sides between neighboring monomers. Chromophores also tend to be longer in the β phase compared to the glassy phase [100]. Cartoons illustrating these two phases for polymer chains in solid state PFO can be found in Fig 2.3 b) and c).

3.3.1 Electroluminescence of PFO Phases

The experimentally most straightforward way to determine the phase of a PFO organic layer is through its electroluminescence (EL) spectra [101]. This can be done for the OLED

structures discussed above by positioning the device so that the transparent bottom layers of glass/ITO/PEDOT-PSS are held directly in front of a spectrometer and while fluorescence is excited electrically via a forward bias. Once the voltage is large enough to excite electrons and holes into the LUMO and HOMO levels, respectively, they will naturally relax back to the ground state with an emission of a photon with an energy characteristic of the PFO phase [90].

As discussed in detail in Chapter 5, the EL spectra of glassy phase devices have a peak with a characteristic wavelength centered around 420 nm. This blue light emission is also present in the β phase but is slightly red shifted such that the 0-0 transition peak is centered near 440 nm. The 0-0 transition peak is transition from the lowest vibrational energy level of an excited state to the ground state, 0-1 transitions are when the excited state has a photon that relaxes to the 1st vibrational energy state into the ground state. The intensities of each spectral peak can be explained by the Frank-Condon principle [102].

The luminescence of PFO, like most polymers, is a red shifted mirror image of its absorption spectrum. The energy lost is due to the fast process ($\sim 10^{-12}$ s) in which charges move from higher vibrational energy levels to the bottom vibrational state due to Kasha's rule [103]. Generally, the energy lost in this process is given by $E_{stokes} = (2S - 1)\hbar\omega$ [104], where S is the Huang-Rhys parameter that depends on the physical shift of the nucleus when an electron is excited or relaxed.

3.3.2 Conductivity Differences Between PFO Phases

A distinct difference between the phases of PFO is the conductivity of the polymers which are due to the mobility differences that range on an order-of-magnitude (10^{-4} vs. 10^-

^{3} cm^2/V s) [105,106]. Both phases show larger conductivities than other typical π-conjugated polymers and they show roughly 2 orders of magnitude larger currents, compared to the prototypical polymer MEH-PPV [106]. The difference between glassy- and β-phase conductivities can be understood by their significantly different chromophore size distributions. However, tunneling and hopping events between chromophores do not solely account for the overall observed device current. Interchain crossing, where different chromophores overlap and charge is delocalized over both chains in a small segment, may actually strongly contribute to the currents observed in PFO OLEDs as well, and the intrachain transition rates are highly dependent on materials morphology, too [107,108].

3.3.3 <u>Stability Differences</u>

There is a significant difference between the stabilities of the active PFO layer made from the two studied materials phases. The β-phase shows a more stable device current when compared to glassy phase and mixed morphologies, consisting of both PFO phases [109]. Standard device currents can change up to 50% over the course of a 45-minute measurement. Neither glassy nor β-phase layers create stable polymers as they both react with oxygen readily [110,111] creating a chemical defect known as the Keto defect, which results in a green emission [112]. For experiments, these processes had to be taken into proper account and the most straightforward way to do this was to frequently refabricate PFO devices. Furthermore, for the PFO OLED devices investigated in this study, additional stability problems arose in the form of joule heating. These will be discussed in greater detail in the following Chapter 4.

a) Device stack

b) Bottom view of device
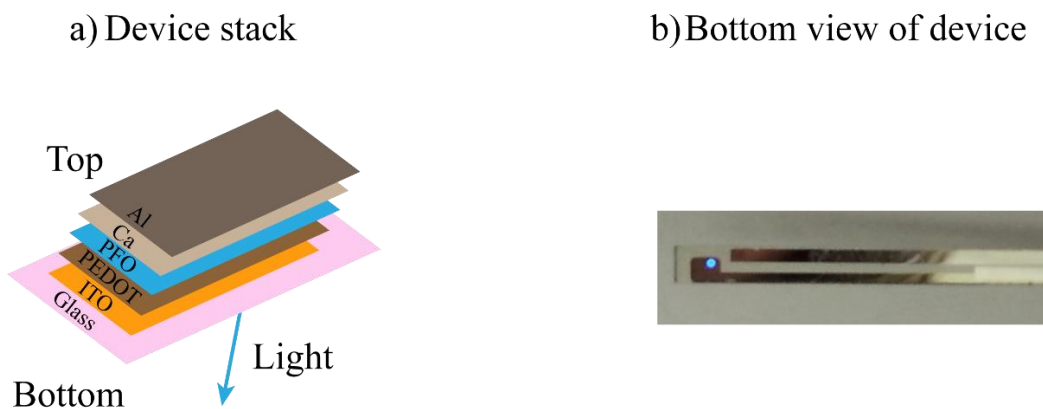
Figure 3.1 Device structure: a) Sketch of the device stack of a PFO OLED as used in this study with all the layers labeled. b) Photo of a fabricated OLED with a 200μm diameter circular active device area under operating conditions with a forward bias applied so that electrons and holes are injected into the LUMO and HOMO levels, respectively, before they recombine fluorescently under emission of blue light.
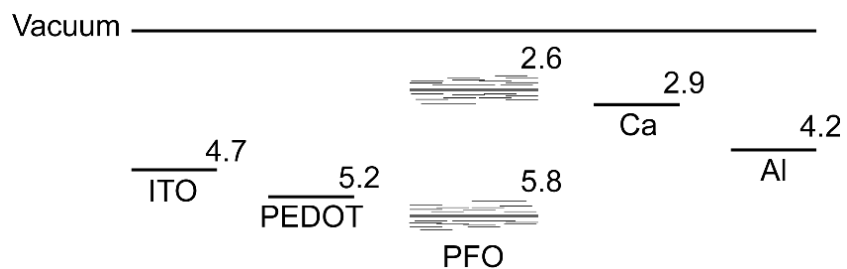
Figure 3.2 The band structure of a standard PFO OLED used in this study. Each line is an energy level, where the work functions of the different materials in a PFO OLED are stated. ITO is the transparent indium tin oxide (ITO) layer that defines the active area, PEDOT is the hole injector, calcium (Ca) the electron injector that, together with aluminum (Al), forms the device cathode. PFO has two work functions, one for the HOMO level and one for the LUMO level, respectively. All energies are given in eVs.
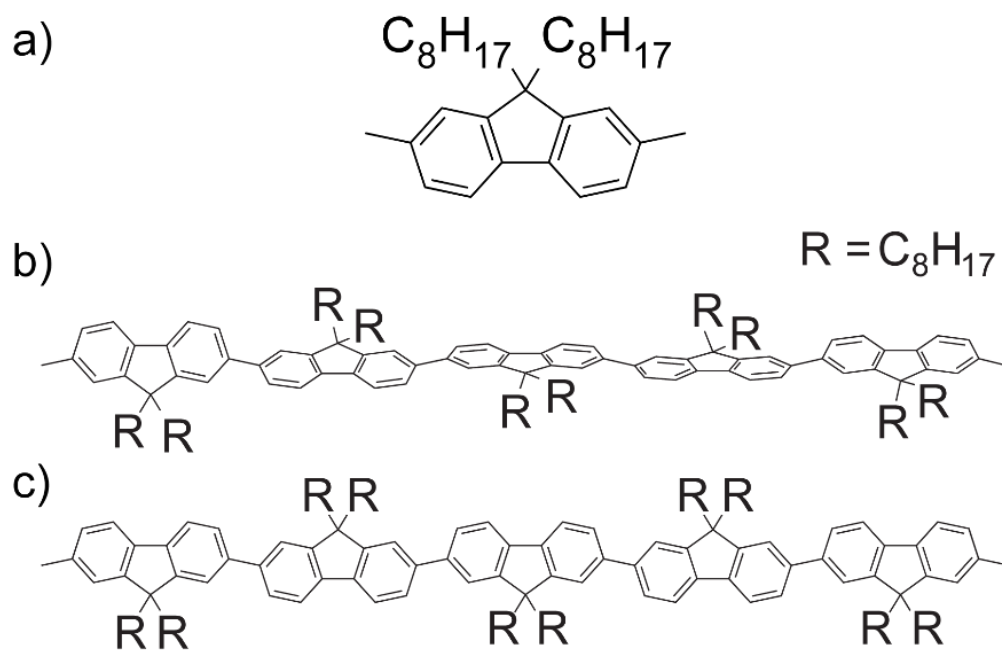
Figure 3.3 PFO chain morphology, a) Is a drawing of a monomer unit of PFO. The side chains are written instead of drawn. b) and c) are representations of glassy and β-phase polymers, respectively. Note the twisting in the glassy phase, b), and the straighter, planar, layout of the β-phase, c).

CHAPTER 4

EXPERIMENTAL EQUIPMENT AND TECHNIQUES

This chapter describes the equipment and procedures that were used to perform the experiments presented in this dissertation. This includes sample fabrication procedures. Segments of this chapter haven been taken from the manuscript: *Morphology effects on spin-dependent transport and recombination in polyfuorene thin films*, which has been submitted for publication to *Phys. Rev. B* and these segments are coauthored by K. J. van Schooten, S. Jamali, G. Joshi, H. Malissa, J. M. Lupton, and C. Boehme.

4.1 Sample Preparation

The following subsections discuss the steps required to fabricate PFO OLEDs as used in this study. While an inert glovebox system is used for the organic layer deposition, the device template fabrication takes place in the University of Utah clean room facilities using physical and chemical vapor deposition techniques as well as lithographic structuring procedures.

4.1.1 The Design of Sample Templates

For the application of kW-range microwave radiation to mm-sized electronic thin-film devices, strong inductive coupling has to be avoided in order to prevent induction of artifact currents and/or damage to the device. Low-inductive coupling can be achieved by geometric structuring of the conductive material within the test device such that the wires and vias do not couple to the applied microwave modes. The development of test device architectures meeting this low-coupling requirement has taken place in the course of the development of pEDMR spectroscopy. For the application of this to studies of organic semiconductors, which require large sample throughput rates and thus, quick sample preparation, pEDMR test device "templates" were developed for which all lithographic structuring or contacts, vias and dielectrics defining the device boundaries, are finished before the studied materials are then deposited on top of these templates in a glovebox environment. The test device templates for this study were all fabricated in large batches and then brought to the glovebox for the processing of the individual OLED layer stacks.

The OLEDs used in the experiments described in the following are all single pixel devices with circular lateral active layer areas with 500 μm and 200 μm diameter as well as rectangular active layer areas with 2 mm x 3 mm size. The vertical OLED layer stacks are prepared through spin coating of the needed organic layers and metallic evaporation for the back contact layers.

For the pEDMR experiments, the templates are held in the center position inside the resonator by a custom built sample rod made of glass epoxy. The rods make electrical connection with the template which is used to apply a bias voltage and monitor the device current. As illustrated in Fig. 4.1, the sample rod accommodates the 50 mm long glass

template with the OLED pixel in such a way that the active area at the end of the template is placed in a location within the resonator to experience the least inductive coupling to the electric microwave modes while simultaneously experiencing the homogenous and powerful magnetic fields modes. The electric field (E_1) at the sample position is minimal and thus, has a node, where the magnetic field is maximal (and where the active device area is located).

For EDMR devices, large amounts of highly conducting materials (i.e., the metal of contacts) will affect the electric and magnetic field modes within the resonator during EDMR experiments. Thus, thin films (<120 nm) of the transparent conducting indium tin oxide (ITO) and Al are used as electrical leads. The skin penetration depth $\delta = \sqrt{\frac{\rho}{\pi f \mu_r \mu_0}}$ of electromagnetic radiation in conducting materials for Al at 10 GHz is about 820 μm at room temperature (ρ is the material's resistivity, f the frequency, μ_r is the relative magnetic permeability, and μ_0 the vacuum permeability constant. This is much larger than the thickness of the contact leads. The skin depth gives the distance within a material that the current density (or electromagnetic wave amplitudes) drops to 1/e of the surface current [113]. By having metal layers thinner than the skin depth, we allow the microwave radiation to penetrate the active layer of our sample without being distorted by a voltage buildup that would occur if the metal layers were thicker.

The transparent conductor ITO, is used as cathode so that the light may pass out of the bottom of the device while still allowing electrical current to pass through the OLED. ITO (from SPI Supplies), which is sputtered on the glass template, must be smoothed after deposition to remove spikes (up to 100 nm in height) which could create pinholes in the device.

4.1.2 Cleaning the Sample Templates

Before deposition of an OLED pixel, the glass templates with the ITO must be thoroughly cleaned. The first step is to clean the templates in ultrapure water for 5 minutes, then 5 minutes in acetone and isopropyl alcohol (IPA), respectively, in an ultrasonic bath. Afterwards, the templates are dried with nitrogen gas. Finally, the dry templates are cleaned in an ozone oven for 15 minutes.

4.1.3 OLED Fabrication

The sequential steps for the fabrication of a PFO OLED of either phase are outlined below. Each step occurs directly after the preceding step.

4.1.3.1 PEDOT:PSS Application

Directly after cleaning, poly(styrene-sulfonate)-doped poly(3,4-ethylenedioxythiophene) (PEDOT:PSS) is spin-coated on the templates at 3000 rpms for 1 minute. PEDOT is a transparent water soluble semimetal that acts as a hole-injector. The PEDOT is filtered using an 0.2 µm filter before being dropcast, using a syringe to deposit small quantities, onto the active area to prevent clumping which would result in an uneven film thickness. The resulting layer of PEDOT is generally 80-100 nm in thickness [114].

4.1.3.2 Glovebox Fabrication Steps for EDMR Compatible OLED Device

In order to deposit the active polymer layer, a solution of the respective polymer must be prepared prior to deposition. The polymer PFO is highly susceptible to water and oxygen. In order to maintain a pure and unaltered polymer layer, the PFO must be added

to the device in an inert atmosphere. While the dry polymer is more robust in the presence of atmospheric conditions, the solution used to spin coat the organic layer degrades when exposed to atmospheric O_2 very quickly [110–112,115]. This is why the polymer solutions used for spincoating are also prepared and stored within the GB.

The so-called Keto-defect occurs during device fabrication or via an electro-oxidation degradation process [110,115]. The Keto-defect is seen to be stronger in electroluminescence (EL) rather than photoluminescence (PL) spectra which makes it detrimental to device performance. Essentially Keto defects act in a way that the oxidation produces a lower energy state (with a band gap ~2.2 eV) which singlet excitons get trapped in and fluoresce and refill faster than the normal singlet state is able to fluoresce. This produces a much more intense broad green emission in polyfluorene-like devices.

To prevent the samples from being exposed to air during the device preparation, they are placed in a N_2 rich glove-box (GB) immediately after the PEDOT deposition. Once in the GB the samples are baked on a hot plate for 10 minutes at 100°C to evaporate all remaining traces of water in the PEDOT.

Toluene is applied in order to clean the active device area from dirt particles that may have settled on the PEDOT after the baking process. PEDOT is not soluble by toluene or chloroform (the two main solvents used in the polymer solutions). To dry the toluene from the device it is placed on the spincoater and run for a little more than 10 seconds.

4.1.3.3 Fabrication Steps of the β- and the glassy-phases

The degree of order within the PFO active layer can be controlled through layer deposition parameters and subsequent film treatment. A glassy-phase layer is formed by

spin-coating a 5 g/L solution of the polymer in toluene directly onto the template for 1 minute with no further postprocessing of the layer. PFO in the ordered β-phase is formed by briefly immersing a spin-coated layer of a slightly more concentrated solution (7 g/L in toluene) into a 1:1 orthogonal solvent mixture of tetrahydrofuran and methanol for 2 minutes, followed by thermal annealing at 100°C for 5 minutes, as outlined in Ref. [109].

Using pipets, 6μL of the polymer solution are deposited on the active area of the template. Then they are spun for 30 seconds at 1500 rpms, for the β phase, 1 minute for the glassy phase. The β samples are placed on a hotplate (100 C) after the spincoating for 2 minutes to evaporate any remaining solvent. Glassy samples are never exposed to heat as some reports have been issued stating that thermal annealing can lead to a greater β phase component.

4.1.3.4 Evaporation of Thin Metal Contacts

Once the organic layer is on the templates they are placed in the evaporation chamber within the GB. A shadow mask is used to hold the templates to ensure that the metal layers are evaporated only in the desired locations. Two separate boats and crucibles are used to warm the Al and Ca to their respective evaporation points. The pressure within a bell jar where the deposition takes place is brought down to 5×10^{-6} mbar before any power is dispersed to the evaporation sources. No deposition will take place if the pressure is over 1×10^{-5} mbar, which occasionally can happen when the first metal layer is warmed up and brought to thermal equilibrium.

The bell jar has three evaporation shutters that ensure that no metal reaches the samples before it is wanted: two shutters for each evaporation source, and one for the

shadow mask. Ensuring an even and smooth deposition of metal is a simple process: the boa or crucible acts as a heater when current is applied to it and warms the metal inside. First, the metal temperature is kept right below the evaporation point for a few minutes to ensure all of the material is in a uniform state. Then, the power to the source is increased to bring it the metal over the evaporation threshold and the source shutter is opened while the shadow mask shutter remains closed. A crystal is used to measure the rate of metallic evaporation by monitoring its resonance frequency as more metal is deposited onto it. When the desired rate is achieved, the shutter blocking the shadow mask is opened and the deposition can take place.

The first layer atop the organic semiconductor is Ca, as this metal has the needed work function for electron injection. The Ca layer is usually 5-7nm thick. Then a second metal layer made from Al is deposited which is usually 100nm to 150nm thick. The Al layer is used as thin-film wire connecting the back contact of the OLED device with the contact pads on the device template. The Al layer also serves as an encapsulation layer if thick enough (albeit additional encapsulation is needed when the device is exposed to air). For working OLED devices, the Al layer can be as thin as 15 nm in order to make the top contact partially transparent. However, for the study presented here, such entirely transparent devices were not used.

4.1.3.5 Encapsulation of the OLED

After evaporation of the top electrodes, the samples are characterized electrically within the GB. Devices with good IV characteristics are then encapsulated so that they may be removed from the GB and exposed to atmospheric conditions.

A two-part epoxy glue is used to cover the active area as well as all the evaporated metal layers to ensure that no air or moisture can reach the active device layers. While this encapsulation scheme is straightforward to implement and very reliable at room temperature, it cannot be cooled down to liquid He or even liquid N_2 temperatures without breaking apart and destroying the sample. The epoxy layer tends to be on the order of one mm thick or more. This macroscopic thickness can become problematic when the EDMR devices are used with microscopic near-field resonators such as coplanar waveguide resonators that will be discussed later. For such experiments, another encapsulation method can be used that is based on a spin-on-glass (commercially available under the name Futurrex IC1-200 or 500). This material is applied by simply depositing and spinning it on top of the sample in the same manner as when the organic layer is fabricated. While spin-on glass as an encapsulation layer is not as reliable as epoxy in blocking the atmosphere from reaching the device, it can be cooled down to 4 K and is thin enough to be utilized in near-field resonators.

4.1.4 Joule-heating in PFO OLEDs

Since PFO is a relatively high mobility polymer, with mobilities ranging from 2×10^{-5} to 3×10^{-4} cm²/Vs at 293 K, depending on the morphological phase of the polymer [105], device performance can be negatively impacted by Joule heating for large active area devices with 6 mm^2 active area at high current densities of (50-70 mA/cm^2), causing a rapid degradation (of up to 75%) of the steady-state current (4 mA) for a fixed bias voltage.

Thin film devices used throughout this study are made under nominally identical conditions during every fabrication step. Large-area devices are made on 3×2 mm active

area templates and, for PFO OLEDS, resulting in currents up to 4 mA at voltages of approximately 3.5 V. Under these conditions, substantial electrical device degradation is recognizable within 1-2 hours of constant bias application. Furthermore, at constant bias, the device current was highly unstable and fluctuated up to 10% randomly in addition to the systematic current decrease.

In order to limit Joule heating, maintain device integrity, and increase layer homogeneity, a lithographically-structured SiN layer is used to define small circular openings to the underlying ITO with diameters of either 500 or 200 μm. This design reduces Joule heating by improved heat-sinking and therefore allows high-power device operation. This also allows device operation at higher voltages while maintaining currents of approximately 20 μA (~2 orders of magnitude less than for the large area devices).

EDMR detected charge carrier spin-Rabi oscillations, observed on a large area (3×2 mm) PFO OLED is depicted in Fig. 4.2. The data set displayed in panel (a) shows the device current plotted with an arbitrary color scale as a function of time after the magnetic resonant excitation pulse and as a function of the length of the applied magnetic resonant pulse. The total duration of all measurements, including the shot repetitions for signal averaging which provided the data displayed, is about half an hour. As shown in Fig. 4.2, the observed signal drastically changes, when measurements are made for pulse lengths in excess of about 105ns. The cause of this drastic change is shown by the current-voltage (IV) functions of the device that are plotted in panel (b): The IV data shown in the bottom plot were recorded before the EDMR data shown in panel (a) were recorded while the IV data shown in the top plot were recorded thereafter. Apparently, the diode device turned into an ohmic resistor while the EDMR experiment was conducted. This abrupt degradation

behavior was highly reproducible for full sized devices, while it was entirely absent for nominally identically prepared OLED device with small active area.

Using small area OLED devices with increased heat sinking, reduced device current, and reduced Joule heating, EDMR OLED device of both PFO phases remain stable for more than 2 days under constant voltage bias. Also, the variation in current over several hours is less than 10 µA, typically about 2 µA or 10% for devices with glassy PFO as active layer while device with β-phase PFO are generally found to change by <7% from the steady state current. The devices degrade to a point where charge carriers can no longer be injected (no electroluminescence, nondiode current-voltage characteristic) within at most 27 hours of continuous device operation.

All measurements presented in the following are performed on PFO OLED devices with 200 µm diameter active areas under forward bias conditions establishing a 20 µA forward current. Exceptions are made for the experiments in Chapters 8 and 9, where larger diameter devices are used with a steady-state current of 50 µA in order to increase the signal under otherwise similar operating conditions. The change in current due to the magnetic resonant excitation is measured by subtraction of the steady-state current from the measured device current. A high-pass filter with a cut-off frequency of 30 Hz was set with the used Stanford Research SR570 current amplifier in order to filter out low frequency contributions.

In Chapter 5 a picture of a scanning electron micrograph of the unprocessed active area and a photograph of light emission from the structured OLED are shown respectively. For all devices, the current-voltage characteristic was measured to ensure proper diode operation.

4.2 Experimental Facilities for pEDMR Spectroscopy

Once the samples are fabricated and characterized they are inserted into the aforementioned custom made sample rods. A low-Q, dielectric, cylindrical Flex-Line resonator (approximately 7 cm tall with a radius of 3 cm) (Bruker ER 4118X-MD5 X-band resonator) is used for microwave excitation. The resonator is placed in a Helium-4 flow cryostat that is used to control the temperature as well as provide an inert atmosphere in which the experiments are run. The cryostat is placed in the middle of the static magnetic field that is produced by a Helmholtz coil electromagnet.

The sample is biased using a variable battery voltage source (Stanford Research Systems SRS SIM928). The device current is monitored by an analog digital converter (ADC) and digitizer after passing through a current preamplifier. The low-noise current preamplifier (SRS570) measures the current and converts it to a voltage that the ADC, and subsequently, the computer can record. The SRS570 amplifier is equipped with an array of integrated signal filters and a DC offset option.

A Bruker Elexsys E580 pulsed EPR spectrometer is used to read the signal from the SRS570, and control the static magnetic field B_0 as well as the timing of the microwave excitation sequences. The E580 has a pulse programmer that controls the microwave bridge, determining how long and strong the excitation pulses for each experiment must be with nanosecond precision. A traveling-wave-tube (TWT) amplifier is used to coherently amplify the power of the excitation pulse from the mW range into the kW range, which in the dielectric cavity produces radiation field amplitudes, B_1, in the mT range. The cryostat temperature is monitored by a Cernox sensor and the temperature is controlled using a heating wire.

4.3 Experimental Facilities for cw EDMR Spectroscopy

In order to execute cw EDMR in a broad range of microwave frequencies, coplanar waveguide resonators were developed to allow for coupling at higher resonator harmonics [53]. These quarter-wave coplanar wave guide resonators were made on a microwave circuit board (AD1000, Arlon Microwave Materials) with a dielectric constant of ε_r = 10. The circuit boards are made to be geometrically compatible with the cryostat mentioned prior, giving them low temperature capabilities; their dimensions are 1.27 × 3.81 cm^2. The center conductor of the resonator has a width of 152 μm and the spaces on both sides are 76 μm for all resonators. The main difference between the resonators with different fundamental frequencies is the length of the coupling capacity, which is the segment of the resonator strip that has a length of a quarter wavelength and which determines the inductive resonance frequency of the resonator. The resonators all have a ~50 Ω impedance. More details can be seen in Ref [53], and the probe head layout is shown in Fig. 4.3. An end-launch connector (Southwest Microwave Inc.) connects the microwave source via SMA cables to the circuit board.

Fig. 4.3 shows the geometry of the CPWG setup. These resonators can be used not just with their fundamental frequencies f_0 but also with higher harmonics at frequencies f_n = (2n + 1) f_0 [53].

Homemade Helmholtz coils are attached to the circuit board such that they produce a modulating magnetic field to B_0 in the center of the resonator positions. The electrical connection of the Helmholtz cables and the device is established by spring-loaded contact pins and run up the sample rod to separate coaxial jacks. A G3 spacer is used to pressure the top of the sample on the waveguide and ensure that the sample remains in place as well

as contacting the contact pins to provide contact at all temperatures.

4.4 Signal Conversion and Noise Considerations

For the current detection chain described above, the raw device current

$$I = \frac{RawData*(Amp_{Sensitivity})*(ADC)}{(N_{shots})*(N_{scans})} \tag{4.1}$$

can be calculated from the recorded counts of the digitizer in the Bruker Elexsys E580 Spectrometer. The E580 is equipped with an 8-bit ADC to digitize the analogue signal, for which it counts 220 steps/volt and acts at the same time as a voltage divider that produces a factor of ½ so that $ADC = 2/220$ in the Eq. 4.1. N_{shots} is the number of shot repetitions while N_{scans} the number of scan repetitions in a given experiment.

As explained in section 2.4, pEDMR experiments are based on charge measurements instead of current measurements, which are based on the integration of transient current measurements. In order to accurately obtain these charges, the equation above is simply multiplied by the time resolution, t_{res}, of the spectrometer. Typically t_{res}= 4 ns, but can be increased by steps of 2 ns to any larger time.

The signal to noise ratio (SNR) for the measurement setup described above is given by the signal over the variance and scales as the square root of the number of averages $(S/\sigma^2 \propto \sqrt{N})$. This relationship shows how averaging repetitively measured experiments leads to data with increases SNR, but it also shows that the square-root dependent increase is highly sublinear and thus, it requires many experimental resources when large SNR increases are needed.

Main contributors to noise in EDMR experiments are electrical shot noise and Johnson-Nyquist (thermal) noise. Shot noise is the result of individual charges which have

discrete detection times. While a constant current is described by a steady flow of charges that a detector collects upon arrival, each individual charge causes a small random current fluctuation on a small time scale. Shot noise power is constantly distributed throughout the frequency domain the integral leads to a shot noise magnitude of $\Delta I_{sn} = \sqrt{2eI\Delta f}$ here e is the electron charge, I is the DC current and Δf is the bandwidth. Following this expression, it becomes obvious that the SNR of a current signal I caused by shot noise is proportional to $1/\sqrt{I}$ [116].

Johnson-Nyquist noise, commonly called "thermal noise," is present in anytime charge carriers move through a conductor at a finite temperature [117–120]. Thermal noise is caused by random motion of charges inside a conductor and as such, it caused fluctuating electrostatic potentials, leading to a noise current $\Delta I_{JN} = \sqrt{(4k_B T\Delta f)/R}$ in a conductor with T being the temperature and R the resistance.

Flicker noise, also called 1/f noise and burst noise, is not considered to be of significance for the measurements discussed in this dissertation as flicker noise is considered to be smaller than shot noise in EDMR studies [116], and burst noise is filtered out by low-frequency high pass filter as it generally is in the very low audio range (<100 Hz). Flicker noise can occur when the resistance of a device has minute fluctuations at a frequency (f) resulting in small voltage or current fluctuations. Aside from shot and thermal noise, EDMR measurements are also influenced by current contributions from inductively coupled background EM waves. However, as these contributions are not noise because they are not random, but artifact signals, they can be oppressed by simple subtraction from of the data.

4.5 Multifrequency cw EDMR Spectrocopy

In the following chapters, cw EDMR spectroscopy is used in order to distinguish the contributions of random local hyperfine fields caused by proton spins to the inhomogeneous broadening of polaron pair EDMR lines from contributions of the g-factor inhomogeneity to inhomogeneous broadening. As discussed in section 2.6, inhomoeneous broadening always causes Gaussian line shapes and thus, a simple fit

$$\partial I = \frac{A}{\sigma_1} e^{\frac{-(x-B_0)^2}{2\sigma_1^2}} + \frac{A}{R\sigma_2} e^{\frac{-(x-B_0)^2}{2\sigma_2^2}} \qquad (4.2)$$

of the two Gaussian resonance lines within an EDMR signal of a PP system, where the Gaussian line broadening is defined by the standard deviation

$$\sigma_{1,2} = \sqrt{B_{Hyp_{1,2}}^2 + (\alpha_{1,2}B_0)^2}, \qquad (4.3)$$

cannot reveal what the individual contributions of the hyperfine fields and the SOC induced g-factor distribution are, i.e., Eq. 4.3 is only one equation that cannot reveal two unknown parameters. This problem can be resolved by recording EDMR spectra different magnetic fields and microwave frequencies, yielding different values for σ_1 and σ_2 for each applied value of B_0 and thus, additional equations to Eq. 4.2 each of which have the same unknown variables α_1, α_2, and B_{HYP}.

Experimentally, EDMR spectra of the PP signal are recorded for magnetic field intervals around several difference resonant magnetic fields $B_0 = f/\gamma$ corresponding to several different applied microwave frequencies f with $\gamma = 28.034953$ GHz/T being the gyromagnetic ratio [53].

Using the aforementioned coplanar waveguide resonators allows the collection of EDMR spectra for more than 27 different frequencies between 1GHz and 20 GHz.

Furthermore, using a copper coil, it is possible to measure EDMR resonances in the 100 MHz to 1GHz range and furthermore, by utilization of magnetic field user facilities such as National High Magnetic Field Laboratory in Tallahassee, Florida EDMR spectroscopy, it is possible up to garner spectra at frequencies up to 330 GHz. Using all these experimental capabilities to conduct magnetic resonance spectroscopy at frequencies spanning more than four orders of magnitude, it is possible to extract accurate values for the SOC induced g-factor distribution terms α_1 and α_2 as well as the magnitude of hyperfine fields by fitting the entire set of EDMR spectra recorded at various frequencies with a global fit function [3,53].

4.5.1 Bootstrap Analysis for the Numerical Determination of Fit Variable Confidence Intervals

The bootstrap method is a numerical procedure which [121] allows us to calculate the probability distributions of fit parameters belonging to fits of experimental data. A condition for the applicability of the bootstrap technique is that the residual value resulting from a fit procedure are independent random variable and that they are therefore randomly distributed. The idea behind the bootstrap technique is to use residuals randomly picked from a least-square fit in order to generate value sets, which are then fitted using the same least-squares algorithm as used on the actual experimental data. When n value sets are generated and a fit is executed for each value set, then n sets of fit parameters are produced. From the resulting distribution of each these parameters, the confidence intervals of each fit parameter can be estimated.

The following list summarizes the individual steps for the bootstrap algorithm:

i.   A least squares fit is performed on the experimental dataset

ii. The residuals are calculated

iii. A value set is generated by adding randomly picked (with replacement) residuals from step 2 to the fit curve from step 1.

iv. A least squares fit (using the algorithm from step 1) is performed on the artificial dataset from step 3.

v. Steps 3 and 4 are repeated n times. This will result in n sets of fit parameters (from step 4).

vi. The n sets of fit parameters will be statistically distributed. These distributions for each parameter reflects the ambiguity that originates from the experimental data itself and they allow to estimate expectation values and standard deviations for the model parameters of the fit (which means the fit parameters).

If the model used for the fit procedure accurately describes the measured data and n is sufficiently large, the algorithm will give distributions of the fit parameters from which the standard deviation and confidence interval can be obtained. Fig. 4.4 shows the histogram results for 1000 iterations of a bootstrap analysis carried out to determine both spin relaxation times for electrically detected spin-inversion recovery experiments performed on glassy and β-phase T_1 and discussed in Chapter 8. The larger noise seen in the β-phase data clearly coincides with a larger spread of possible fit results indicated in Fig. 4.4. This is an example that illustrates the inherent capability of the bootstrap routine to obtain the correct probability distribution for a fit parameter, even if the fit model is highly nonlinear which causes more than one local maximum for the fit parameters probability distributions.

4.6 Experimental Procedures

This section covers the individual steps of the experimental procedures applied to this study. These measurements include the characterization of the fabricated PFO OLED devices as well as the pulsed and cw EDMR spectroscopy experiments.

4.6.1 <u>PFO OLED Characterization</u>

Before EDMR experiments can be conducted that reveal the differences of spin-dependent charge carrier transitions between the two phases in PFO, it is paramount that the properties of the devices subjected to these experiments are verified, i.e., the used experimental devices require careful characterization for each fabricated device. There are two main characterization techniques that all devices were subjected to before they were subjected to EDMR experiments, namely electroluminescence spectroscopy and current-voltage characterization. If either one of the two measurements show incongruities for a given device, the device will be deemed "poor" and not used for further experiments.

4.6.1.1 Current-Voltage Curves

For the measurement of the device current as a function of the applied bias (IV characterization), the device is connected to a Keithley 2400 voltage source meter and the current is monitored as the voltage is swept from a low negative bias or 0 V to about 500 mV above the "turn on voltage" (which is generally around 3 V) of the device where the current starts to increase exponentially with applied voltage. The Keithley Instrument is used as both the voltage source and current monitor that is externally controlled by the LabTracer 2.9 software.

IV characterization is an essential integrity test for an OLED device. A shorted device, as represented by the plot in Fig. 4.5 a), gives a linear IV curve as all the charge carriers bypass the organic device layer. Fig. 4.5 c) shows an ideal IV curve that is near zero for voltages below a turn on voltage beyond which the charge carriers are injected into the device. Some IV measurements also reveal a mixed behavior where a nonlinear domain

exists indicating the presence of charge carrier in injection, while in the low bias regime a linear characteristic is seen. This is highly indicative of a "shunt" within the device, a small ohmic short that is parallel to the organic layer (Fig 4.5 b). This type of device produces generally only very weak EDMR signals.

4.6.1.2 Electroluminescence Spectra

The second characterization technique is electroluminescence (EL) spectroscopy. This experiment is a critical characterization tool as the EL spectra are key indicators for the materials morphology within the active PFO layer in the OLED (see section 3.3.1). The measurement of the EL spectrum is technologically straightforward: Once the device is fabricated, a bias is above the LUMO level (~3 V for PFO) is applied and the emitted light can be collected by either an Andor SR-303i spectrometer that is equipped with an intensified charge-coupled device (Adnor iStar DH720 ICCD) or an Avantes Sensline AvaSpec-2048 XL spectrometer.

For these experiments, the OLED emission is detected through the transparent device bottom while other light sources (room lights, etc.) are blacked out in order to optimize the SNR and avoid surplus artifact signals.

4.6.2 Pulsed Magnetic Resonance Experiments

Figure 4.6 illustrates six magnetic resonant pulse sequences that are used for the pEDMR experiments discussed in the following, along with the Bloch-sphere illustrations of the charge carrier spin ensemble propagation that is caused by these pulse sequences and depictions of the spin-dependent transition rates expected from the spin motion.

4.6.2.1 Current Transients After Pulsed Excitation as a Function of Magnetic Field

The first EDMR experiment that is usually conducted on a material that has previously not been studied by EDMR and thus, that is unknown to exhibit spin-dependent current, is to measure current changes after a brief intensive microwave excitation pulse as a function of time and the applied magnetic field. This two-dimensional measurement, depicted in Fig. 4.6a) is referred to in the following as "field map" measurements as it maps for the applied microwave frequency, a broad range of dynamic and magnetic field domains where potential EDMR signals can occur.

Typically, for each applied value of B_0, a forward bias is applied to the OLED and a 400ns long burst of B_1 is applied to the device (green rectangle). If on-magnetic resonance, this excitation changes the spin ensemble from its steady state and scrambles it randomly given a long enough pulse length (shown in the Bloch spheres). When the current change is monitored in the device, both current quenching and current enhancement are observable after the excitation. The transient of the measured current change is typically measured for the duration of the shot repetition time (SRT) which must be chosen such that the resonantly changed device current can return to its steady state value. After that another microwave burst (another shot) is applied and the experiment is repeated. Once a transient has been repeated and recorded often enough for a given value B_0 such that an average transient with sufficiently high SNR has been obtained, the magnetic field is shifted to a new value of B_0 and the entire procedure is repeated. Once an entire scan is finished (average transients for all values of B_0 have been obtained), the scan is repeated and averaged with previous scans in order to account for low-frequency noise and slow drift effects.

The one-pulse field map experiments described here usually allow the acquisition of EDMR spectra and a first glimpse into the dynamics of the observed spin-dependent processes. However, the interpretation of one-pulse field map experiments requires great care in that they do not provide optimal SNR compared to lock-in detected cw EDMR experiments, and because of the excitation by short powerful pulses, their spectra are prone to suffer from power broadening effects [27].

Field map experiments are also possible at half-field resonance caused by excitonic states for which the microwave pulse drives transitions between T_- and T_+ at the magnetic field strength corresponding to $g = 4$ [50,55] and revealing asymmetric resonance line shapes which allow to determine both, the zero field splitting parameter D for the polymer [21,122].

4.6.2.2 Rabi Oscillation Measurements

Electrically detected single pulse-Rabi oscillation (also called transient nutation) experiments are crucial for the determination of the fundamental qualitative physical nature of a spin-dependent process that causes an EDMR signal. For this experiment, the B_0 field is held constant on resonance with a known EDMR signal. Then, a single pulse is applied and the resulting spin-dependent current change transient is integrated into a charge Q. This charge Q is then measured repeatedly after excitation with increasing pulse length τ, such that the pulse lengths dependence function $Q(\tau)$ is obtained. This is illustrated in Fig. 4.7 b). The function $Q(\tau)$ reveals the coherent propagation of the excited spin-ensemble during the excitation pulse, which allows us to obtain information about the spin-Hamiltonian based on which the coherent spin propagation takes place and thus, it reveals information

about the fundamental nature of the probed spin-dependent process (i.e., which of the mechanisms discussed in section 2.5.2 controls the spin-dependent current). For instance, under strong magnetic resonant MW drive, both charge carriers in a PP will be rotated simultaneously and a spin-dependent signal will show a beating frequency component at twice that of the Rabi frequency (γB_1). Thus, the observation of spin-beating is strong evidence for the presence of a PP process.

Electrically detected Rabi nutations have been used to determine hyperfine fields [59], exchange [123], and dipolar couplings [27]. Finally single-pulse spin-Rabi oscillation experiments are crucial for the determination of the lengths of π and $\pi/2$ pulses that are needed for the execution of spin-echo experiments. A π pulse is a pulse that is long and strong enough to flip the spins 180° from their initial position. A $\pi/2$ pulse simply rotates the spins 90°. These times are determined by looking at the time between local maxima and minima in the Rabi oscillations, which provide unambiguous information about the pulse powers and pulse lengths needed for any desired excitation angle.

4.6.2.3 Hahn Echo Sequence

Hahn spin-Echo experiments were among the first coherent spin experiments and also among the first pulsed magnetic resonance experiment in the early 1950s [71]. For the application of this iconic pulse sequence in pEDMR three pulses rather than two pulses are needed [124]. Analogously to NMR and EPR detected Hahn echoes, they are used in pEDMR spectroscopy in order to determine the transverse spin relaxation time T_2.

From the microwave pulse scheme and the Bloch sphere representation in Fig. 4.6 c), it can be seen that a spin ensemble that is polarized along the direction of B_0 can rotated

into the x-y plane by a π/2 pulse. The π/2 pulse strength and length are determined by the Rabi measurements described above. As the spins within the spin ensemble experience different local magnetic fields, they will gradually dephase in the x-y plane for a time τ. Then, a π pulse is applied which flips the spins by 180° and the same local fields that lead to the dephasing have the opposite effect and refocus then spins except for those that have lost coherence via hopping or moving to a different local [124]. Another time τ is waited to allow the spins to reorient the same amount as they were allowed to separate. In EDMR the additional π/2 pulse then places the spins back along the z-axis which projects the spin-polarization onto a permutation symmetry state that is detectable with spin-dependent charge carrier transition rates.

In order to resolve the actual spin-echo, which is the brief rephasing spike that occurs at a time around 2τ after the first π/2 pulse, the detection pulse must be swept through the echo transient and the entire three-pulse sequence must be repeated for different trigger timings τ' of the projection pulse.

4.6.2.4 Hahn Echo Decay Sequence

Both, the longitudinal spin-relaxation time T_1 as well as the transverse spin-relaxation time T_2 can be measured using the Hahn-echo sequence. For both, a Rabi nutation experiment must determine how long a microwave pulse must be to attain a maximum inversion of the spin orientation within the active area of the OLED. The Rabi measurement but also the dephasing time of a Hahn-echo are able to provide the coherent dephasing time T_2^*, which is a lower limit on T_2. In order to accurately measure T_2, the magnitude of the Hahn echo as a function of the coherence decay time τ is measured. In order to do this

without repeated Hahn echo measurements as it is done for pEPR spectroscopy (which would require lengthy sweep experiments of τ), the peak echo intensity is simply measured as a function of 2τ. T_2 is determined by fitting the obtained function with an exponential decay with time constant T_2.

4.6.2.5 Spin-lattice Relaxation Time Measurement with EDMR

To determine the longitudinal coherence time (T_1) an inversion recovery experiment is conducted, consisting of a in initial π pulse which inverts the steady state spin ensemble polarization, then a wait time T, before a Hahn echo sequence (described above) is used as a readout scheme for the remaining polarization at the end of the waiting time.

The pulse sequence is shown in Fig. 4.6 e). The spins oriented along B_0 are initially rotated around the x-axis by a π pulse, then over the waiting time T, some randomly flip back to the original polarization state. As T increases the polarization returns to the equilibrium state with an exponential time constant, T_1, that is the spin-flip time or spin-lattice relaxation time [68].

4.6.2.6 EDMR Detected Electron Spin Echo Envelope Modulation

Electron spin echo envelope modulation (ESEEM) is a measurement that allows for the detection and determination of hyperfine coupling between nuclei and probed electron spins. It is based on a stimulated echo (three-pulse) echo sequence where the first two $\pi/2$ pulses generate nuclear polarization that is eventually read out by the final two pulses after the spins interact with the local magnetic fields from the nuclei in their vicinity that have a particular Larmor frequency that is overlaid onto the decay of the signal. As the pulse

sequence is similar to the Hahn-echo decay experiment, ESEEM functions have a strong echo decay component which can be subtracted by a fit function consisting of a simple exponential decay. Taking the Fourier transform of the measured ESEEM function after this subtraction reveals the modulation frequencies that the observed charge carrier spins experience. These typically reflect the Larmor precession of adjacent nuclear spin.

Fig. 4.6 f) shows the pulse sequence (not to scale) where a $\pi/2$ pulse-τ sequence gets the spins into the xy plane. The following $\pi/2$ pulse orients the dephased spin ensemble back along the z axis, while the ones that were dispersed enough in the xy plane remain unaffected by the $\pi/2$ pulse as they are parallel to the excitation field. The spins in the xy plane will decay with time T_2 whereas the spins along z are going to decay with time T_1. After the second $\pi/2$ pulse a time T is waited as the spins become entangled with the local nuclei fields that add the nuclear modulation to the charge carriers. The charge carriers themselves are weakly coupled and therefore no signal from spin-spin interactions shows up in the amplitude modulation of the signal.

The final $\pi/2$ pulse-τ-$\pi/2$ pulse is used to read out the echo amplitude. By changing T for each measurement a decay is measured which will have an amplitude modulation. The cartoon signal below the Bloch spheres shows how the charge measured has a superimposed oscillatory signal.
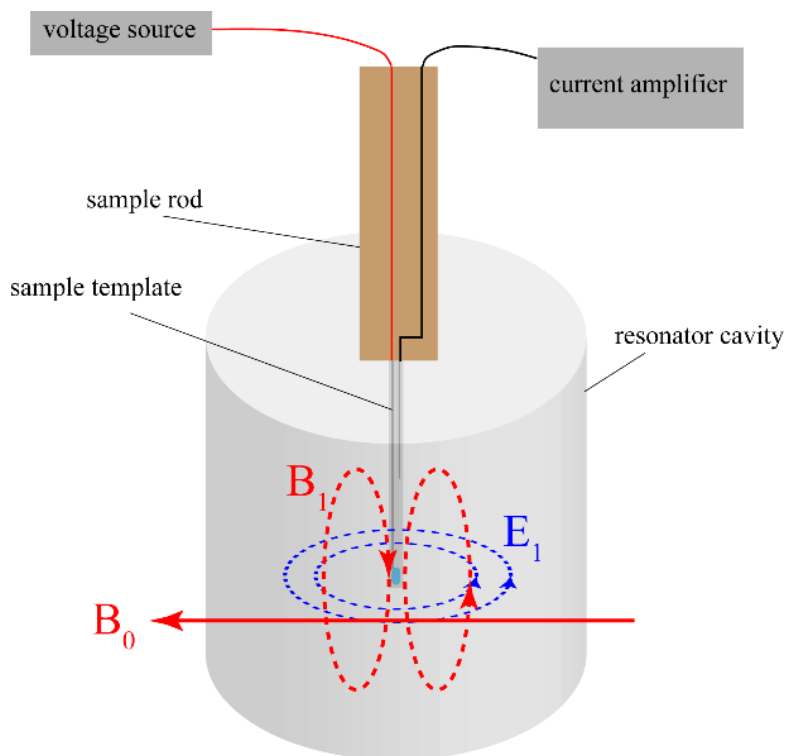
Figure 4.1: Illustration of a cylindrical dielectric pulse microwave resonator used in this study for the application of large (mT range) oscillating (within the X-band) magnetic fields to electronic devices allowing for EDMR measurements. While the magnetic field (red) at the resonator center is parallel to the resonator's symmetry axis, the electric field (blue) is circular. The sample is on a template that minimized inductive coupling to the radiation by minimizing the electric fields. The leads on the sample rod show how the device is biased with the red lead representing the positive terminal.
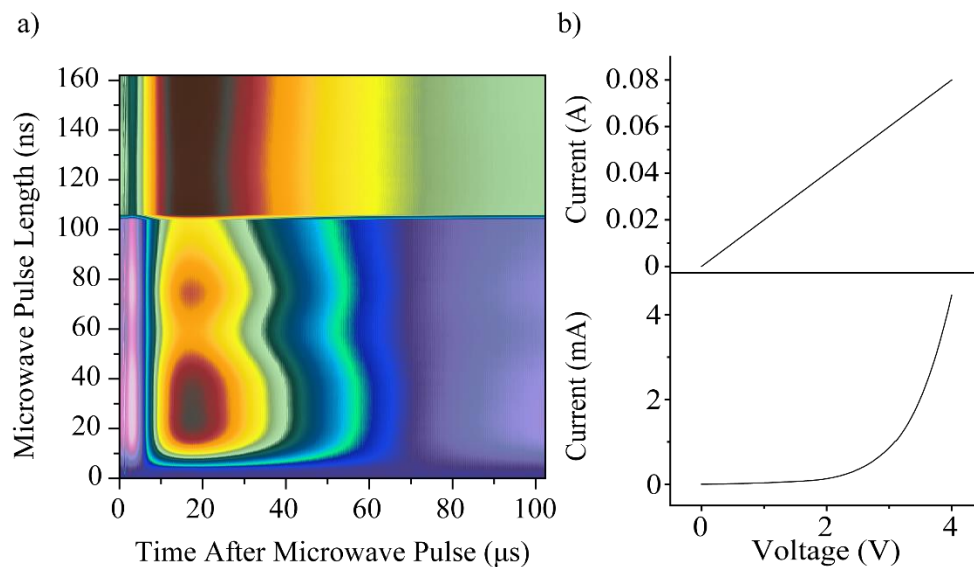
Figure 4.2 Device instability: a) Plot of the device current with arbitrary color units of a large area PFO OLED as a function of time after a brief microwave pulse is applied and a function of the length of this pulse. After these transient measurements are recorded for pulses with about 105ns, an abrupt change of the device takes place. This change, after which the device exhibits Ohmic behavior, is an indication for a device breakdown, a reproducible event for large area device templates. (b) Plots of the current-voltage characteristics of the device after and before the measurement shown in a) were conducted confirming the diodic behavior before and the Ohmic behavior after the breakdown.
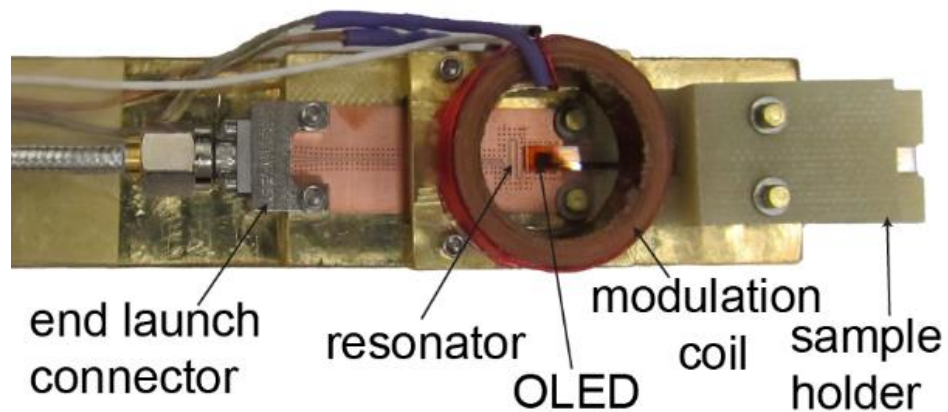
Figure 4.3: Photograph of the coplanar waveguide setup after installation in a probe head that is compatible with a commercial Oxford flow cryostat. The bronze section labeled resonator is the circuit board on which the CPWG is built and the modulation coils are placed to produce a static field directly on the active area of the device held in place with pressure applied by the sample holder. Detailed in reference [53].
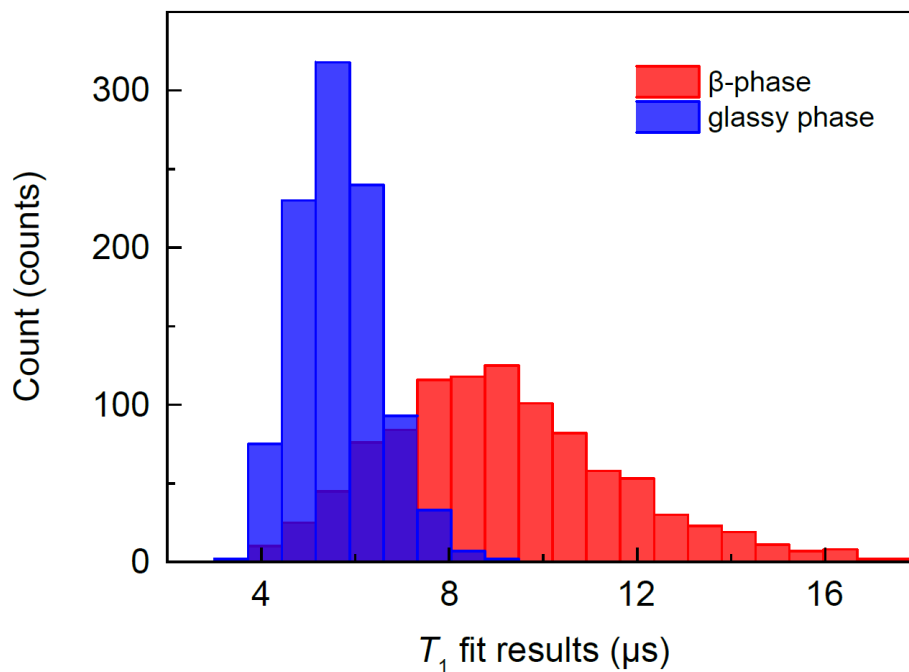
Figure 4.4: Histograms of T_1 values as determined using a bootstrap error analysis with 1000 iterations for both glassy phase (blue) and β-phase (red), using the datasets from Fig. 8.5. The Gaussian nature for both probability distributions is evident for both histograms. Four T_1 values occurring at $T_1 > 18$ μs are omitted to improve clarity of the plot.
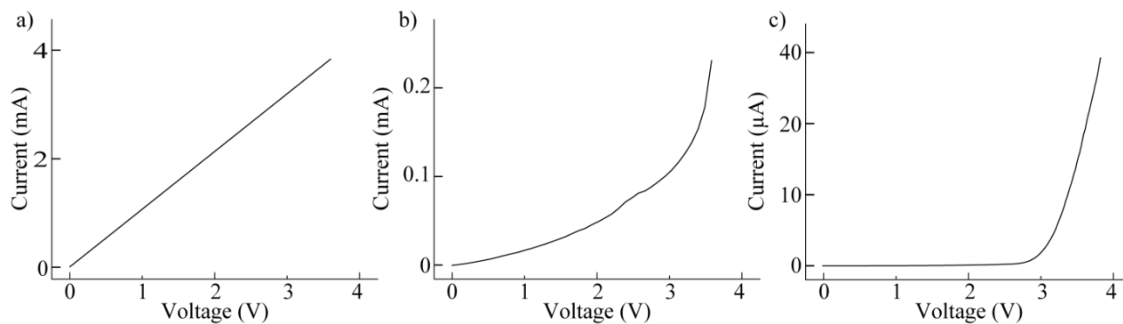
Figure 4.5: Three different current voltage (IV) curves measured on three nominally identical devices: a) IV characteristic showing a shorted sample where there is no diodic behavior but only ohmic behavior, b) IV characteristic showing a shunted device where there is a domain of nonlinear current increase but also an Ohmic domain in the low-bias domain , and c) an IV curve with almost no current in the low-bias domain, followed by an exponential increase of the current when the bias exceeds a "turn-on" voltage.
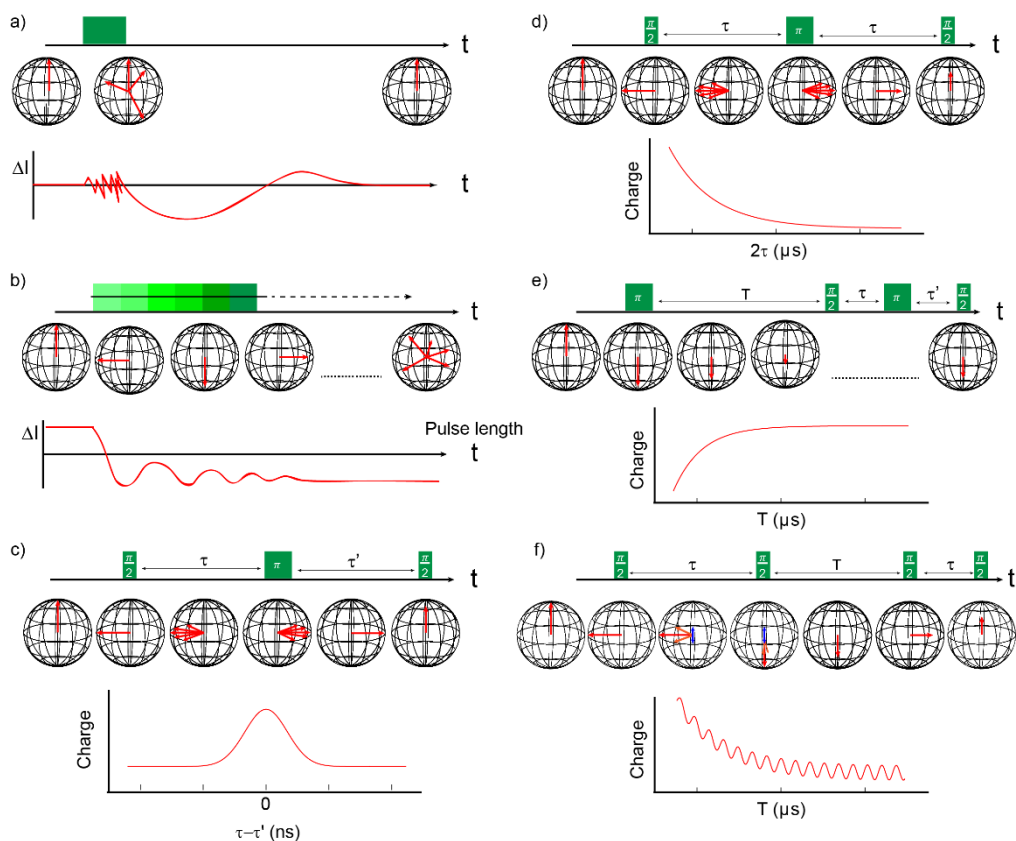
Figure 4.6: Illustrations of pulse sequences of six different pEDMR experiments used in this study, how those pulses affect the magnetic resonantly manipulated spin ensembles, represented by Bloch sphere depictions, as well as hand-drawn sketches illustrating the qualitative behavior of spin-dependent transition rates ΔI as functions of time. The pulses of each experiment are denoted by the green rectangular squares and labeled π and $\pi/2$ when they are meant to induce nutation by specific angles. The six sketches illustrate a) single pulse transients measurements [47], b) spin-Rabi oscillation (transient nutation) experiments [47]; c) electrically detected-Hahn echoes [125], d) Hahn Echo decays [20], e) inversion recovery [68], and f) ESEEM [20]. Note that some Bloch spheres in a) and b) indicate random orientations for the spin ensemble.

CHAPTER 5

EDMR MEASUREMENTS ON PFO THIN-FILM DEVICES

This chapter is focused on the implementation of EDMR experiments specfically for the PFO based OLED devices discussed above. The device characterization measurements of PFO based OLED devices that are conducted prior to each EDMR experiments are shown and discussed before the qualitative properties of EDMR signals in PFO are introduced. Segments of this chapter are reprinted from the paper: *Morphology effects on spin-dependent transport and recombination in polyfuorene thin films*, submitted for publication to Phys. Rev. B and coauthored by K. J. van Schooten, S. Jamali, G. Joshi, H. Malissa, J. M. Lupton, and C. Boehme.

5.1 Diode and PFO Phase Characterization

For the study of material phase effects on spin-dependent electronic transitions in PFO, reliable knowledge about the material's phase for each sample is crucial. Thus, before any pEDMR measurements can be taken, the phase of the PFO in this particular device has to be verified. The machines and procedures for these characterization measurements are described in section 4.6.1.2. For each device, IV curves are taken directly following fabrication, right before and after EDMR measurements are conducted. All data shown in

the following chapters are collected on OLEDs exhibiting IV curves similar to the data shown in Fig. 4.5 c) for the example of a good IV curve.

Fig. 5.1 (a) illustrates the OLED device structure used in this study. The structure is based on a glass template: indium tin oxide (ITO) (100 nm) is used as a transparent anode, poly(3,4-ethylenedioxythiophene) polystyrene sulfonate (PEDOT:PSS) is a hole injection material that is spin coated (at 3000 rpm) onto the cleaned ITO surface, and PFO in either morphology is the active layer that is spin coated in a nitrogen glovebox to form a thickness of approximately 75 nm. A thin (7 nm) calcium layer is then thermally evaporated to inject electrons, and 100 nm of aluminum is used to contact and encapsulate the device. The device is further encapsulated using either an epoxy or a so-called spin-on-glass (Futurrex IC1-200), for measurements at cryogenic temperatures, to ensure minimal atmospheric contact to the device during transport from the glovebox to the vacuum of a cryostat that is part of the spin resonance spectrometer.

To ensure absolute control over the morphological phase of the PFO OLEDs, the electroluminescence (EL) spectra were recorded for all devices. The EL spectrum can be used to infer long-range translational order within the polymer since the glassy phase exhibits emission for the 0-0 transition near wavelengths of 425 nm, while the β-phase has its maximal peak centered at 440 nm. This difference in 0-0 transition is a reliable indicator of the morphological phase of the layer [90]. Fig. 5.1 (d-f) shows typical EL spectra for the glassy, mixed, and β-phases, respectively, along with illustrations of the polymer chains for each morphology.

All following measurements in this study were performed on devices with 200 μm diameter active areas under forward bias conditions so that a 20 μA forward current

through the OLED was established. Exceptions were made for the experiments in Chapters 8 and 9, which had a steady state current of 50 µA to increase signal but also a larger active sample area in order to operate the material under similar conditions. We measured the change in current due to the magnetic resonant excitation by subtracting the steady-state current from the measured device current. A high-pass filter on the SR570 current amplifier with a cut-off frequency of 30 Hz was used to filter out low frequency contributions.

5.2 Phased PFO EDMR Signal Sign Change

We begin by discussing the generic magnetic resonance signals observed in PFO OLEDs. Fig. 5.2 shows transient pEDMR signals for the two PFO phases, as well as for a device with an admixture of both phases, at both room temperature (293 K) and 10 K. Each panel depicts the change in current of a device from its steady-state current, encoded in the color scale, as a function of time after a 400 ns excitation pulse took place at time $t = 0$, plotted along the horizontal axis, and as a function of the applied magnetic field B_0, plotted along the vertical axis. The graphs to the right of each panel depict data subsets of the color plots that represent current changes as a function of applied magnetic field recorded at times where maximal changes in current occurred, as indicted by the red arrows on the horizontal axis. Results from the β-phase sample [Fig. 5.2(a, b)] are shown above those from the mixed phase sample [Fig. 5.2(c, d)] and the glassy phase sample [Fig. 5.2(e, f)]; data measured at 10 K are shown to the right of the room temperature measurements. Note the different color scales exist for the different data sets. The current changes representing the magnitude of the detected spin-dependent currents increase 2 to 4 times when the devices are cooled to 10 K. Closer inspection of the transients reveals that each device

shows a rather large change in current at shorter times, while a subsequent slower signal of opposite sign follows. The case in Fig. 5.2(d) is most instructive. Here, an initial enhancement in current is followed by a long-lived quenching. In the vicinity of the zero-crossing of the current change it can be seen that the quenching of the current overlaps with the tail of the initial enhancement peak around 40 μs after the microwave pulse: quenching and enhancement appear to occur simultaneously, implying that more than one spin-dependent mechanism must be active here.

To determine the change in signal sign seen in Fig. 5.2 we first focus on the relation between chain morphology and the initial sign (quenching or enhancement) of the OLED current change following resonant excitation. The morphology can be quantified by considering the EL spectra. The inset in the upper left corner of Fig. 5.3 explains the procedure in relating the morphology to the initial sign of the transient current change. The inset illustrates the definition of two charges A_1 and A_2 as integrals of the current change in the time intervals between the resonant pulse and the sign change, and between the sign change and the relaxation of the current to the steady state (when the current change vanishes), respectively. Note that this inset is a sketch and not experimental data. Based on these charges, we introduce a normalization of A_1 by considering the ratio of A_1 to the sum of the magnitude of A_1 and A_2. This ratio represents the percentage of integrated charge that is due to initial current enhancement when the ratio is positive. When the ratio is negative, it represents initial current quenching. The main plot of Fig. 5.3 contains experimentally obtained values for this enhancement ratio (pEDMR experiments) for various PFO samples, prepared such that glassy, β-phase as well as the mixed phase emerged as a function of the morphology composition ratio detected in EL.

The latter is an observable that is defined by the second inset in the lower right corner of Fig. 5.3, which shows a cartoon of an EL spectrum (see Fig. 5.1) which is fitted with two Gaussians whose integrated intensities G and β represent the EL intensities of the glassy (G) and β-phase, respectively. We now define the EL detected morphology composition ratio as $G/(|G| + |\beta|)$. The black line connecting the data points in Fig. 5.3 is a guide to the eye. Fig. 5.3 shows that even with a significant glassy component in the EL spectra, the pEDMR signal sign can be dominated by current quenching characteristic of the β-phase. This observation is consistent with the observation made in Fig. 5.2 that β-phase EDMR signals are significantly stronger compared to those of glassy phase samples.

5.3 Discussion

The results shown in Fig. 5.2 demonstrate that the microscopic ordering of the π-conjugated polymer PFO does indeed play a role in the quantitative nature of spin-dependent transitions in this material. The most significant effect is the sign change in resonantly induced current changes between amorphous (glassy) and ordered (β) phases. The magnitude of the current-transient response also differs substantially. Both phases show an increase in signal strength at 10 K for most measurements with respect to room temperature. The quenching occurring simultaneously with an enhancement, seen in Fig. 5.2(d) around 40 μs after the excitation pulse, indicates that there must be more than one single spin dependent process, since a single process can only give rise to either quenching or enhancement, but not both at the same time [3].

The reason for the inversion in sign in the transient current signal between the two types of devices (glassy or β-phase) in Fig. 5.2 is presently unclear. It is most certainly not

due to the presence of the aforementioned additional spin-dependent channel. Also, all measurements were taken with the identical detection setup and nominally equivalent RC time constants of the devices. The RC time (~100 ns) is typically much shorter than the characteristic timescales of the current dynamics, so capacitive effects should not cause the change in resonance sign observed in Fig. 5.2. A straightforward hypothesis is that the sign change originates from a change in balance of spin-dependent dissociation and recombination rates which describe the resonant current transients [63]. Given identical measurements parameters a change in signal sign as discussed in Ref [126] can be attributed to dissociation rates, pair generation, and intersystem-crossing. In Fig. 5.1(e) an EL spectrum for a mixed phase device is shown. There is a strong emission peak near 425 nm, characteristic of the glassy phase of PFO, while the second peak coincides with both the 0-1 glassy transition peak and the 0-0 emission of the β-phase. β-phase polymer chains are presumably energetically favorable for charge carriers as indicated by the red shifted emission of the β-phase film. Consequently, in a mixed-phase film, charge carriers will preferentially take paths through the active layer via β-phase chromophores rather than glassy-phase chromophores. Pure glassy-phase films are hard to achieve in device fabrication as the polymer will tend towards arranging itself in the preferential low-energy conformation of the β-phase. While a device can have a majority of glassy-phase polymer chains, remaining β-phase chains throughout the active layer can play a substantial role in the resulting EDMR signal. The color scales in Fig. 5.2 show that the β-phase devices display a much larger change in current when compared to the glassy phase devices. Hence, a small percentage of β-phase polymer chains within a predominantly glassy-phase film can have a larger effect than the predominantly glassy-phase chains and overpower the

signal originating from the glassy phase. Fig. 5.2(c, d) shows a change in signal sign between 293 and 10 K measurements of the mixed phase film, as well as relatively weak current change signals ΔI compared to pure β-phase devices. The spin-dependent properties of the mixed phase devices therefore indeed lie between the two extremes of glassy and β-phase.
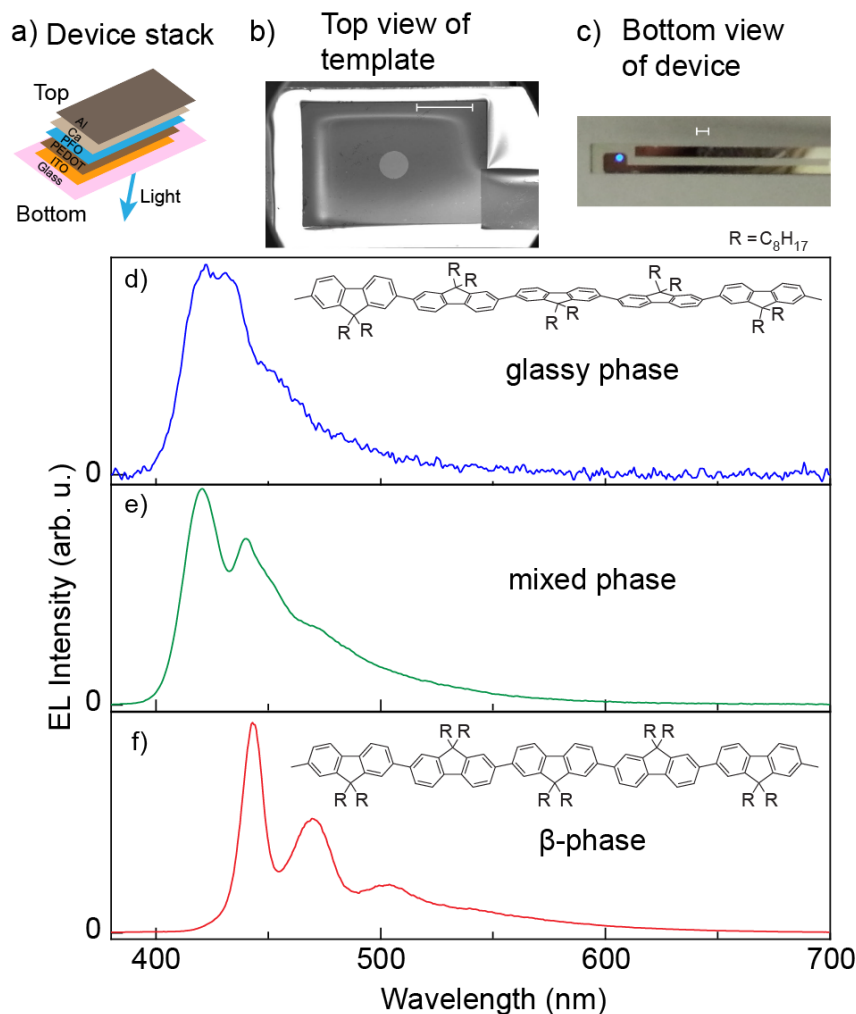
Figure 5.1 Device active layers and areas as well as EL spectra: (a) Illustration of the vertical device stack used in all measurements of this study where the active layer of PFO (blue) is sandwiched between a Ca layer (light grey) and a PEDOT:PSS layer (brown) for electron and hole injection, respectively. (b) SEM image of the active area of a standard device covered with SiN to insulate the ITO except for a small circular opening in the center, defining the active area. The small active device area atop the large substrate allowed for sufficient heat sinking of the power dissipated by the device under operation. (c) Photograph of a device under operating conditions with the blue PFO EL visible. The scale bars in (b) and (c) both represent 1 mm. The EL spectra for glassy, mixed and β-phase devices are plotted in (d), (e), and (f), respectively. Sketches of the polymer chain conformations for the two main phases are shown in their respective panels in order to illustrate the different states of molecular ordering.
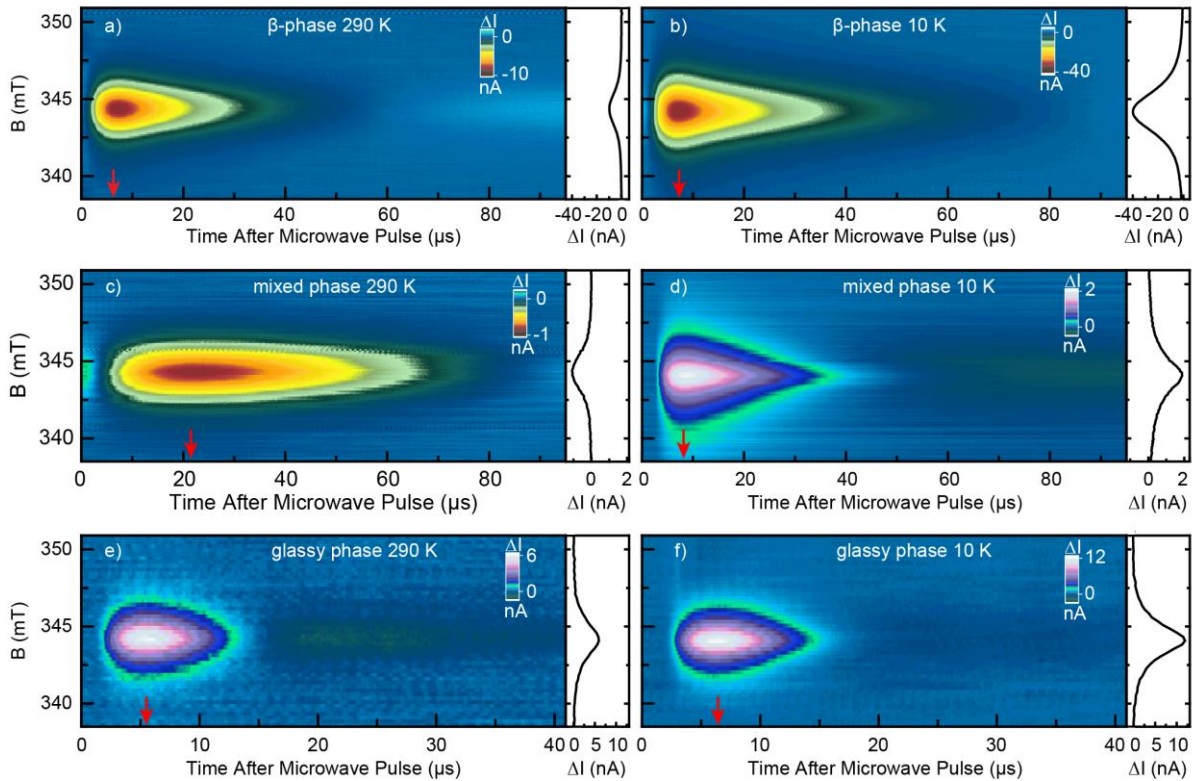
Figure 5.2: Plots of transient changes to a steady-state device current of I_0=20 µA after a 400 ns microwave excitation pulse was applied to the samples, as a function of the applied magnetic field which is represented by the vertical axis. The current transients were measured at 293 K (left) and 10 K (right), on devices containing PFO in the β-phase (a, b), a mixed phase containing both β-5.2e and glassy components (c, d) and the glassy phase (e, f). The insets of the panels display plots of the changes in device current as a function of the applied magnetic field for specific times after the microwave pulse indicated by the red arrows. Qualitatively, a sign reversal of the current change is seen between glassy and β-phases while for the mixed phase device a sign change occurs between high and low temperature. The data also show that magnetic resonance induced current changes in PFO are more than a factor of two larger in β-phase PFO compared to glassy PFO. The maxima of the current changes occurred for g-factors of 2.00327, 2.00324, 2.0033 for the room temperature data shown in panels (a), (c), and (e), respectively, and for g-factors of 2.00423, 2.00467, 2.00413 for the low temperature data shown in panels (b), (d), and (f), respectively with errors below 10^{-4}.
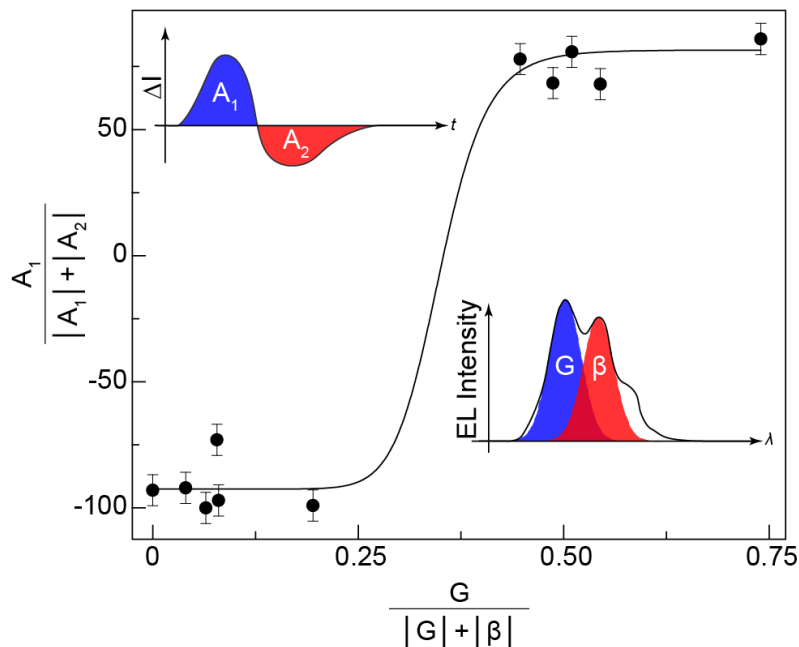
Figure 5.3: Correlation between EL spectrum and the sign of the initial steady-state current change following magnetic resonant excitation. The transient of current change is separated into two parts by its zero-crossing and integrated to yield areas A_1 and A_2 as sketched in the top left inset (this example transient is not experimental data). The ratio of A_1 to the sum of the moduli $|A_1|+|A_2|$ gives a measure of the sign of the initial part of the transient, either current enhancement or quenching. This ratio is related to the fraction of glassy-phase EL which is derived by deconvolution of the EL spectrum into glassy emission and β-phase emission. The fraction of the glassy phase is defined as the ratio between the glassy phase EL peak intensity G divided by the total EL intensity $|G|+|\beta|$, as illustrated in the bottom right inset. The black line is a guide to the eye. The data reveal that the sign of the steady-state current change of PFO OLEDs is governed by the fraction of glassy to β-phase.

CHAPTER 6

SPIN-DEPENDENT PROCESSES IN POLYFLUORENE

In Chapter 4, several different spin-dependent processes are discussed regarding their possible account for signals seen in EDMR measurements. This chapter shows that some of these mechanisms are present PFO, namely the polaron pair process and the triplet-exciton polaron process. Segments of this chapter are reprinted from the paper: *Morphology effects on spin-dependent transport and recombination in polyfuorene thin films*, submitted for publication in Phys. Rev. B and coauthored by K. J. van Schooten, S. Jamali, G. Joshi, H. Malissa, J. M. Lupton, and C. Boehme.

6.1 The Polaron Pair Process

Earlier studies on organic semiconductor compounds similar to PFO have pointed to the polaron pair (PP) process as the dominant origin of these transient magnetic resonance signals [11,57,58,127–129]. However, these earlier studies always showed a transient enhancement in current followed by a long-lived reduction (quenching). It is unusual that one and the same material can either show initial enhancement [i.e., Fig. 5.2(e)] or quenching [i.e., Fig. 5.2(a)]. Thus, mixed-phase devices are particularly interesting since they show quenching at 293 K and enhancement at 10 K. This variation in the sign of the

magnetic resonantly induced current change can be explained by a change in transition rates, or the involvement of additional spin-dependent processes beyond the electron-hole PP process. One way to determine if there is more than one spin dependent channel (i.e., in addition to the PP process) is to fit the EDMR spectrum at maximum amplitude (shown to the right of the colored panels in Fig. 5.2) with double Gaussian lines of equal area. Each charge in the pair should contribute to the resonance signal equally if the signal is due to a PP process. Each resonant spin (electron and hole) experiences inhomogeneous hyperfine broadening of slightly different magnitude, explaining the appearance of two Gaussians.

Fig. 6.1 shows EDMR resonance spectra by plotting the change in current along the vertical axis as a function of magnetic field along the horizontal axis. The data are the same as shown in the insets of Fig. 5.2. Here, each plot shows the measured data (open squares) fitted with equal-area Gaussian curves (blue lines), and the combined fits of the two Gaussians (red lines). The residuals of each fit are shown above each panel. The data from the glassy phase device at 293 K (b) produce the only fit result that does not show a distinct structure in the residual given its signal-to-noise ratio. Structures in the residuals above the noise level imply that the two Gaussians do not provide a perfect fit to the spectra. Since these spectra offer only a snapshot of spectral broadening at one particular time after resonant spin excitation and for one particular magnetic field strength, we refrain from simply comparing spectral widths between the different phases for these measurements based on the data in Fig. 6.1. Instead, we will comprehensively discuss the magnetic field dependence of the resonance spectra below in Chapter 7, which allows an extraction of the spectral line widths as a function of Zeeman splitting and offers a direct comparison between the two morphologies.

All the spectra shown in Fig. 6.1 were taken at the first maximum after the microwave pulse. In order to determine how the signal evolves with time, every spectra along the time axis of a field map for glassy device was fit using Lorentzian. If the PP process is the sole spin-dependent recombination channel the time dependence of the resonance should remain constant [21]. The value of the full width half maximum (FWHM) of each individual fit result was plotted as a function of time after the microwave pulse to see if the resonance width changed with time; the early and middle stages are omitted as they are the cross-over sections and thus supply unreliable results that show diverging widths, as evident by the tail end of the early signal in Fig. 6.2.

Lorentzian fits were used in lieu of double Gaussian fits simply so that a single data point (FWHM) of the total signal can represent the resonance. Also, as seen in Fig. 6.1 a double Gaussian is not the perfect model and thus any arbitrary measurement of width, as long as it is consistent, should show if the FWHM changes throughout a measurement. The inset in Fig. 6.2 shows a spectra of a mixed phase device in the crossover region where an enhancement and quenching are clearly seen to occur at the same time. This can only happen if there is more than one spin dependent channel occurring in the device. It could be due to there being four types of charge carriers in a device, two holes and two electrons for the glassy and β-phase polymers. In order to account for that the spectra would need to be fit with four Gaussians which could only increase the fit quality so much, as with two Gaussians the fits seen in Fig. 6.1 have $R^2 = 0.99$. This again indicates that while the PP model is not perfect it is very good and the dominant signal in the PFO spectra.

6.2 Triplet-exciton Polaron Process

Since the double-Gaussian fits shown in Fig. 6.1 do not lead to entirely vanishing residuals, we conclude that the PP process described by the double Gaussian function is not the only mechanism contributing to the signals observed in PFO. In order to identify these additional spin-dependent conductivity mechanisms, we carried out EDMR spectroscopy in the half magnetic-field domain in order to investigate the potential occurrence of a triplet-exciton polaron (TEP) process that has been observed before in other polymer films [37,130]. Triplet excitons can be quite short lived at room temperature, so their influence should be more pronounced at low temperatures [21]. The half-field measurements are conducted in the same manner as the measurements depicted in Fig. 5.2, but the magnetic field is set to slightly more than half the magnetic field where direct transitions between the sublevels of the triplets can become allowed for the given excitation pulse frequency.

While no half-field signal is observed in related conjugated polymers such as MEH-PPV at 293 K [21], PFO is known to have a potentially high triplet exciton density in the β-phase, owing to the longer triplet lifetime than for MEH-PPV, which could make room-temperature detection possible [95,131]. Fig. 6.3 shows the change in current as a function of magnetic field for β-phase (red triangles) and glassy phase (blue circles) OLEDs for both 293 K and 10 K. A half field resonance cannot be resolved for either phase at 293 K but is clearly visible at 10 K. Panels (c, d) show measurements at 10 K, where each resonance slice gives an average of multiple measurements to improve the signal to noise (4 averages were made for the β-phase and 6 for the glassy phase). The 293 K measurements were also averaged (22 averages for the β-phase, 9 averages for the glassy

phase).

The half-field resonances can be fitted by a standard procedure using the EasySpin MATLAB toolbox in order to determine D, the dipolar coupling parameter of the spin pair of the triplet exciton [132,133]. The error estimate for D was calculated using a bootstrap analysis [121] (appendix B). The β-phase zero-field splitting parameter of the triplet exciton is determined to be $D = 2407 \pm 128$ MHz, while the glassy phase gave $D = 2317 \pm 732$ MHz. Even though the amplitudes of the half-field resonances differ between the two morphological phases, the zero-field splitting parameters D appear to be quite similar. The residuals of the fits (black lines) in Fig. 6.3(c, d) are shown above the resonance curves. For the β-phase, it appears that there is some structure in the residual close to the resonance. Such a residual could be interpreted to imply that a third spin-dependent process, besides the PP and the TEP mechanisms, is present in PFO. This conclusion can also be drawn by noting that there is no detectable half-field resonance at 293 K in β-phase PFO, yet a clear structure in the fit residual of the full-field resonance is seen in Fig. 6.1(a). Even though the TEP mechanism is not detectable by the available EDMR experiment at room temperature, an additional nondominant spin-dependent mechanism must exist.

6.3 Discussion

The conclusion drawn in section 6.1 regarding the presence of more than a PP process is reaffirmed by the structure in the residuals of the Gaussian fits to the spectra in Fig. 6.1 for β-phase devices at 293 K (panel a) and 10 K (panel c) along with the glassy phase devices at 10 K (d). These fits also show that at least for room temperature that there is one dominating spin-dependent electronic transition while the other spin-dependent

mechanism is significantly weaker in magnitude as corroborated by the weak (or absent) residuals at 293 K in Fig. 6.1 (a, b). For the dominant spin-dependent signal at room temperature, all evidence found in this study points towards the PP mechanism, the spin-dependent recombination of electrons and holes. These carriers first form weakly spin-coupled pairs due to Coulomb attraction before they recombine into singlet or triplet excitations, dependent on the PP spin state.

At 10 K, a TEP process is seen in both phases of PFO due to the appearance of a half-field resonance, but the PP process remains the dominant spin-dependent mechanism for the polymer at both temperatures studied. The dominance of the PP process is demonstrated by the spectral analysis of the magnetic-field slice of the resonance and the appearance of Rabi spin-beating at a frequency of $2\gamma B_1$. The zero-field splitting parameters of the triplet exciton are found to be very similar for the two phases, implying a similar degree of localization of the triplet. The values for D are also consistent with earlier measurements on similar polymers [122]. However, the TEP process appears to be more prominent in the β-phase than in the glassy phase, which likely relates to the longer triplet lifetime in the ordered material, in agreement with earlier studies of photoinduced absorption spectroscopy of the triplet state [93].

There may potentially be another spin-dependent transport process present in PFO that was not discerned in this study. Looking at Fig. 6.1 it is clear that there is a residual of some sort for at least the β-phase device at room temperature, but there is no discernable half field signal. Ergo, the PP process is not the sole factor in the device signal, and the TEP process is not present at that temperature which points to an unknown factor or process. That being said the overall effect of the unknown signal is significantly small. It

is conceivable that the extra signal could be due to a small portion of PFO in the opposite phase present in the device. Fitting the resonance with four Gaussians, however, will not give any better insight into this given the reasonable fit accrued with just two.
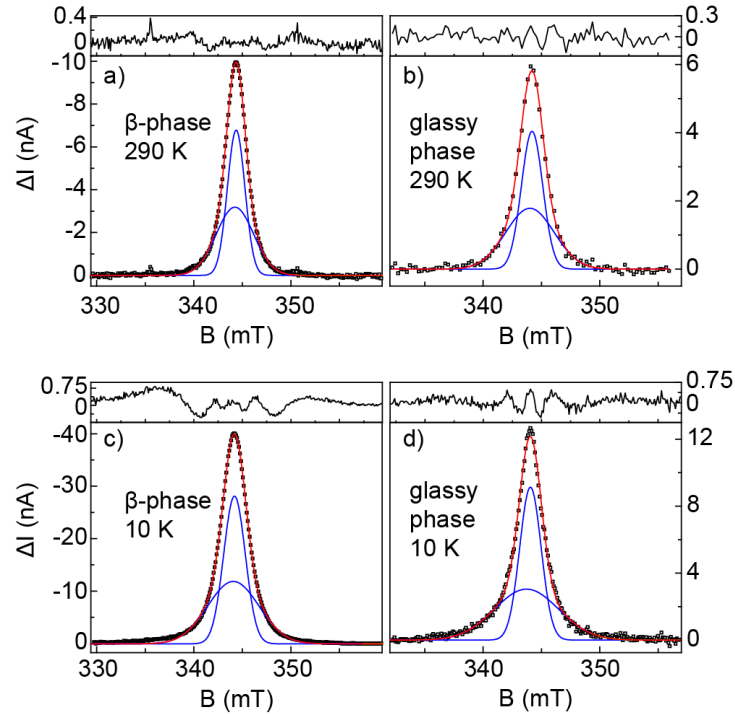
Figure 6.1: Plots of the measured maximal current change (black squares) after the resonant pulse excitation as a function of applied static field B_0 obtained from the data shown in Fig. 5.2 for β- and glassy phases at temperatures of 293 K (a, b) and 10 K (c, d). The blue lines are fit results with double-Gaussian functions, representing electrons and holes, in which both functions have the same area as required for a pair process. The quality of the fit results is recognized by the fit residuals which are plotted in the insets of the panels. Weak but significant structure is discernible in the residual data sets, indicating that additional spin-dependent processes not described by a double-Gaussian line make minor contributions to the overall EDMR response of the devices. We note that within the given errors, no *g*-factor difference between the two resonance peaks was observed. For each data set, the *g*-factors of both Gaussian functions are described by the values provided in Fig. 5.2.
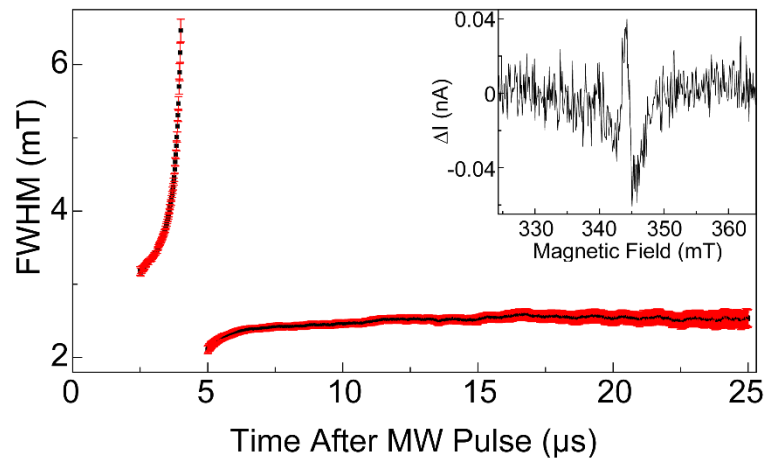
Figure 6.2: Displays the full width half maximum (FWHM) of a Lorentzian fit of each resonance slice as a function of time after the microwave pulse. The omitted data points are the flat, cross-over sections where the signal changes sign and thus has approximately no signal. The inset shows a slice in the crossover time for a mixed phase device.
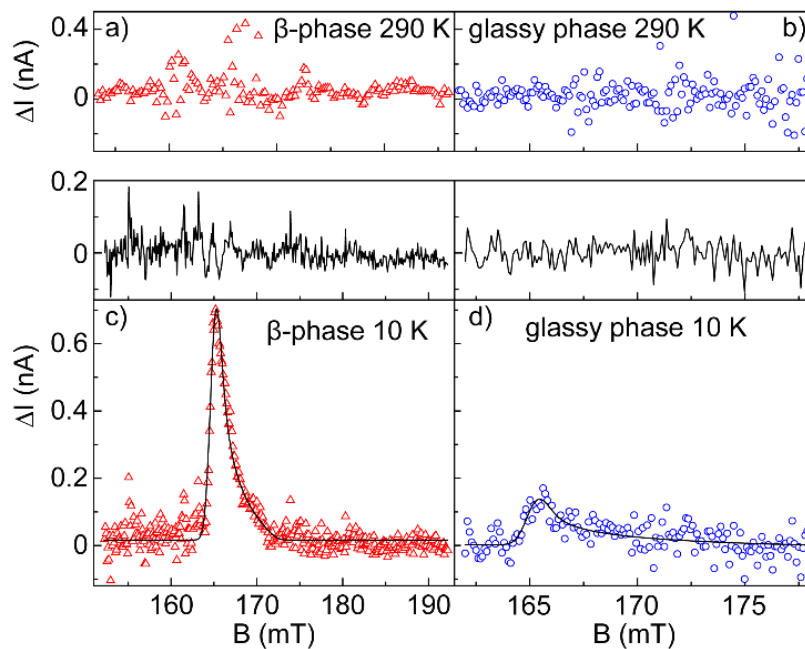
Figure 6.3: Plots of half-field resonance spectra for *β*-phase (red triangles) and glassy-phase (blue circles) devices at 293 K (a, b) and 10 K (c, d). Each panel shows a change in steady-state current as a function of magnetic field. The fits in (c, d) were calculated using the EasySpin MATLAB toolbox in order to determine the zero-field splitting parameter *D*. A bootstrap error analysis was used to establish the error in the fit parameters. No discernable signal was found for either phase at 293 K.

CHAPTER 7

HYPERFINE AND SPIN-ORBIT STRENGTHS IN POLYFLUORENE

This chapter discusses the utilization of capacitively coupled coplanar wave guides to preform cw EDMR measurements at several different frequencies. The equipment used in the acquisition of the data in this chapter is discussed in section 4.3 and expanded upon in 4.7.3. Multiple resonant peaks with different widths allow for the use of a global fit to extract the dependence of the hyperfine and spin-orbit strengths in PFO OLEDS of both phases. A bootstrap routine was used to determine the errors in the global fit. Segments of this chapter are reprinted from the paper: *Morphology effects on spin-dependent transport and recombination in polyfuorene thin films*, submitted for publication to Phys. Rev. B and coauthored by K. J. van Schooten, S. Jamali, G. Joshi, H. Malissa, J. M. Lupton, and C. Boehme.

7.1 Results of Globally Fitting Multifrequency cw EDMR Spectra

The line shape of the PFO full-field resonances shown in Figs. 5.2 and 6.1 is wider than that of similar polymers [27,39,67,134–136]. Inhomogeneous broadening of a magnetic resonance line of an amorphous material can result from local hyperfine interactions or a distribution in g-factors which can arise from spin-orbit interactions. In

order to determine how much of the resonance width is due to hyperfine coupling, arising from the abundance of hydrogen atoms in PFO, and what contribution results from spin-orbit coupling, multiple resonances were measured using coplanar waveguide resonators operating at different frequencies [53]. This approach is chosen because the two contributions to resonance line widths have different magnetic field dependencies: hyperfine broadening occurs independently of the external magnetic field strength, whereas spin-orbit coupling is manifested by a distribution of g-factors and therefore gains more influence on the spectrum for higher static magnetic field strengths.

For the multifrequency EDMR experiments, the coplanar waveguide (CPW) resonators were operated under magnetic-field modulated continuous wave (cw) excitation as opposed to the pEDMR measurements discussed above. Consequently, the change in current as a function of magnetic field, i.e., the magnetic resonance spectrum, is recorded as a derivative function. Many frequencies are available in the CPW due to the use of the higher harmonics of each fundamental frequencies for a given resonator. This allows one to measure EDMR at a number of different magnetic fields and develop an understanding of how the line shape of the resonance changes with magnetic field strength. Fig. 7.1 a) shows the change in current due to multiple resonances for both glassy (blue) and β-phase (red) as a function of magnetic field (bottom horizontal axis) and corresponding frequency (upper axis). Since the magnetic field scale is so broad, the individual resonances appear very narrow.

As described in detail in Ref. [53] for a different polymer material, the multiple resonance spectra obtained through such a procedure can be analyzed by fitting all spectra simultaneously using a global fit with two field-dependent line widths ΔB_1 and ΔB_2 given

by $\Delta B_{1,2} = \sqrt{B_{Hyp_{1,2}}^2 + (\alpha_{1,2}B_0)^2}$. This relation is based on a two-Gaussian model, representing one Gaussian function for the electron spin resonance and one for the hole spin resonance, which together form an ensemble of PPs undergoing spin-dependent recombination. This approach allows us to deduce the exact distribution width of the random hyperfine fields of each carrier 1 and 2 ($B_{Hyp_{1,2}}$) as well as the spin-orbit controlled g-factor distribution widths ($\alpha_{1,2}$). Fit results to the resonances for both polymer phases are shown in Fig. 7.1 b) for the lowest (upper curve) and highest (lower curve) frequencies recorded. The curves are shifted along the abscissa by the magnitude of the magnetic field on resonance, $B - f/\gamma$, with γ being the gyromagnetic ratio. The fits are clearly of acceptable quality even though they are made under neglect of the above discussed second spin-dependent process and, more importantly, even though these global fit models are applied to a frequency span of a factor of 20. The fit quality does appear to deteriorate at higher frequencies for both phases of the material. The results of the fits are summarized in Table 7.1. Note that the black fitting curve is actually one and the same fit for each phase, since a global fit is carried out over all data and the only variable in the plotted function is the magnetic field strength B.

We applied a bootstrap error analysis to the results of the global fits for both material phases to arrive at a better understanding of the uncertainty in the hyperfine and SO terms as described in detail in Ref. [53]. Fig. 7.1 (c) shows the 95% confidence interval for the resonance line width (ΔB) for both the narrow and wide Gaussian lines of the resonances (blue, glassy phase; red, β-phase) as a function of magnetic field. These errors were extracted from the bootstrap analysis and are stated in Table 7.1. The circles and triangles in the plot mark the magnetic field strengths of each resonance spectrum taken in panel a).

The broader the resonance line, the larger the error in extrapolating the line width. Clearly, all features do indeed broaden with increasing magnetic field, implying contributions to line broadening from spin-orbit coupling resulting in a distribution Δg.

7.2 Discussion

In both polymer conformations, the line width in the limit of low excitation frequencies is determined solely by hyperfine coupling between charge carrier spins and hydrogen nuclei. It is significantly larger than what has been observed in other organic semiconductor materials [27,57,58,67]. The line width increases with excitation frequency, which also points to a strong contribution of spin-orbit coupling. In comparison to the hyperfine fields as strong as those found in PFO, the minute effects of spin-spin interactions are negligible. The glassy-phase devices exhibited larger hyperfine broadening but a slightly smaller spin-orbit term than the ordered β-phase. One possible explanation for the counterintuitive observation of stronger hyperfine coupling in the glassy phase devices (where the proton density is lower due to the disorder) is a stronger localization and broader conformational and energetic distribution of the possible charge carrier states. A related effect is known from amorphous Si:P, where the field splitting of the hyperfine lines is 24 mT as compared to 4.2 mT in crystalline Si:P [137]. The double Gaussian derivative line shape used to globally fit the c.w. EDMR resonances describes the measured spectra well at low excitation frequencies, but deviates progressively for higher frequencies. The individual fits for the glassy-phase resonances went from fit qualities of $R^2 = 0.966$ at 2.33 GHz to $R^2 = 0.712$ at 17.89 GHz. The β-phase at 1.15 GHz fitted with $R^2 = 0.982$ but only $R^2 = 0.852$ at 19.88 GHz. These deviations at higher frequencies could

be partially due to the spin-dependent processes not accommodated by the PP model, i.e., possibly a TEP process [21,40,53]. Such a TEP process becomes apparent, for example, by comparing EDMR and EL-detected MR (ELDMR), where the former can contain signatures of spin-dependent transport but the latter only reports on spin-dependent recombination [40]. However, the TEP and the PP mechanisms must contribute equally to lower-frequency spectra where excellent fit agreements are achieved under all conditions (Fig. 6.1), and consequently there is no reason to assume an additional process. It is therefore more likely that the deteriorating fit quality at higher frequencies (Fig. 7.1) is caused by the inadequacy of the assumption that the *g*-factors are isotropic. As spin-orbit contributions become increasingly significant at spectra recorded at higher frequencies, the *g*-factors may increasingly require representation by the full *g*-tensors. Whether or not this hypothesis is correct, though, can only be resolved experimentally through EDMR experiments at frequencies much greater than the 20 GHz used here.

Even with the imperfect two-Gaussian model for the global fit, the results of the bootstrap analysis (see Table 7.1) show a significant increase of hyperfine field strength in the glassy phase compared to the β-phase. The distributions of the *g*-factors *Δg* between spin species, or the overall *g*-factor anisotropy (*g*-tensor), are all very similar except for the order-of-magnitude greater value seen in the broad resonance peak for the β-phase. We therefore conclude that there is likely very little influence of chain shape on spin-orbit coupling. However, chain shape does affect hyperfine coupling: in the more disordered material, proton densities can increase locally, raising local hyperfine fields and inducing spectral broadening.
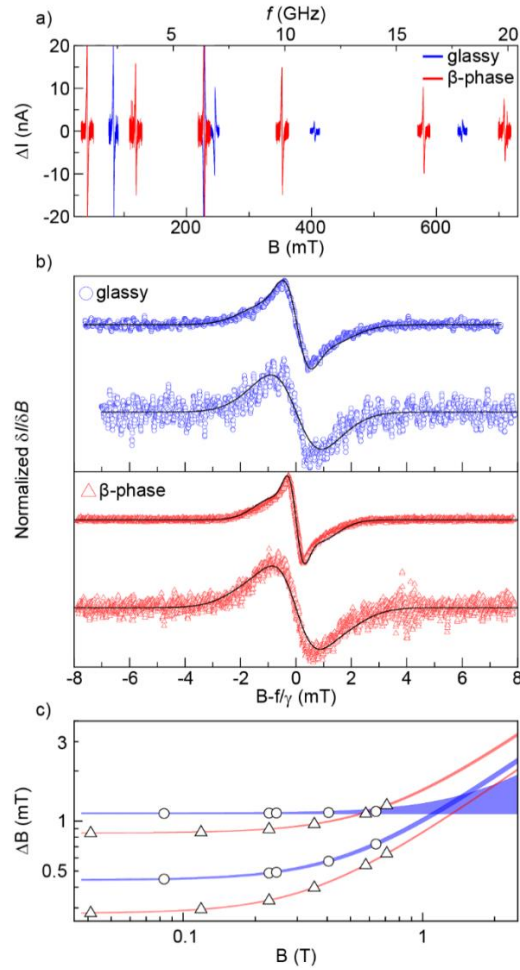
FIGURE 7.1: Multifrequency continuous wave (c. w.) EDMR spectra obtained by using coplanar waveguide (CPW) resonators. (a) C. w. spectra of glassy and β-phase OLEDs, shown in blue and red, respectively. The change in current is shown as a function of both static magnetic field (bottom) and the corresponding magnetic resonance frequency for an uncoupled electron with the vacuum g-factor (top axis). Note that c. w. spectra have a differential lineshape compared to the pulsed spectra in Fig. 6.1. (b) Plot of normalized resonance spectra for different magnetic field scales as a function of the offset relative to the observed resonance center, obtained from devices with glassy (blue circles) and β-phase (red triangles) PFO. For each phase, the resonances for the lowest and highest frequency (2.33 GHz and 17.89 GHz for the glassy phase; 1.15 GHz and 19.88 GHz for the β-phase) are displayed. The solid black line represents the result of a global fit with multifrequency dependent double-Gaussian derivatives that model both low and high-frequency data. All fits reveal the superposition of a broad and a narrow Gaussian. (c) Plots of the widths ΔB of the two Gaussians for the two phases as a function of the applied on-resonance magnetic field B based on the fit results obtained from the global fit procedure. The shaded regions represent 95% confidence intervals resulting from the parameter uncertainties that were determined using a bootstrap analysis. The circles and triangles represent the values of the continuous red and blue plots highlighted for the magnetic fields at which experimental spin resonance data were obtained.

TABLE 7.1: Boundary values of the 95% confidence intervals for the double-Gaussian fit results of the multifrequency c.w. EDMR data presented in Fig. 7.1. The ranges correspond to the shaded regions in Fig. 7.1 (c). Line broadening arises due to both magnetic field-independent hyperfine coupling B_{Hyp} and field-dependent broadening due to a distribution Δg in g-factors, denoted by the parameter α. Hyperfine coupling is substantially stronger in the glassy phase than in the β-phase, even though the compounds are chemically identical. The broad line of the β-phase resonance shows significantly stronger broadening with magnetic field, suggesting that spin-orbit coupling may be stronger in the β-phase than in the glassy phase.

β-phase		Glassy phase	
Narrow line	Broad line	Narrow line	Broad line
$0.276 \leq B_{Hyp} \leq$ 0.280 (mT)	$0.841 \leq B_{Hyp} \leq$ 0.851 (mT)	$0.436 \leq B_{Hyp} \leq$ 0.446 (mT)	$1.101 \leq B_{Hyp} \leq$ 1.120 (mT)
$7.98 \leq \alpha \leq 8.17$ (10^{-4})	$1.25 \leq \alpha \leq 1.31$ (10^{-3})	$8.71 \leq \alpha \leq 9.43$ (10^{-4})	$\alpha \leq 6.11 \times 10^{-4}$

CHAPTER 8

ELECTRICALLY DETECTED COHRET SPIN MOTION IN PFO

The influence of coherent spin effects on conductivity phenomena are currently not only very intensively studied for new spintronic applications, including spin memory, but also for spin quantum information concepts [15]. Here such effects are utilized in order to study the nature of spin-dependent processes. Organic semiconductors typically have shorter coherence times than inorganic material due to the low SOC. This chapter contains the first study of spin coherence effects on charge carrier transport in PFO. First, Rabi spin nutation experiments are discussed which in turn lead to the probing of transverse and spin-lattice relaxation times. Segments of this chapter are reprinted from the manuscript: *Morphology effects on spin-dependent transport and recombination in polyfuorene thin films*, submitted to Phys. Rev. B and coauthored by K. J. van Schooten, S. Jamali, G. Joshi, H. Malissa, J. M. Lupton, and C. Boehme.

8.1 Rabi Oscillations and Hahn Echoes

OLEDs have shown remarkable signatures of spin coherence such as spin beating between precessing electron and hole spins [38] and time-resolved electron-nuclear spin precession [138], phenomena which both show a strong dependence on hydrogen isotope.

PFO is a unique material to investigate spin coherence effects since the two phases are chemically identical but structurally distinct: is there an effect of polymer structure on spin coherence? Fig. 8.1 shows the transient current response following a microwave pulse as a function of pulse duration for glassy and β-phase OLED devices. If the carrier spins retain their coherence, then spin-Rabi flopping becomes apparent in the device current [128]. Figs. 8.1 (a, d, g, j) show the transient current response following a microwave pulse of varying duration. In order to improve the visibility of coherent Rabi oscillations as a function of microwave pulse length, the background was subtracted with a second-order polynomial function. This procedure is described in detail in Ref. [27]. The change in current is shown on a color scale as in Fig. 8.1. The amplitude B_1 of the excitation microwave pulse strength for the measurements in Fig. 8.1 is approximately 560 μT. Panels (b, e, h, k) show slices along the respective white dashed lines to better portray the oscillation in device current as a function of excitation pulse length. The first few nanoseconds of each slice are omitted to better fit the data into the given scale for the displayed range of pulse lengths. As expected, all four data sets – for the two phases at the two temperatures – show coherent oscillations in the current. However, one can clearly see that the oscillations at 293 K decay more rapidly than those at 10 K.

The Rabi oscillations can be further analyzed by considering the frequency components making up the oscillation. Fig. 8.1(c, f, i, l) shows the Fourier transform of the time domain data for the time slices marked in white. To prevent distortions of the Fourier spectra by the baseline subtraction mentioned above, all transforms were carried out on the uncorrected data without baseline subtraction. All Fourier spectra show a dominant fundamental at the Rabi frequency γB_1, corresponding to the oscillation of one spin-½

carrier species. However, a second harmonic component is also seen at a frequency of $2\gamma B_1$, which arises due to simultaneous coherent precession – spin beating – of both the electron and hole spin. The detection of this spin-beating component is proof that the dominant spin-dependent transition for the observed EDMR signals is governed by weakly coupled pairs with spin s=1/2. This beating is consistent with the PP recombination mechanism which has previously been observed in MEH-PPV. The second-harmonic peaks in panels (c, i) are less pronounced than those in panels (f, l) because of the faster decay of the Rabi oscillations at room temperature. The beating component is, again, clearly visible in the 10 K data, and more so in the glassy phase than in the β-phase.

The Rabi oscillations on their own only demonstrate that coherent spin precession contributes to the device current under magnetic resonance excitation, but do not allow us to extract spin relaxation times. We use electrically detected Hahn-spin echo experiments and inversion recovery measurements to determine spin relaxation and dephasing times. We determine the necessary duration of the echo-driving π-pulse, which rotates the spins by 180° from their thermal equilibrium orientation along the direction of the external field B_0 to $-B_0$, from the duration of the Rabi oscillation at a given microwave power. Details of the echo experiments on OLEDs are given elsewhere [138,139]. Note that for the electrical detection of spin echoes, for which spin permutation symmetry rather than spin polarization is observed, it is necessary to modify the Hahn-echo pulse sequence well known for inductively detected magnetic resonance spectroscopy by adding an additional π/2-pulse. This pulse projects the charge carrier spins onto their eigenstates along the $\pm B_0$ axis. This procedure is explained in Ref. [125,138] and the *Supporting Information* thereof. Fig. 8.2 shows examples of Hahn echoes measured on PFO devices. The actual pulse sequence is

illustrated above the figure, and the echo shape is recorded by varying the timing of the projection pulse (τ').

8.2 Transverse Spin-relaxation Times (T_2)

Fig. 8.2 shows representative current-detected Hahn echoes for both PFO phases at room temperature and at 10 K (red shows the β-phase and blue the glassy phase). All data sets can be fitted with a simple Gaussian function which serves as a guide to the eye. The echoes measured at 10 K show a greater change in overall charge (i.e., time-integrated current) than those measured at room temperature. Fig. 8.3 shows the decay of the echo envelope, i.e., the Hahn echo signal as a function of delay time 2τ (with $\tau' = \tau$) at 293 K (a) and 10 K (b) for both β-phase (red triangles) and glassy phase (blue circles), allowing us to determine the transverse spin-relaxation times T_2. A mixed-phase device (black pentagons) was also measured at 293 K to explore whether a distinct change in T_2 arises from a blend of phases. Since the glassy-phase devices are significantly more unstable than the β-phase samples, rapid measurements are necessary in order to maintain device integrity throughout a measurement. As a consequence, fewer data points were recorded for glassy phase devices. The signal-to-noise ratio of the 10 K β-phase measurement was low, and we therefore used a bootstrap error analysis in order to reliably determine upper and lower bounds for the T_2 values. The black lines show fits of single exponential decays for each data set. The resulting values for T_2, given in Table 8.1 are of the same order of magnitude as those found in OLEDs made of other organic semiconductor molecules [68]. Similarly, very little effect of morphology is seen on the decoherence times T_2.

8.3 Spin-lattice Relaxation Times (T_1)

Up to now the term π-pulse has been used without any rigorous proof that it does flip the spins 180°. Estimates of the pulse lengths can be found from time transient rabis [124,128] and confirmed to a certain degree via Hahn echo signals, in order to ensure that the π and $\pi/2$ pulses are correct inversion recovery pulse optimization is done. The pulse sequence for inversion recovery optimization is very similar to the pulse sequence outlined in Fig. 4.6 e), only it differs by changing the length of the initial pulse (starting at 0) and maintains the same delay time **T**. Again the Hahn echo sequence is used as a polarization readout scheme so that our observable (charge) can be related to spin polarization.

Fig. 8.4 is an inversion recovery optimization measurement, from a β-phase device, that shows the spin polarization is completely flipped from the initial steady state, at pulse length equal to 0, by ~34 ns. This gives us a reliable π-pulse length. Obviously this only works when our ventured π and $\pi/2$-pulses are in the correct ballpark so we can use the Hahn echo sequence to read out the polarization.

Spin relaxation is characterized both by the spin coherence time T_2 and the spin-lattice relaxation time T_1. In order to determine T_1 we conducted inversion recovery experiments. Intermediate pairs (PPs) can either dissociate or recombine where they couple further in excitons, which could affect the T_1 measurements if either process occurs before an irreversible spin flip [63,124]. The pulse sequence is depicted above Fig. 8.5. A π-pulse is applied before a Hahn echo sequence, and the mixing time T is varied. T_1 is usually longer than T_2 [68]. The data in Fig. 8.5 are plotted as the total detected charge as a function of mixing time T. The β-phase data are shown in red and glassy-phase in blue with respective

fits in black. Both data sets were recorded at 293 K. No measurements were carried out at 10 K. Since the β-phase OLED had a larger active area than what was used for the other measurements (500 μm diameter rather than 200 μm), a higher steady-state current of 50 μA was used to reach approximately the same current density as in the other measurements (~600 A/m^2). The extracted values for T_1 are summarized in Table 8.1. Again, little difference is seen between the two phases.

8.4 Discussion

PFO devices are particularly instructive for understanding the relation between spin-coherence, as revealed by electrically detected spin-Rabi oscillations, and the underlying spin coherence times, which can be extracted using Hahn echoes. Although substantial differences in the fidelity of Rabi oscillations appear to exist, with the highest-quality oscillations apparent in the 10 K glassy-phase data, there is very little quantitative difference in the spin lifetimes. The glassy phase shows a charge-carrier spin coherence time of $T_2 = 237 \pm 37$ ns with a spin lattice relaxation time $T_1 = 5.6 \pm 0.9$ μs, both at 293 K. The β-phase coherence time was marginally longer at $T_2 = 295 \pm 10$ ns; the spin lattice relaxation time of the β-phase film was also slightly larger, $T_1 = 9.1 \pm 2.5$ μs. The different charge carriers (electrons and holes) have strongly overlapping resonances, shown in Fig. 6.1, implying that their individual relaxation times cannot be probed separately but only as an ensemble. This similarity in values is consistent with the assumption that decoherence is driven by hyperfine interactions [139], since hyperfine coupling strengths are within the same order of magnitude for both phases of the material even though detectable differences in hyperfine-field strengths do exist.

Figure 8.1 Time transient Rabis: (a, d, g, j) Plots of the change in device current after a short, pulsed magnetic resonant excitation at *t*=0 as a function of time (horizontal axis) and pulse length (vertical axis) for both PFO phases at 293 K (top row) and 10 K (bottom row). The microwave pulse strength for all measurements was ~560 µT. The current transients are baseline corrected using a second-order polynomial to highlight the Rabi oscillations. (b, e, h, k) show corresponding slices along the dashed white line. (c, f, i, l) show the real component of the Fourier transforms that were calculated using data slices without background subtraction. The Fourier amplitude is plotted as a function of frequency in units of spin-½ Rabi frequency γB_1, where γ denotes the gyromagnetic ratio. Every frequency spectrum exhibits a peak in its signal intensity at the fundamental frequency of γB_1 indicating the involvement of paramagnetic states with spin s=1/2. The 10 K measurements also show smaller peaks at $2\gamma B_1$, though less visible in the β-phase (f). This second harmonic is indicative of beating of the observed paramagnetic centers, the electron and hole spins.

Figure 8.2: Plots of electrically detected Hahn echo experiments observed in the time-integrated current of devices with both PFO phases at 293 and at 10 K. The pulse sequence used for these experiments is sketched above the plots. Both plots show the integrated current (the charge) as a function of time difference τ - τ' defined in the sketch of the pulse sequence. This difference was chosen such that the center of the electrically detected spin echoes occurs around τ - τ' ≈ 0 for better comparison. The solid lines are fits with Gaussian curves and serve as a guide to the eye.
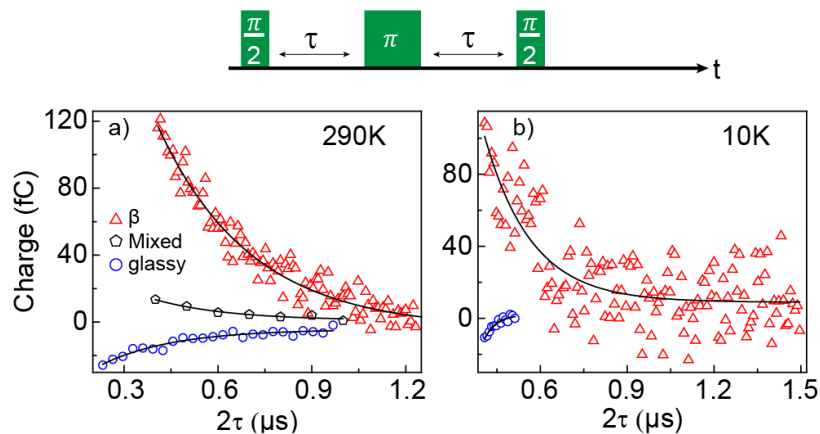
Figure 8.3: Plots of the decays of the Hahn echo envelopes measured at 293 K (a) and 10 K (b) as a function of 2τ (defined in the pulse sequence diagram above). (a) Data were recorded from a mixed-phase device (black pentagons), a glassy-phase device (blue circles), and a β-phase device (red triangles). All measured data sets were fitted with single exponential decay functions in order to determine the coherence times T_2 of the charge carrier spin states.
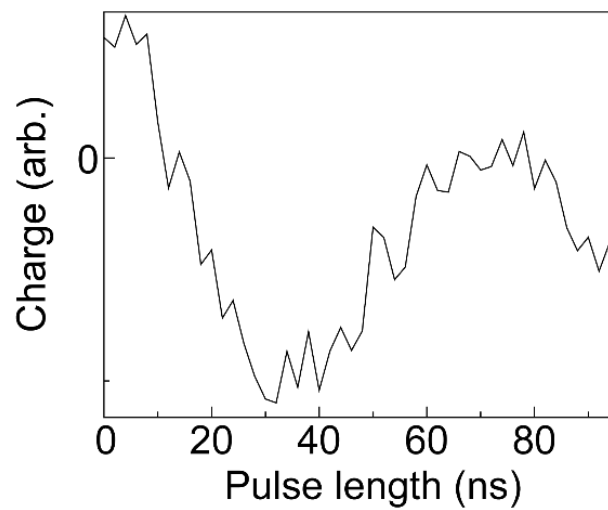
Figure 8.4: Inversion recovery optimization experiment showing charge as a representation of spin polarization as a function of initial pulse length. This measurement shows a π-pulse should be roughly 34 ns to completely flip the spin of the sample.
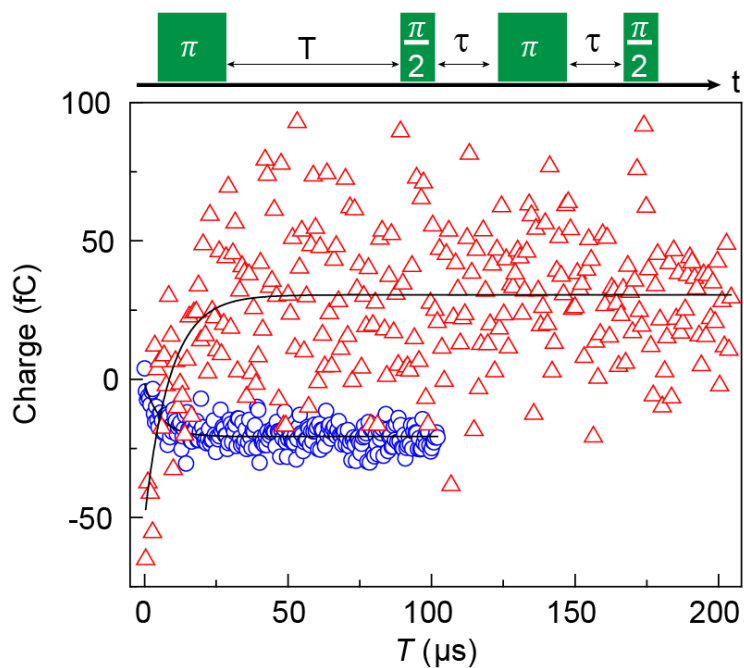
Figure 8.5: Plots of the results of inversion recovery experiments for glassy-phase (blue circles) and β-phase (red triangles) PFO OLEDs measured at 293 K. The time-integrated current (charge) is plotted as a function of mixing time (T) that follows the initial π pulse. An electrically detected Hahn echo sequence is used for readout. The EDMR pulse sequence used is shown above the plot. The β-phase OLED was forward biased so that the device current was 50 µA, with a circular active area of 500 µm diameter. The glassy device had a smaller active area with 200 µm diameter. It was operated at a current of $I_0 = 20$ µA.

TABLE 8.1: Results of the bootstrap analysis of T_1 and T_2 times for the different phases of PFO. The errors stated represent one-sigma confidence intervals. The two-sigma values overlap for all phases, implying that there is no significant change in coherence time between the phases. The spin-lattice relaxation times for the β-phase appear to be slightly longer than for the glassy phase.

	Decoherence time T_2		Spin-lattice relaxation time T_1
	at 293 K	at 10 K	at 293 K
Glassy phase	237 ± 37 ns	590 ± 280	5.6 ± 0.9 (μs)
Mixed phase	253 ± 82 ns	N/A	N/A
β-phase	295 ± 10 ns	252 ± 35	9.1 ± 2.5 (μs)

CHAPTER 9

ELECTRON SPIN ECHO ENVELOPE MODULATION

This chapter is the last to contain data acquired for this study. Seemingly unnecessary, as PFO is made with only hydrogen and carbon atoms, electron-spin-echo envelope modulation (ESEEM) measurements were conducted to determine what nuclei are producing the hyperfine fields and interacting with the charge carriers. However the results were not as straightforward as one would assume. Segments of this chapter are reprinted from the manuscript: *Morphology effects on spin-dependent transport and recombination in polyfuorene thin films*, submitted to Phys. Rev. B and coauthored by K. J. van Schooten, S. Jamali, G. Joshi, H. Malissa, J. M. Lupton, and C. Boehme.

9.1 EDMR Measurement of ESEEM in PFO

In order to investigate the nature of the hyperfine couplings, which are responsible for the random effective magnetic fields governing the line width at low excitation frequencies, electron-spin-echo envelope modulation (ESEEM) measurements were performed. In echo measurements, the exponential decay of the echo amplitude, the echo envelope, is modulated slightly due to precession of the local nuclear magnetic moments in the course of the echo decay. Such modulations are not always observed, but when they arise, they

provide a direct fingerprint of the dominant isotope responsible for hyperfine coupling. Fig. 9.1 shows stimulated echo ESEEM experiments, following the procedure outlined in Ref. [138] with an illustration of the stimulated three-pulse echo sequence given above the figure. In such an experiment, nuclear polarization is generated by a $\pi/2$-τ-$\pi/2$ pulse sequence acting on the electronic spins. The system then evolves freely for a mixing time T, and a stimulated echo is generated by another $\pi/2$ pulse. The final $\pi/2$ readout pulse is required for electrical detection when the spin-dependent current is governed by spin permutation symmetry rather than spin polarization [69,138,140]. The resulting echo signal at 293 K is shown in panel (a) for the two phases, where a Gaussian fit is again used as a guide to the eye. The stimulated echo amplitude is recorded as a function of mixing time T with $\tau^* = \tau$ and is shown in panel (b).

The β-phase device used in this experiment was operated at a current of 50 μA due to this particular sample being manufactured with a larger active area. The device had a 500 μm diameter opening in the SiN insulating layer, as opposed to the 200 μm used for the glassy sample. As expected, the larger pixel produces a larger signal. However, larger pixels also displayed more of a tendency to random current fluctuations. The OLEDs based on glassy PFO with identical device structure could not maintain a sufficiently stable current, hence the small area template was used in the glassy ESEEM measurements. The ESEEM decay shown in Fig. 9.1 b), measured as time-integrated current (charge), depicts the charge decay as a function of mixing time, T. Fine structure in the measured stimulated echo decays shown in panel (b) might appear to be noise. However, it is not noise but a well-defined harmonic contribution caused by the precession of nuclear magnetic moments. This effect is clearly revealed by the Fourier transform of the decay curve shown

in panel (c), where a distinct peak is seen around the frequency of 14.5 MHz for the β-phase OLED. This frequency corresponds exactly to the matrix proton frequency at the X-band field used, and therefore provides a clear demonstration of the hydrogen nuclei interacting with the PPs which in turn are responsible for conductivity. While the glassy-phase device shows a similar decay to the β-phase device in Fig. 9.1 b), there is no signal discernable at the hydrogen frequency in the Fourier transform in panel (c). However, this result does not allow for any conclusions, as the signal-to-noise ratio for an electrically detected ESEEM signal is less than unity for the glassy phase device (blue), below that of the more stable β-phase device. Given the chemical makeup of PFO, the fact that hyperfine-broadening appears to be larger in the glassy phase than in the β-phase (cf. Fig. 7.1) along with the general similarity of the spin-dependent processes in both phases strongly suggest that the charge carrier spins of the glassy phase should also experience oscillations close to 14.5 MHz. They are simply not detectable with the given experiment. This limitation can, in principle, be overcome by averaging over more repetitions of the experiment. However, we estimate that the duration of an experiment capable of resolving the hydrogen signal in the glassy device would exceed the lifetime of our devices made from this phase. We note that it is well known from single-molecule spectroscopy that the β-phase is much more photostable than the glassy phase [88], so it is not surprising that the same also holds for devices.

9.2 Discussion

The role of hyperfine coupling becomes particularly clear in the ESEEM experiments where we observe an echo envelope modulation signal corresponding to the hyperfine

coupling to hydrogen nuclei. This spectral signature has been confirmed only in the β-phase samples, but the absence in the glassy-phase devices is probably only related to the low signal-to-noise ratio and poorer device stability.
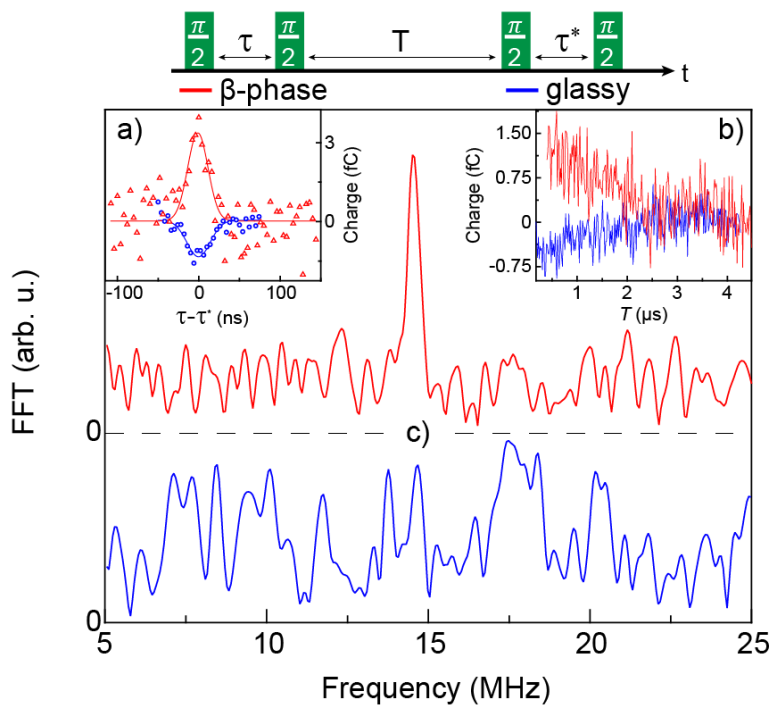
Figure 9.1: Plot of the stimulated and electrically detected echo measurements revealing the presence of an electron spin-echo envelope modulation (ESEEM) at room temperature. The definition of the pulse parameters τ and T is shown in the sketch of the pulse sequence used. Blue and red data points represent results from glassy and β-phase devices, respectively. Panels a) and b) show the stimulated echoes and their decays for on-resonance measurements at a magnetic field of 344 mT. The stimulated echo is measured with a constant mixing time ($T = 180$ ns) and delay time τ while τ^* is varied (red and blue lines). For (b), $\tau = \tau^* = 96$ ns, with T being varied. In (c) the Fourier transforms of the envelope modulations contained in the data in (b) are plotted, revealing a strong peak at 14.5 MHz for the β-phase device. This frequency corresponds to the proton Larmor frequency for the applied magnetic field. No significant modulation is seen in the glassy-phase device because of insufficient signal to noise.

CHAPTER 10

SUMMARY AND OUTLOOK

PFO is an intriguing material that has many unique characteristics among organic semiconductors. While non-spin related device applications based on PFO seem unlikely given the stability and the material's sensitivity against joule heating, the influence of morphological order on the spin-dynamics, the hyperfine and the spin orbit interaction of charge carrier spins could be of interest for polymer based spin applications and spin devices. Changing the lattice between phases also led to a noteworthy change in spin-lattice relaxation times, giving a possible means to produce longer lived spin states within such materials.

The work presented in this study has encompassed a range of measurement techniques and thoroughly probed the differences molecular order causes in spin-dependent charge carrier processes in PFO. The dynamics of spin-dependent recombination differs significantly between the two PFO phases that are studied, while the respective spin-coherence times are quite similar, not only in the two materials phases but also compared to those of other polymers. Also similar to other polymers is that the PP process is the dominant spin-dependent electronic transition in both PFO phases while at low-temperatures, the triplet-exciton-polaron process becomes pronounced. Finally, there is

also a third process involved in spin-dependent charge transitions whose exact nature could not be resolved in the course of this study. The fact that changes in molecular order change hyperfine field strengths and spin-orbit coupling induced g-factor distributions has led to the main conclusion of this work, namely that molecular order in PFO can be used to tune these materials parameters which are crucial for potential spintronics applications, including sensors and memory applications. Further work is needed to explore such possibilities. Due to the broad line width of the polaron pair magnetic resonance signals that is shown in this study, such future work would likely require EDMR spectroscopy at frequencies higher than the 20 GHz that have been reached in this study. Furthermore, as molecular order is also tunable in other conducting polymers [i.e., Poly(3-hexylthiophene-2,5-diyl), P3HT] [56], conducting a similar study on this polymer could lead to additional interesting results.

Morphological changes in PFO have also shown significant changes to other observables, albeit none of these changes were as pronounced as the changes seen for SOC and hyperfine interactions. This is intriguing as it provides another way to tune the materials characteristics by ordering.

APPENDIX A

MATLAB CODES

Segments of this Appendix are reprinted from the manuscript: *Morphology effects on spin-dependent transport and recombination in polyfuorene thin films*, which has been submitted for publication to Phys. Rev. B and coauthored by K. J. van Schooten, S. Jamali, G. Joshi, H. Malissa, J. M. Lupton, and C. Boehme.

The following code is for the error determination of the hyperfine fields and spin-orbit coupling parameters in PFO using a global fit. The error determination is based on the bootstrap procedure discussed in Chapter 4. The Global fit is the function "`BFit`," used to fit the different beta phase spectra, measured with the CPWGs, together. Prior to the for loop the different arrays we want to keep track of, each representing a fit parameter, must be established. The bootstrap portion of this code is in the center, while the two grayed sections before and after are for the initial fit and parameter setup and the display of the results, respectively. Keep in mind the initial least squares fit was implemented in order to determine the model spectra (`mod_y`) and the residuals (`residuals = mod_y - I, R = residuals`) in the first gray section.

```
%% Generate data (in real life this would be experimental data)
clear;
```

```matlab
load('C:\Users\chad\PFO\Beta\BmT.mat')
load('C:\Users\chad\PFO\Beta\I.mat')

%start clock for script
tic

%% Do the bootstrap

% Fit the original data
[fitresult, gof] = BFit(BmT, I);

%exract fit reults needed for model fit
format long;
cof = coeffvalues(fitresult);
mA=cof(1);
mA1=cof(2);
mA2=cof(3);
mA3=cof(4);
mA4=cof(5);
mA5=cof(6);
mBh=cof(7);
mBh1=cof(8);
mR=cof(9);
mS=cof(10);
mS1=cof(11);
mg=cof(12);
mg1=cof(13);
mg2=cof(14);
mg3=cof(15);
mg4=cof(16);
mg5=cof(17);
my0=cof(18);

% Calculate the fit curve
mod_y = BetaFit(BmT, mR, mg, mg1, mg2, mg3, mg4, mg5, mA,
mA1, mA2, mA3, mA4, mA5, mBh, mBh1, mS, mS1, my0);

% Calculate the actual residuals
residuals = mod_y - I;

%extract non baseline residuals
R = residuals;
N1 = R(R > .55); %N1 is the noise above 0.03
N2 = R(R < -.55); %N2 is the noise below -.03
N = vertcat(N1,N2); %N is the noise who's magnitude is
larger than 0.03
```

```matlab
% Plot a histogram of the residuals
%use N if restricting residuals
%use R if leaving residuals if open
hist(R, 64)

% these are the arrays where we keep track of the
parameters we get from each
% bootstrap iteration bBh and bBh1 are the hyperfine fields
of both gaussians % respectively, bS and bS1 are the spin
orbit alpha values. bR is the ratio  % between both areas
of the double Gaussian fit.
bBh = [];
bBh1 = [];
bS = [];
bS1 = [];
bR = [];

% bootstrap loop (better to use a large number, small umber
to test)
nboot = 1000;
for i = 1:nboot
    % generate artificial residuals by picking random
elements from the
    % actual residuals (with replacement).
    % BmT is the vector containing the magnetic field,
sim_residuals must
    % have the same number of elements.
    sim_residuals = zeros(size(BmT));
    for j = 1:length(sim_residuals)
        % swithch R and N depending on residual
circumstance, R is the
        % residual vector (established above)
        k = randi(length(R));
        sim_residuals(j) = R(k);
    end
    % generate artificial dataset by using the fit curve
(see above) and
    % adding the artificial residuals
    sim_y = mod_y + sim_residuals;
    % fit the artificial dataset and get the resulting
parameters
    [fitresult, gof] = BFit(BmT, sim_y);
    format long;
    % need the long format for small numbers that are
rounded otherwise.
    % the following lines extract the fit results as a
vector with different
```

```matlab
    % coefficient values pertaining to each fit result.
Ordered by name so
    % you need to manually check which coefficient
represents which fit
    % parameter.
    cof = coeffvalues(fitresult);
    aBh=cof(7);
    aBh1=cof(8);
    aS=cof(10);
    aS1=cof(11);
    aR=cof(9);
    % append the parameters to arrays a and b
    bBh = [bBh, aBh];
    bBh1 = [bBh1, aBh1];
    bS = [bS, aS];
    bS1 = [bS1, aS1];
    bR = [bR, aR];
    % display the standard deviation of hyperfine and spin
orbit coefficients
    % these values should converge the longer the loop is
running
    fprintf('Iteration %d\t std(Bh) = %g\t std(Bh1) = %g\n
std(S) = %g\t std(S1) = %g\n', i, std(bBh), std(bBh1),
std(bS), std(bS1));
end

%% display the bootstrap results
Bh_std = zeros(size(bBh));
Bh1_std = zeros(size(bBh1));
S_std = zeros(size(bS));
S1_std = zeros(size(bS1));
for i = 1:length(bBh)
    Bh_std(i) = std(bBh(1:i));
    Bh1_std(i) = std(bBh1(1:i));
    S_std(i) = std(bS(1:i));
    S1_std(i) = std(bS1(1:i));
end
figure;
subplot(3, 2, 1);
plot(bBh);
xlim([1, nboot]);
xlabel('Bootstrap Iteration');
ylabel('Bh');
title('Parameter Bh');
subplot(3, 2, 2);
plot(bBh1);
xlim([1, nboot]);
```

```matlab
xlabel('Bootstrap Iteration');
ylabel('Bh1');
title('Parameter Bh1');
subplot(3, 2, 3);
hist(bBh, 64);
xlabel('Bh');
ylabel('#');
subplot(3, 2, 4);
hist(bBh1, 64);
xlabel('Bh1');
ylabel('#');
subplot(3, 2, 5);
plot(Bh_std);
xlim([1, nboot]);
xlabel('Bootstrap Iteration');
ylabel('Standard deviation of Bh');
subplot(3, 2, 6);
plot(Bh1_std);
xlim([1, nboot]);
xlabel('Bootstrap Iteration');
ylabel('Standard deviation of Bh1');
%plots for S (spin orbit coef)
figure;
subplot(3, 2, 1);
plot(bS);
xlim([1, nboot]);
xlabel('Bootstrap Iteration');
ylabel('S');
title('Parameter S');
subplot(3, 2, 2);
plot(bS1);
xlim([1, nboot]);
xlabel('Bootstrap Iteration');
ylabel('S1');
title('Parameter S1');
subplot(3, 2, 3);
hist(bS, 64);
xlabel('S');
ylabel('#');
subplot(3, 2, 4);
hist(bS1, 64);
xlabel('S1');
ylabel('#');
subplot(3, 2, 5);
plot(S_std);
xlim([1, nboot]);
xlabel('Bootstrap Iteration');
```

```matlab
ylabel('Standard deviation of S');

plot(S1_std);
xlim([1, nboot]);
xlabel('Bootstrap Iteration');
ylabel('Standard deviation of S1');

%plot of Area ratio
figure;
plot(bR);
xlim([1, nboot]);
xlabel('Bootstrap Iteration');
ylabel('R');
title('Parameter R');

%end stopwatch timer
toc
```

The code above is given for a global fit that will reveal the hyperfine and spin-orbit strengths. However, in principle, any arbitrary fit function can be used with this code by changing the data vectors (`BmT` and `I`) and the fit function (`BFit`). Any fit parameter can then be extracted by altering the coefficients in the "`fitresult`." Of course, the fit parameters that are wanted need to have the correct number of vectors created before the for loop (ie: `bBh = []; bBh1 = []; bS = []; bS1 = []; bR = []`). If fewer fit parameters are wanted then fewer vectors will be needed. In either case, the coefficients will be in a different order and it is crucial that the user manually checks to ensure the right coefficient of the "`fitresult`" is extracted in the bootstrap routine.

The equation "`BFit`" is used throughout the bootstrap code. This is a least squared fit used to get initial results and then the real residuals, "`R`," used in the bootstrap above. It is important to have reasonably accurate starting values for each parameter when there are numerous spectra being fit at the same time. The actual function that is being fit differs for every experiment as the frequencies and fields shift for each experiment. An example code is given below for a global fit trying to extract the hyperfine fields and spin-orbit strengths

of multiple double Gaussian derivatives and three normal absorbance spectra all being fit

together.

```
function I = PEDOT12specRatio(B, R, g, g1, A, A1, A2, A3,
A4, A5, A6, A7, A8, A9, A10, A11, A12, Bh, Bh1, S, S1, F,
F1, F2, F3, F4, F5, F6, F7, F8, F9, F10, F11, F12, y0)
% UNTITLED6 Summary of this function goes here
% Doble Gaussian Derrivative for 10 CW spectra and 3 EDMR
spectra
% 173 different spectra global fit with one eq.
% Detailed explanation goes here
% Bh, Bh1 are hyperfine fields; S, S1 are SO; g, g1 are
gyromagnetic ratios
% R is the ratio of the double Gaussian areas (As). Fs are
field calibrations
I               =               y0+A*((0.1/g)-B-F).*(exp(-((F+B-
0.1/g).^2)./(2*(Bh^2+(S^2)*(0.1/g)^2))))./...
(Bh^2+(S^2)*(0.1/g)^2)^(3/2)...
+(A/R)*((0.1/g1)-B-F).*(exp(-((F+B-
0.1/g1).^2)./(2*(Bh1^2+(S1^2)*(0.1/g1)^2))))./...
(Bh1^2+(S1^2)*(0.1/g1)^2)^(3/2)...
+A1*((0.2/g)-B-F1).*(exp(-((F1+B-
0.2/g).^2)./(2*(Bh^2+(S^2)*(0.2/g)^2))))./...
(Bh^2+(S^2)*(0.2/g)^2)^(3/2)...
+(A1/R)*((0.2/g1)-B-F1).*(exp(-((F1+B-
0.2/g1).^2)./(2*(Bh1^2+(S1^2)*(0.2/g1)^2))))./...
(Bh1^2+(S1^2)*(0.2/g1)^2)^(3/2)...
+A2*((0.3/g)-B-F2).*(exp(-((F2+B-
0.3/g).^2)./(2*(Bh^2+(S^2)*(0.3/g)^2))))./...
(Bh^2+(S^2)*(0.3/g)^2)^(3/2)...
+(A2/R)*((0.3/g1)-B-F2).*(exp(-((F2+B-
0.3/g1).^2)./(2*(Bh1^2+(S1^2)*(0.3/g1)^2))))./...
(Bh1^2+(S1^2)*(0.3/g1)^2)^(3/2)...
+A3*((0.4/g)-B-F3).*(exp(-((F3+B-
0.4/g).^2)./(2*(Bh^2+(S^2)*(0.4/g)^2))))./...
(Bh^2+(S^2)*(0.4/g)^2)^(3/2)...
+(A3/R)*((0.4/g1)-B-F3).*(exp(-((F3+B-
0.4/g1).^2)./(2*(Bh1^2+(S1^2)*(0.4/g1)^2))))./...
(Bh1^2+(S1^2)*(0.4/g1)^2)^(3/2)...
+A4*((0.5/g)-B-F4).*(exp(-((F4+B-
0.5/g).^2)./(2*(Bh^2+(S^2)*(0.5/g)^2))))./...
(Bh^2+(S^2)*(0.5/g)^2)^(3/2)...
+(A4/R)*((0.5/g1)-B-F4).*(exp(-((F4+B-
0.5/g1).^2)./(2*(Bh1^2+(S1^2)*(0.5/g1)^2))))./...
(Bh1^2+(S1^2)*(0.5/g1)^2)^(3/2)...
+A5*((1/g)-B-F5).*(exp(-((F5+B-
```

```
1/g).^2)./(2*(Bh^2+(S^2)*(1/g)^2))))./...
(Bh^2+(S^2)*(1/g)^2)^(3/2)...
+(A5/R)*((1/g1)-B-F5).*(exp(-((F5+B-
1/g1).^2)./(2*(Bh1^2+(S1^2)*(1/g1)^2))))./...
(Bh1^2+(S1^2)*(1/g1)^2)^(3/2)...
+A6*((2.24/g)-B-F6).*(exp(-((F6+B-
2.24/g).^2)./(2*(Bh^2+(S^2)*(2.24/g)^2))))./...
(Bh^2+(S^2)*(2.24/g)^2)^(3/2)...
+(A6/R)*((2.24/g1)-B-F6).*(exp(-((F6+B-
2.24/g1).^2)./(2*(Bh1^2+(S1^2)*(2.24/g1)^2))))./...
(Bh1^2+(S1^2)*(2.24/g1)^2)^(3/2)...
+A7*((3.185/g)-B-F7).*(exp(-((F7+B-
3.185/g).^2)./(2*(Bh^2+(S^2)*(3.185/g)^2))))./...
(Bh^2+(S^2)*(3.185/g)^2)^(3/2)...
+(A7/R)*((3.185/g1)-B-F7).*(exp(-((F7+B-
3.185/g1).^2)./(2*(Bh1^2+(S1^2)*(3.185/g1)^2))))./...
(Bh1^2+(S1^2)*(3.185/g1)^2)^(3/2)...
+A8*((6.19/g)-B-F8).*(exp(-((F8+B-
6.19/g).^2)./(2*(Bh^2+(S^2)*(6.19/g)^2))))./...
(Bh^2+(S^2)*(6.19/g)^2)^(3/2)...
+(A8/R)*((6.19/g1)-B-F8).*(exp(-((F8+B-
6.19/g1).^2)./(2*(Bh1^2+(S1^2)*(6.19/g1)^2))))./...
(Bh1^2+(S1^2)*(6.19/g1)^2)^(3/2)...
+A9*((17.435/g)-B-F9).*(exp(-((F9+B-
17.435/g).^2)./(2*(Bh^2+(S^2)*(17.435/g)^2))))./...
(Bh^2+(S^2)*(17.435/g)^2)^(3/2)...
+(A9/R)*((17.435/g1)-B-F9).*(exp(-((F9+B-
17.435/g1).^2)./(2*(Bh1^2+(S1^2)*(17.435/g1)^2))))./...
(Bh1^2+(S1^2)*(17.435/g1)^2)^(3/2)...
+A10*(exp(-((F10+B-120/g).^2)./(2*(Bh^2+(S^2)*(120/g)^2))))./...
(Bh^2+(S^2)*(120/g)^2)^(1/2)...
+(A10/R)*(exp(-((F10+B-
120/g1).^2)./(2*(Bh1^2+(S1^2)*(120/g1)^2))))./...
(Bh1^2+(S1^2)*(120/g1)^2)^(1/2)...
+A11*(exp(-((F11+B-240/g).^2)./(2*(Bh^2+(S^2)*(240/g)^2))))./...
(Bh^2+(S^2)*(240/g)^2)^(1/2)...
+(A11/R)*(exp(-((F11+B-
240/g1).^2)./(2*(Bh1^2+(S1^2)*(240/g1)^2))))./...
(Bh1^2+(S1^2)*(240/g1)^2)^(1/2)...
+A12*(exp(-((F12+B-336/g).^2)./(2*(Bh^2+(S^2)*(336/g)^2))))./...
(Bh^2+(S^2)*(336/g)^2)^(1/2)...
+(A12/R)*(exp(-((F12+B-
336/g1).^2)./(2*(Bh1^2+(S1^2)*(336/g1)^2))))./...
(Bh1^2+(S1^2)*(336/g1)^2)^(1/2);
End
```

The function above fits 13 spectra at once using two *g*-factors (g, g1), two hyperfine

field strengths (`Bh, Bh1`), and two spin orbit strengths (`S, S1`) for the entire fit. `R` is the ratio between the two Gaussian areas, and the areas (`A-A12`) are individual fitting parameters. In this way it is possible to fit the widths of 13 spectra (10 derivative and 3 high field absorption) with only 7 variables as opposed to 13 individual fits with the same number of variables.

APPENDIX B

MODELLING THE HALF-FIELD RESONANCE

The half-field resonance line shapes were modelled using the EasySpin MATLAB toolbox [38]. We assume a spin-1 species (triplet) with an isotropic g-factor near the free electron g-factor and an axial zero-field splitting tensor **D**. We also take into account an isotropic Gaussian line broadening. We then calculate the solid-state continuous-wave zero-harmonic EPR line shape with EasySpin (using the 'pepper' function). Strictly speaking, this does not represent the pulse experiment which we performed, but it does result in the same field dependence. Finally, we used the least-squares fitting function of EasySpin ('esfit') in order to obtain values for the g-factor, the line width, and **D** that reproduced to observed line shapes. The standard deviations for all parameters were determined using the bootstrap method as described above.

APPENDIX C

LIST OF ABBREVIATIONS

cw	continuous wave
EDMR	electrically detected magnetic resonance
ITO	indium tin oxide
SOC	Spin-orbit coupling
pEDMR	pulsed electrically detected magnetic resonance
HOMO	highest occupied molecular orbit
LUMO	lowest occupied molecular orbit
PFO	polyfluorene
NMR	nuclear magnetic resonance
ESR/EPR	electron spin/paramagnetic resonance
KSM	Kaplan Solomon and Mott
PP	polaron pair
OMAR	organic magnetoresistance
OLED	organic light emitting diode
SNR	signal to noise ratio
CPWG	coplanar waveguide
Al	aluminum
Ca	calcium
GB	glovebox
ADC	analog digital converter
TWT	traveling wave tube
SNR	signal to noise ratio
IV	current voltage
EL	electroluminescence
SRT	shot repetition time
MW	microwave

REFERENCES

[1]   A. Thiessen, THE INFLUENCE OF MORPHOLOGY ON EXCITONS, University of Utah, 2014.

[2]   J. Hachmann, R. Olivares-Amaya, S. Atahan-Evrenk, C. Amador-Bedolla, R. S. Sánchez-Carrera, A. Gold-Parker, L. Vogt, A. M. Brockway, and A. Aspuru-Guzik, J. Phys. Chem. Lett. **2**, 2241 (2011).

[3]   W. J. Baker, K. Ambal, D. P. Waters, R. Baarda, H. Morishita, K. van Schooten, D. R. McCamey, J. M. Lupton, and C. Boehme, Nat. Commun. **3**, 898 (2012).

[4]   P. Heremans, G. H. Gelinck, R. Müller, K.-J. Baeg, D.-Y. Kim, and Y.-Y. Noh, Chem. Mater. **23**, 341 (2011).

[5]   Z. H. Xiong, D. Wu, Z. V. Vardeny, and J. Shi, Nature **427**, 821 (2004).

[6]   R. Geng, T. T. Daugherty, K. Do, H. M. Luong, and T. D. Nguyen, J. Sci. Adv. Mater. Devices **1**, 128 (2016).

[7]   J. Stephens and C. D. Leonnig, Washington Post 3 (2011).

[8]   P. Cohan, Forbes 2 (2012).

[9]   M. Baibich, J. Broto, A. Fert, Nguyen Van Dau F, F. Petroff, P. Etienne, G. Creuzet, A. Friederich, and J. Chazelas, Phys. Rev. Lett. **61**, 2472 (1988).

[10]   Editorial, Nat. Mater. **8**, 691 (2009).

[11]   V. A. Dediu, L. E. Hueso, I. Bergenti, and C. Taliani, Nat. Mater. **8**, 707 (2009).

[12]   C. Boehme and J. M. Lupton, Nat. Nanotechnol. **8**, 612 (2013).

[13]   F. Klotz, H. Huebl, D. Heiss, K. Klein, J. J. Finley, and M. S. Brandt, Rev. Sci. Instrum. **82**, 074707 (2011).

[14] A. Blank, E. Dikarov, R. Shklyar, and Y. Twig, Phys. Lett. A **377**, 1937 (2013).

[15] E. Gibney, Nature **533**, 448 (2016).

[16] A. M. Tyryshkin, S. Tojo, J. J. L. Morton, H. Riemann, N. V Abrosimov, P. Becker, H.-J. Pohl, T. Schenkel, M. L. W. Thewalt, K. M. Itoh, and S. a Lyon, Nat. Mater. **11**, 143 (2012).

[17] D. Rugar, R. Budakian, H. J. Mamin, and B. W. Chui, Nature **430**, 329 (2004).

[18] M. Widmann, S. Lee, T. Rendler, N. T. Son, H. Fedder, S. Paik, L.-P. Yang, N. Zhao, S. Yang, I. Booker, A. Denisenko, M. Jamali, S. A. Momenzadeh, I. Gerhardt, T. Ohshima, A. Gali, E. Janzén, and J. Wrachtrup, Nat. Mater. **14**, (2014).

[19] R. H. Friend, R. W. Gymer, A. B. Holmes, J. H. Burroughes, R. N. Marks, C. Taliani, D. D. C. Bradley, M. Logdlund, W. R. Salaneck, D. A. Dos Santos, and J. L. Bredas, Nature **397**, 121 (1999).

[20] H. Malissa, M. Kavand, D. P. Waters, K. J. van Schooten, P. L. Burn, Z. V. Vardeny, B. Saam, J. M. Lupton, and C. Boehme, Science (80-.). **345**, 1487 (2014).

[21] W. J. Baker, D. R. McCamey, K. J. van Schooten, J. M. Lupton, and C. Boehme, Phys. Rev. B **84**, 165205 (2011).

[22] J. Behrends, A. Schnegg, K. Lips, E. a Thomsen, a K. Pandey, I. D. W. Samuel, and D. J. Keeble, Phys. Rev. Lett. **105**, 176601 (2010).

[23] P. A Bobbert, T. D. Nguyen, F. W. A van Oost, B. Koopmans, and M. Wohlgenannt, Phys. Rev. Lett. **99**, 216801 (2007).

[24] A. Kitai, *Principles of Solar Cells , LEDs and Diodes*, 1st ed. (Wiley & Sons, West Sussex, 2011), pp. 1–316.

[25] E. Collini and G. D. Scholes, Science **323**, 369 (2009).

[26] B. Shklovskii, H. Fritzsche, and S. Baranovskii, Phys. Rev. Lett. **62**, 2989 (1989).

[27] K. J. van Schooten, D. L. Baird, M. E. Limes, J. M. Lupton, and C. Boehme, Nat. Commun. **6**, 6688 (2015).

[28] G. Jeschke, Chemphyschem **3**, 927 (2002).

[29] T. Herring, S.-Y. Lee, D. McCamey, P. Taylor, K. Lips, J. Hu, F. Zhu, a. Madan, and C. Boehme, Phys. Rev. B **79**, 195205 (2009).

[30] M. Pope and C. E. Swenberg, *Electronic Processes in Organic Crystals and Polymers*, 2nd ed. (Oxford University Press Inc., New York, 1999), pp. 1–1328.

[31] N. S. Sariciftci, L. Smilowitz, A. J. Heeger, and F. Wudl, Science (80-.). **258**, 1474 (1992).

[32] P. F. Weller, J. Chem. Educ. **44**, 391 (1967).

[33] B. Valeur, *Molecular Fluorescence Principles and Applications*, 1st ed. (Wiley-VCH, Weinheim, 2002), pp. 1–381.

[34] J. Lakowicz, *Topics in Fluorescence Spectroscopy*, 3rd ed. (Kluwer Academic Publishers, New York, 2002), p. 390.

[35] F. A. Sperlich, Electron Paramagnetic Resonance Spectroscopy of Conjugated Polymers and Fullerenes for Organic Photovoltaics, Würzburg, 2013.

[36] D. P. Waters, MAGNETORESISTANCE OF POLYMER DIODES, University of Utah, 2014.

[37] T. L. Keevers, W. J. Baker, and D. R. McCamey, Phys. Rev. B **91**, 205206 (2015).

[38] D. R. McCamey, K. J. van Schooten, W. J. Baker, S.-Y. Lee, S.-Y. Paik, J. M. Lupton, and C. Boehme, Phys. Rev. Lett. **104**, 017601 (2010).

[39] C. Boehme, D. R. McCamey, K. J. van Schooten, W. J. Baker, S.-Y. Lee, S.-Y. Paik, and J. M. Lupton, Phys. Status Solidi **246**, 2750 (2009).

[40] M. Kavand, D. Baird, K. van Schooten, H. Malissa, J. M. Lupton, and C. Boehme, Phys. Rev. B **94**, 075209 (2016).

[41] F. Bloch, Phys. Rev. **70**, 460 (1946).

[42] E. Purcell, H. Torrey, and R. Pound, Phys. Rev. **69**, 37 (1946).

[43] I. I. Rabi, J. R. Zacharias, S. Millman, and P. Kusch, Phys. Rev. **53**, 318 (1938).

[44] I. I. Rabi, Phys. Rev. **51**, 652 (1937).

[45] B. I. Kochelaev and Y. V. Yablokov, *The Beginning of Paramagnetic Resonance*, 1st ed. (World Scientific, Singapore, 1995), p. 184.

[46] P. Charles P., *Electron Spin Resonance : A Comprehensive Treatise on Experimental Techniques*, 2nd ed. (Mineola, 1997), p. 810.

[47] C. Boehme and K. Lips, Phys. Rev. B **68**, 245105 (2003).

[48]   J. C. Cook, J. Res. Natl. Inst. Stand. Technol. **119**, 55 (2014).

[49]   I. I. Rabi, N. F. Ramsey, and J. Schwinger, Rev. Mod. Phys. **26**, 167 (1954).

[50]   A. Schweiger and G. Jeschke, *Principles of Pulse Electron Paramagnetic Resonance*, 1st ed. (Oxford University Press Inc., New York, 2001), pp. 1–578.

[51]   J. J. Sakurai, *Modern Quantum Mechanics (Revised Edition)* (Addison-Wesley, Reading, 1994), p. 500.

[52]   P. ZEEMAN, Nature **55**, 347 (1897).

[53]   G. Joshi, R. Miller, L. Ogden, M. Kavand, S. Jamali, K. Ambal, S. Venkatesh, D. Schurig, H. Malissa, J. M. Lupton, and C. Boehme, Appl. Phys. Lett. **109**, 103303 (2016).

[54]   N. M. Atherton, *Electron Spin Resonance : Theory and Applications* (Ellis Horwood Ltd., New York, 1973), p. 438.

[55]   K. J. Van Schooten, OPTICALLY ACTIVE CHARGE TRAPS AND CHEMICAL DEFECTS IN SEMICONDUCTING NANOCRYSTALS PROBED BY PULSED OPTICALLY DETECTED MAGNETIC RESONANCE, University of Utah, 2013.

[56]   S. Günes, H. Neugebauer, and N. S. Sariciftci, Chem. Rev. **107**, 1324 (2007).

[57]   K. Murata, Y. Shimoi, S. Abe, S. Kuroda, T. Noguchi, and T. Ohnishi, Chem. Phys. **227**, 191 (1998).

[58]   G. B. Silva, L. F. Santos, R. M. Faria, and C. F. O. Graeff, Phys. B Condens. Matter **308-310**, 1078 (2001).

[59]   A. R. Stegner, C. Boehme, H. Huebl, M. Stutzmann, K. Lips, and M. S. Brandt, Nat. Phys. **2**, 835 (2006).

[60]   M. Xiao, I. Martin, E. Yablonovitch, and H. W. Jiang, Nature **430**, 435 (2004).

[61]   A. Morello, J. J. Pla, F. a Zwanenburg, K. W. Chan, K. Y. Tan, H. Huebl, M. Möttönen, C. D. Nugroho, C. Yang, J. a van Donkelaar, A. D. C. Alves, D. N. Jamieson, C. C. Escott, L. C. L. Hollenberg, R. G. Clark, and A. S. Dzurak, Nature **467**, 687 (2010).

[62]   R. Vincent, S. Klyatskaya, M. Ruben, W. Wernsdorfer, and F. Balestro, Nature **488**, 357 (2012).

[63]   D. R. McCamey, S.-Y. Lee, S.-Y. Paik, J. M. Lupton, and C. Boehme, Phys. Rev. B **82**, 125206 (2010).

[64] R. Maxwell and A. Honig, Phys. Rev. Lett. **17**, 188 (1966).

[65] R. Glenn, W. Baker, C. Boehme, and M. Raikh, Phys. Rev. B **87**, 155208 (2013).

[66] F. Hoehne, L. Dreher, M. Suckert, D. P. Franke, M. Stutzmann, and M. S. Brandt, Phys. Rev. B **88**, 155301 (2013).

[67] G. Li, C. H. Kim, P. a. Lane, and J. Shinar, Phys. Rev. B **69**, 165311 (2004).

[68] S.-Y. Paik, S.-Y. Lee, W. J. Baker, D. R. McCamey, and C. Boehme, Phys. Rev. B **81**, 075214 (2010).

[69] M. Fehr, J. Behrends, S. Haas, B. Rech, K. Lips, and a. Schnegg, Phys. Rev. B **84**, 193202 (2011).

[70] A. Schnegg, J. Behrends, M. Fehr, and K. Lips, Phys. Chem. Chem. Phys. **14**, 14418 (2012).

[71] E. L. Hahn, Phys. Rev. **80**, 580 (1950).

[72] C. Boehme, P. Kanschat, and K. Lips, J. Non. Cryst. Solids **299-302**, 566 (2002).

[73] a. Gliesche, C. Michel, V. Rajevac, K. Lips, S. D. Baranovskii, F. Gebhard, and C. Boehme, Phys. Rev. B **77**, 245206 (2008).

[74] D. R. Mccamey, H. A. Seipel, S. Y. Paik, M. J. Walter, N. J. Borys, J. M. Lupton, and C. Boehme, Nat. Mater. 1 (2008).

[75] D. J. Lepine, Phys. Rev. B **6**, 436 (1972).

[76] R. M. White and J. F. Gouyet, Phys. Rev. B **16**, 3596 (1977).

[77] D. Kaplan, I. Solomon, and N. F. Mott, J. Phys. Lettres **39**, 51 (1978).

[78] E. L. Frankevich, A. A. Lymarev, I. Sokolik, F. E. Karasz, S. Blumstengel, R. H. Baughman, and H. H. Hörhold, Phys. Rev. B **46**, 9320 (1992).

[79] W. Wagemans, F. L. Bloom, P. a. Bobbert, M. Wohlgenannt, and B. Koopmans, J. Appl. Phys. **103**, 07F303 (2008).

[80] M. A. Lampert, Phys. Rev. Lett. **1**, 450 (1958).

[81] F. Jakubka, S. B. Grimm, Y. Zakharko, F. Gannott, and J. Zaumseil, ACS Nano **8**, 8477 (2014).

[82] G. Finkelstein, H. Shtrikman, and I. Bar-Joseph, Phys. Rev. B **53**, R1709 (1996).

[83] V. Ern and R. E. Merrifield, Phys. Rev. Lett. **21**, 609 (1968).

[84] M. A. Baldo, C. Adachi, and S. R. Forrest, Phys. Rev. B **62**, 10967 (2000).

[85] M. H. Levitt, *Sin Dynamics: Basics of Nuclear Magnetic Resonance*, 2nd ed. (John Wiley & Sons, Inc., West Sussex, 2008).

[86] C. Boehme, Dynamics of Spin – Dependent Charge Carrier Recombination, Philipps–Universitat Marburg, 2002.

[87] T. Adachi, J. Vogelsang, and J. M. Lupton, J. Phys. Chem. Lett. **5**, (2014).

[88] T. Adachi, J. Vogelsang, and J. M. Lupton, J. Phys. Chem. Lett. **5**, 2165 (2014).

[89] M. Ariu, D. G. Lidzey, M. Sims, A. J. Cadby, P. A. Lane, and D. D. C. Bradley, J. Phys. Condens. Matter **14**, 9975 (2002).

[90] B. Arredondo, B. Romero, a. Gutiérrez-Llorente, a. I. Martínez, a. L. Álvarez, X. Quintana, and J. M. Otón, Solid. State. Electron. **61**, 46 (2011).

[91] K. Asada, T. Kobayashi, and H. Naito, Jpn. J. Appl. Phys. **45**, L247 (2006).

[92] D. D. C. Bradley, M. Grell, X. Long, H. Mellor, A. Grice, H. Road, M. Inbasekaran, and E. P. Woo, in (1997), pp. 254–259.

[93] A. J. Cadby, P. A. Lane, H. Mellor, S. J. Martin, M. Grell, C. Giebeler, D. D. C. Bradley, M. Wohlgenannt, C. An, and Z. V. Vardeny, Phys. Rev. B **62**, 15604 (2000).

[94] R. Palacios, P. Formentin, E. Martinez-Ferrero, J. Pallarès, and L. F. Marsal, Nanoscale Res. Lett. **6**, 35 (2010).

[95] C. Rothe and A. P. Monkman, Phys. Rev. B **68**, 075208 (2003).

[96] T. Jen, K. Wang, and S. Chen, Polymer (Guildf). **53**, 5850 (2012).

[97] A. Monkman, R. Simon, and K. Fernando, *Polyfluorene Photophysics* (Springer, Berlin, 2008), pp. 187–225.

[98] M. Wohlgenannt, K. Tandon, S. Mazumdar, S. Ramasesha, and Z. V Vardeny, Nature **409**, 494 (2001).

[99] S. H. Chen, A. C. Su, and S. A. Chen, J. Phys. Chem. B **109**, 10067 (2005).

[100] M. Grell, D. D. C. Bradley, G. Ungar, J. Hill, and K. S. Whitehead, Macromolecules **32**, 5810 (1999).

[101] B. Arredondo, B. Romero, A. I. Martínez, A. L. Álvarez, X. Quintana, and J. M. Otón, Solid State Electron. **61**, 46 (2011).

[102] P. Atkins and J. De Paula, *Physical Chemistry*, 8th ed. (Oxford University Press Inc., New York, 2006).

[103] J. R. Lakowicz, *Principles of Fluorescence Spectroscopy*, 3rd ed. (Springer, New York, 2006), p. 954.

[104] M. de Jong, L. Seijo, A. Meijerink, and F. T. Rabouw, Phys. Chem. Chem. Phys. **17**, 16959 (2015).

[105] H. T. Nicolai, G. a. H. Wetzelaer, M. Kuik, a. J. Kronemeijer, B. de Boer, and P. W. M. Blom, Appl. Phys. Lett. **96**, 172107 (2010).

[106] P. Prins, F. C. Grozema, B. S. Nehls, T. Farrell, U. Scherf, and L. D. a. Siebbeles, Phys. Rev. B **74**, 113203 (2006).

[107] M. Jaiswal and R. Menon, **1384**, 1371 (2006).

[108] P. W. M. Blom and M. C. J. M. Vissenberg, Mater. Sci. Eng. R Reports **27**, 53 (2000).

[109] T.-H. Jen, K.-K. Wang, and S.-A. Chen, Polymer (Guildf). **53**, 5850 (2012).

[110] E. J. W. List, R. Guentner, P. Scanducci de Freitas, and U. Scherf, Adv. Mater. **14**, 374 (2002).

[111] J. Lee, G. Klaerner, and R. D. Miller, Chem. Mater. **11**, 1083 (1999).

[112] E. Zojer, A. Pogantsch, E. Hennebicq, D. Beljonne, J.-L. Brédas, P. Scandiucci de Freitas, U. Scherf, and E. J. W. List, J. Chem. Phys. **117**, 6794 (2002).

[113] J. D. Jackson, *Classical Electrodynamics*, 3rd ed. (John Wiley, New York, 1999), p. 832.

[114] W. J. Baker, COHERENTLY CONTROLLED SPIN-DEPENDENT CHARGE CARRIER TRANSITIONS IN ORGANIC SEMICONDUCTORS : PROPERTIES AND APPLICATIONS, University of Utah, 2012.

[115] E. J. . List, M. Gaal, R. Guentner, P. S. de Freitas, and U. Scherf, Synth. Met. **139**, 759 (2003).

[116] N. Stemeroff and R. de Sousa, Phys. Rev. Lett. **107**, 197602 (2011).

[117] R. Landauer, Phys. D Nonlinear Phenom. **38**, 226 (1989).

[118] M. Turlakov, Phys. Rev. B **62**, 4656 (2000).

[119] H. Nyquist, Phys. Rev. **32**, 110 (1928).

[120] J. B. Johnson, Phys. Rev. **32**, 97 (1928).

[121] B. Efron and T. Robert J, *An Introduction to the Bootstrap*, 1st ed. (Chapman & Hall, New York, 1993).

[122] V. Dyakonov, G. Rösler, M. Schwoerer, and E. L. Frankevich, Phys. Rev. B **56**, 3852 (1997).

[123] S. Schaefer, S. Saremi, K. Fostiropoulos, J. Behrends, K. Lips, and W. Harneit, Phys. Status Solidi **245**, 2120 (2008).

[124] W. J. Baker, T. Keevers, J. Lupton, D. McCamey, and C. Boehme, Phys. Rev. Lett. **108**, 267601 (2012).

[125] H. Huebl, F. Hoehne, B. Grolik, A. R. Stegner, M. Stutzmann, and M. S. Brandt, Phys. Rev. Lett. **100**, 177602 (2008).

[126] S.-Y. Lee, S. Paik, D. R. McCamey, and C. Boehme, Phys. Rev. B **86**, 115204 (2012).

[127] C. G. Yang, E. Ehrenfreund, F. Wang, T. Drori, and Z. V. Vardeny, Phys. Rev. B **78**, 205312 (2008).

[128] D. R. McCamey, H. a Seipel, S.-Y. Paik, M. J. Walter, N. J. Borys, J. M. Lupton, and C. Boehme, Nat. Mater. **7**, 723 (2008).

[129] L. S. Swanson, J. Shinar, A. R. Brown, D. D. C. Bradley, R. H. Friend, P. L. Burn, A. Kraft, and A. B. Holmes, Phys. Rev. B **46**, 15072 (1992).

[130] W. J. Baker, T. L. Keevers, C. Boehme, and D. R. McCamey, Phys. Rev. B **92**, 041201 (2015).

[131] C. Rothe, S. King, F. Dias, and a. Monkman, Phys. Rev. B **70**, 195213 (2004).

[132] S. Stoll, Spectral Simulations in Solid-State Electron Paramagnetic Resonance, Eidgenössische Technische Hochschule Zürich, 2003.

[133] S. Stoll and A. Schweiger, J. Magn. Reson. **178**, 42 (2006).

[134] B. Z. Tedlla, F. Zhu, M. Cox, J. Drijkoningen, J. Manca, B. Koopmans, and E. Goovaerts, Adv. Energy Mater. **5**, 1401109 (2015).

[135] J. Niklas, K. L. Mardis, B. P. Banks, G. M. Grooms, A. Sperlich, V. Dyakonov, S. Beaupré, M. Leclerc, T. Xu, L. Yu, and O. G. Poluektov, **15**, 9562 (2013).

[136] K. Kanemoto, H. Matsuoka, Y. Ueda, K. Takemoto, K. Kimura, and H. Hashimoto, Phys. Rev. B **86**, 125201 (2012).

[137] M. Stutzmann and R. Street, Phys. Rev. Lett. **54**, 1836 (1985).

[138] H. Malissa, M. Kavand, D. P. Waters, K. J. van Schooten, P. L. Burn, Z. V. Vardeny, B. Saam, J. M. Lupton, and C. Boehme, Science (80-.). **345**, 1487 (2014).

[139] W. J. Baker, T. L. Keevers, J. M. Lupton, D. R. McCamey, and C. Boehme, Phys. Rev. Lett. **108**, 267601 (2012).

[140] F. Hoehne, L. Dreher, H. Huebl, M. Stutzmann, and M. S. Brandt, Phys. Rev. Lett. **106**, 187601 (2011).